Vesicles in Flow: Role of Thermal Fluctuations

Von der Fakultät Mathematik und Physik der Universität Stuttgart
zur Erlangung der Würde eines Doktors der Naturwissenschaften (Dr. rer. nat.)
genehmigte Abhandlung

vorgelegt von

David Abreu

aus Saint-Etienne (Frankreich)

Hauptberichter: Prof. Dr. Udo Seifert
Mitberichter: Prof. Dr. Christian Holm

Tag der Einreichung: 10. April 2014
Tag der mündlichen Prüfung: 27. Mai 2014

II. Institut für Theoretische Physik der Universität Stuttgart

2014

Contents

List of figures

Abbreviations and symbols

Abbreviations

ATP	adenosine triphosphate
GUV	giant unilamellar vesicle
INT	intermittent
KS	Keller-Skalak
NESS	non-equilibrium steady-state
RBC	red blood cell
SS	Skotheim-Secomb
SW	swinging
TB	tumbling
TR	trembling
TT	tank-treading
VB	vacillating-breathing
WBC	white blood cell

Mathematical notations

$\bar{\mathbf{X}}$, $\mathbf{X}$, X	tensor, vector, scalar quantity
$\cdot$, $\times$, $\otimes$	scalar, vector, tensor product
$\langle\rangle$	ensemble average
(x, y, z)	cartesian coordinates
(r, θ, ϕ)	spherical coordinates
δ_{ij}, $\delta(t)$	Kronecker symbol, Dirac distribution
∂_i, $\dot{x}$	derivative with respect to variable i, time-derivative of x
$\mathbf{e_i}$	unit vector of coordinate i
$\int \mathrm{d}A$, $\int \mathrm{d}V$	integral over the surface, the volume of a body
$\mathbf{n}$	normal vector
∇, ∇_s	gradient operator, gradient on the surface
Δ_s	Laplace-Beltrami operator on the surface

Symbols

α_1, α_2, α_3	geometrical quantities of the KS model, page 51
γ	friction coefficient
$\dot{\gamma}$	shear rate, page 37
Δ	vesicle excess area, page 30
ε_{lm}	only non-zero for $(l, m) = (2, \pm 2)$, page 68
$\zeta(t), \xi(t), \chi(t)$	Gaussian white noise
η, η_i, η_o	viscosity, inner viscosity, outer viscosity
Θ	vesicle orientation angle, page 38
Θ_{TT}	TT inclination angle of the KS model, page 55
κ	vesicle bending rigidity
λ	viscosity contrast, page 30
λ'	reduced viscosity contrast, page 52
λ_c	critical viscosity contrast of the KS model, page 55
Λ	dimensionless rotation-to-elongation ratio, page 40
μ	mobility
μ_l	mobility of the l modes,, page 68
ν_l	dimensionless mobility of the l modes, page 79
$\bar{\mathbf{\Pi}}$	hydrodynamic stress tensor
ρ	density
σ, σ_{lm}	surface tension, quasi-spherical expansion coefficients, page 67
τ	characteristic bending timescale , page 79
ϕ_{lm}	orientation angle of the (l, m) mode, page 84
$\tilde{\Phi}$	displacement angle of a membrane element, page 38
Φ	parametric angle of the vesicle cross-section, page 50
ω	strength of rotational flow, page 37
ω_{TB}	tumbling ratio, page 52
a_k	Fourier coefficients of the vesicle cross-section, page 80
A	vesicle area
B	geometrical quantity of the KS model, page 52
c	constant, page 68
C	geometrical quantity of the KS model, page 51
C_{123}^{lm}	integral over three spherical harmonics, page 90
C_a	capillary number, page 37
d	energy dissipated in a volume of fluid, page 26
D	diffusion coefficient
D_{eff}	effective diffusion constant, page 54
D_Φ	TT diffusion constant, page 53

D_Θ	TB diffusion constant, page 53
E_0	shape-memory energy, page 52
$\mathbf{f}$, f, $\mathbf{F}$, F	force
g	determinant of the metric tensor, page 31
g_1, g_2, g_3'	geometrical quantities of the KS model, page 51
h	distance between wall and vesicle, page 43
H	mean curvature, page 31
$\mathcal{H}$, $\mathcal{H}_\kappa$	Helfrich bending energy, page 32
K	Gaussian curvature, page 31
k^*, k^*_{even}, k^*_{odd}	mean wave number, even part, odd part, page 80
k_B	Boltzmann constant
l_1, l_2, l_3	main axes of an ellipsoidal vesicle, page 50
$\mathbf{M}$, M	moment
$\hat{p}$	pressure
$p(x,t)$, $p^{\text{eq}}(x)$, $p^s(x)$	probability distribution function, equilibrium, stationary
$\mathbf{r}$	position vector
$\mathbf{R}$,R	vesicle radius
R_0	effective vesicle radius, page 30
Re	Reynolds number, page 26
s	strength of elongational flow, page 37
S	dimensionless elongational rate, page 40
T	temperature (293 K in the numerical results)
u, u_{lm}	quasi-spherical expansion function, coefficients, page 65
U_e	dimensionless shape-memory energy, page 59
$\mathbf{v}$	velocity
$\mathbf{v}^\infty$	external flow, page 37
$\mathbf{V}$	velocity field on the sphere , page 27
V	vesicle volume
$\dot{W}$	rate of work applied by a fluid on a body, page 26
X, Y, Z	components of $\mathbf{V}$, page 27
$\mathcal{Y}_{lm}$	spherical harmonic, page 90
z_0, z_1, z_2	geometrical quantities of the KS model, page 51

Kurzfassung

Die vorliegende Dissertation befasst sich mit der Dynamik fluider Vesikel im hydrodynamischen Fluss mit einem besonderen Fokus auf den Einfluss thermischer Fluktuationen auf diese Dynamik. Vesikel sind geschlossene Membranen, die aus einer sehr dünnen Lipiddoppelschicht bestehen. Sei schließen eine Flüssigkeit ein und schweben in einer anderen Flüssigkeit. In biologischen Systemen dienen sie dem intra- und interzellulären Informationsaustausch. Sie werden auch als pharmazeutische Stoffträger eingesetzt. Zudem stellen Vesikel das einfachste Modellsystem für komplexere Zellen dar, die eine Lipidmembran besitzen, wie beispielsweise rote Blutkörperchen. Die Untersuchung der Dynamik von Vesikeln im Fluss ist deshalb sowohl aus biologischer als auch technologischer Perspektive von großer Bedeutung.

Insbesondere betrachten wir riesige, unilamellare Vesikel (GUVs, aus dem Englischen *giant unilamellar vesicles*), die mit einem Radius von circa 10 µm sehr viel größer als ihre 5 nm-dicke Membran sind. Ein GUV kann daher als eine geschlossene zweidimensionale Fläche betrachtet werden. Die Membran befindet sich bei Raumtemperatur in einer flüssigen Phase, und ist in guter Näherung inkompressibel und für viele Ionen undurchlässig, sodass das Volumen und die Fläche des Vesikels konstant bleiben. Da Krümmungsdeformationen der Membran energetisch viel günstiger sind als Scherung- oder Streckungsdeformationen, reichen sie aus, um die Gleichgewichtskonfigurationen von Vesikeln unter den zwei vorher erwähnten Zwangsbedingungen vorherzusagen. Außerdem liegt die Krümmungsenergie der Membran bei $10 - 50\ k_{\mathrm{B}}T$, wobei $k_{\mathrm{B}}T$ die typische thermische Energie ist. Damit spielen thermische Fluktuationen eine große Rolle in den Formänderungen von GUVs.

In dieser Arbeit untersuchen wir theoretisch die Dynamik von GUVs in ebenen, linearen Flüssen, die aus einem Rotation- und einem Elongationsanteil bestehen. Unser Hauptziel ist es, den Einfluss thermischer Fluktuationen auf die verschiedenen Bewegungsarten eines Vesikels im Fluss zu beschreiben. Um analytische Bewegungsgleichungen herleiten zu können, betrachten wir entweder ellipsoidale Vesikel mit fester Form oder quasisphärische Vesikel. Wir lösen diese Gleichungen entweder analytisch oder numerisch und vergleichen die daraus resultierenden Ergebnisse mit zahlreichen experimentellen Beobachtungen, um diese theoretisch zu erläutern.

Kapitel 2: Grundlagen. In diesem Kapitel stellen wie die Grundgleichungen vor, die für die Beschreibung von Vesikeln in externen Flüssen notwendig sind. Erstens können wegen der mikroskopischen Größe von GUVs die Trägheitsterme der Navier-Stokes-Gleichungen vernachlässigt werden, weswegen hydrodynamische Flüsse durch die Stokes-Gleichungen beschrieben werden. Diese Gleichungen setzen voraus, dass alle Kräfte und Momente zu jeder Zeit ausgeglichen sind, oder anders gesagt, dass es keine Bewegung ohne Kraft gibt. Außerdem führen wir die sogenannte Lamb'sche Lösung der Stokes-Gleichungen ein, die für Probleme von sphärischer Geometrie besonders geeignet ist. Zweitens unterliegen Vesikel zufälligen Stößen, die aus der thermischen Bewegung der umgebenden, kleineren Flüssigkeitsmoleküle kommen. Der Einfluss dieser thermischen Fluktuationen wird durch die Langevin- beziehungsweise Fokker-Planck-Gleichung beschrieben. Drittens verursachen sowohl hydrodynamische als auch thermische Kräfte Krümmungsdeformationen der Membran, die durch die Helfrich'sche Krümmungsenergie beschrieben werden.

Kapitel 3: Fluide Vesikel im Fluss. In diesem Kapitel geben wir einen Überblick über die Flussdynamik von Vesikeln, die in den letzten Jahren intensiv untersucht wurde. In ebenen, linearen Flüssen weisen Vesikel drei Hauptbewegungsarten auf. In der Panzerkettenbewegung (TT, *tank-treading*) bleibt der Anstellwinkel des Vesikels bezüglich der Flussrichtung konstant, während die Membran sich um den inneren Fluss dreht wie eine Panzerkette. Die Taumelbewegung (TB, *tumbling*) besteht aus einer Drehbewegung, die der Rotation eines starren Körpers ähnlich ist. Dabei bleibt die Vesikelform einigermaßen ellipsoidal. Am Übergang zwischen TT und TB findet man eine zitternde Bewegung (TR, *trembling*), die sich durch eine Schwingung des Anstellwinkels und starke, asymmetrische Deformationen auszeichnet. Der Übergang zwischen diesen drei Bewegungsarten ist durch mehrere Parameter bestimmt, nämlich die Stärke der Rotation- und Elongationsanteile des Flusses, das Viskositätsverhältnis zwischen innerer und äußerer Flüssigkeit, und die Exzessfläche, die das Vesikel im Vergleich zu einer Kugel mit gleichem Volumen besitzt. Für ausreichend starke Flüsse werden faltenähnliche Deformationen von kleiner Wellenlänge beobachtet, wie man sie auch in schlagartig umgedrehte Elongationsflüsse beobachten kann. Die hier beschriebenen Phänomene untersuchen wir in Kapiteln 4, 5,und 6.

Kapitel 4: Unverformbare Vesikel. Der für sehr kleine Scherraten beobachtete TT-TB-Übergang wird sehr gut vom Keller-Skalak-Modell (KS) für formbeständige ellipsoidale Vesikel vorhergesagt, wobei die Dynamik nur von zwei Variablen beschrieben wird, nämlich dem Anstellwinkel der langen Achse des Vesikels bezüglich der Flussrichtung und einem Phasenwinkel, der die Auslenkung eines Membranpunktes

bezüglich seiner Gleichgewichtsposition misst. Das Skotheim-Secomb-Modell (SS) verallgemeinert das KS-Modell, indem eine vom Phasenwinkel periodisch abhängende elastische Energie berücksichtigt wird, die das Formgedächtnis roter Blutkörperchen modelliert. In diesem Kapitel fügen wir thermische Fluktuationen zu diesen zwei Modellen hinzu und leiten die resultierende stochastische Bewegungsgleichungen her. Durch die Lösung der entsprechenden Fokker-Planck Gleichungen erhalten wir die stationären Wahrscheinlichkeitsverteilungen, womit wir dynamische Phasendiagramme erstellen, die für Vesikel mit experimentell zugänglichen Abmessungen gelten.

Für fluide Vesikel sagt das KS-Modell einen Übergang zwischen TT und TB voraus, der nur vom Viskositätsverhältnis und nicht von der Scherrate abhängt. Mit thermischen Fluktuationen hängt dieser Übergang auch von der Scherrate ab, was besonders bei kleinen Scherraten ausgeprägt ist, weil thermische Fluktuationen maßgeblich werden. Infolgedessen wird eine TB-Bewegung für beliebige Viskositätsverhältnisse beobachtet, da Vesikel dann einen gerichteten Zufallspfad vollführen. Sporadische TB-Rotationen finden nah am Übergang auch für TT-Vesikel statt. Für elastische Vesikel oszilliert des Anstellwinkel während der TT-Bewegung, weshalb man von Schwingen (SW, *swinging*) dann redet. Zudem wird eine intermittierende (INT) Bewegung vorhergesagt, die aus abwechselnden SW- und TB-Perioden besteht. Der Übergang zwischen diesen drei Bewegungsarten hängt dann nicht nur vom Viskositätsverhältnis sondern auch von der Scherrate und der elastischen Energie ab. Mit thermischen Fluktuationen wird der INT-Bereich im Phasendiagramm viel breiter. Insbesondere kommt die INT-Bewegung auch in Bereichen vor, in denen das deterministische Modell einen direkten SW-TB-Übergang vorhersagt, da SW und TB dann ähnliche Energien besitzen und daher durch thermisches Rauschen gemischt werden.

Kapitel 5: Zitternde Bewegung. Deformationen werden in Modellen für quasisphärische Vesikel, d.h. Vesikel mit kleiner Exzessfläche, berücksichtigt. Diese Modelle beruhen auf einer Entwicklung des Vesikelradius in Kugelflächenfunktionen. Die Bewegungsgleichungen für die Entwicklungskoeffizienten ergeben sich aus der Lösung der Stokes-Gleichungen für den inneren und den äußeren Fluss. Diese zwei Lösungen werden dann an der virtuellen Kugel, die das gleiche Volumen wie das Vesikel hat, stetig zusammengefügt. Ohne thermisches Rauschen werden drei Bewegungsarten vorhergesagt, nämlich TT, TB, und an deren Übergang eine atmende Bewegung (VB, *vacillating-breathing*), die aus einer periodischen Schwankung des Anstellwinkels besteht, wobei das Vesikel symmetrischen Deformationen unterliegt. Diese VB-Bewegung ist im starken Widerspruch mit der experimentellen TR-Bewegung, die sich durch starke asymmetrische Deformationen während der fluktuierenden Schwankung des Anstellwinkels auszeichnet. Eine

detaillierte Untersuchung der experimentellen Daten zeigt, dass diese langjährige Unstimmigkeit wahrscheinlich an der Vernachlässigung thermischer Fluktuationen in den früheren Modellen liegt.

Hier stellen wir ein Modell für quasisphärische Vesikel im linearen Fluss vor, das thermische Fluktuationen konsistent enthält. Korrekturterme, die aus der Entwicklung der Krümmungsenergie in dritter Ordnung kommen, werden auch berücksichtigt. Dieses Modell liefert Ergebnisse, die quantitativ mit der experimentellen TR-Bewegung übereinstimmen. Grund dafür ist eine Verstärkung des thermischen Rauschens bei negativen Anstellwinkeln, die dazu führt, dass asymmetrische Deformationen stärker werden können als die für die VB-Bewegung maßgebenden ellipsoidalen Deformationen. Die in Simulationen beobachteten Vesikelformen sind in sehr guter Übereinstimmung mit den Experimenten. Außerdem weisen die numerischen und experimentellen Deformationsleistungsspektren die selben Merkmale auf. Das theoretisch vorhergesagte Phasendiagramm entspricht auch den Experimenten, was die Wichtigkeit des thermischen Rauschens in der Flussdynamik von Vesikeln nochmals betont.

Kapitel 6: Falteninstabilität. Ein Vesikel, das einem reinen Elongationsfluss ausgesetzt ist, nimmt eine stationäre ellipsoidale Form an, deren Hauptachse in Flussrichtung ausgerichtet ist. Wenn die Flussrichtung plötzlich um 90° gedreht wird, werden zunächst die Vesikelspitzen zusammengedrückt und Deformationen von kleiner Wellenlänge werden erzeugt. Diese Falten sind nur kurzlebig, weil das Vesikel dann in eine neue Gleichgewichtsform relaxiert, deren Hauptachse senkrecht auf die ursprüngliche Hauptachse liegt. Im konstanten linearen Fluss sind Vesikel bei positiven Anstellwinkeln ellipsoidal, aber sie werden auch vom Fluss zusammengedrückt, wenn der Anstellwinkel in TB- und TR-Bewegungen negative Werte annimmt. Es ist dann zu erwarten, dass für große Flussstärken Falten auftauchen.

In diesem Kapitel zeigen wir experimentelle Beobachtungen einer solchen Falteninstabilität während der TR-Bewegung auf, die anhand analytische und numerische Ergebnisse erläutert werden. Dazu verallgemeinern wir das im Kapitel 5 eingeführte Modell um Korrekturterme, die den Fluss nicht an der virtuellen Kugel sondern an der tatsächlichen Membranposition beschreiben. Diese Falteninstabilität hängt hauptsächlich von der Stärke des Elongationsanteils des Flusses ab, auch wenn die Vortizität und das Viskositätsverhältnis eine Rolle spielen. Wie für die TR-Bewegung sind thermische Fluktuationen von sehr großer Bedeutung. Falten treten in deterministischen Simulationen nicht auf. Simulationen mit thermischem Rauschen zeigen hingegen Deformationen, die mit den Experimenten vergleichbar sind. Diese Deformationen können in einem symmetrischen und einem asymmetrischen Anteil zerlegt werden. In Experimenten und stochastischen Sim-

ulationen entwickeln sich die symmetrischen Deformationen periodisch, und zwar mit der Hälfte der Oszillationsperiode des Anstellwinkels. Hingegen ist die Dynamik der asymmetrischen Deformationen, die nur vom thermischen Rauschen herrühren, nur leicht mit der Anstellwinkeloszillation korreliert. Allerdings werden die experimentellen Messungen von den numerischen Simulationen etwas unterschätzt, was möglicherweise an der quasisphärischen Näherung liegt. Nichtsdestoweniger ist die Übereinstimmung zwischen Theorie und Experiment sehr befriedigend, was darauf hinweist, dass thermische Fluktuationen auch bei stärkeren Flüssen nicht vernachlässigt werden dürfen.

Abstract

The present thesis deals with the dynamics of fluid vesicles in flow, with a particular focus on the role of thermal fluctuations. Vesicles are microscopic "bags" of liquid whose membrane consists of a very thin lipid bilayer. They are used in biological systems for intra- and inter-cellular communication. They also serve as pharmaceutical carriers. Moreover, they represent the simplest model system for more complex cells possessing a lipid membrane such as red blood cells. Therefore, studying the dynamics of vesicles in flow has a great biological and technological relevance.

We are interested in so-called giant unilamellar vesicles (GUVs). Their size is of the order of 10 µm which is much larger than the thickness of their bilayer membrane ($\sim$5 nm). A GUV can thus be modeled as a two-dimensional membrane enclosing a fluid and suspended in another fluid. The membrane is in a liquid phase at room temperature and is to very good approximation incompressible and impermeable to many ions, such that the volume and the surface area of a vesicle remain constant. The bending deformations of the membrane involve much lower energies than the stretching and shearing ones. They are therefore sufficient to predict the equilibrium shapes of vesicles under the two constraints mentioned above. Moreover, the membrane bending energy is around $10-50\ k_{\mathrm{B}}T$, where $k_{\mathrm{B}}T$ is the typical thermal energy. Therefore, thermal fluctuations play an important role in the shape transitions of GUVs.

In this work, we provide a theoretical analysis of the dynamics of GUVs in planar linear flows consisting of a rotational and an elongational component. Our main goal is to investigate the impact of thermal fluctuations on the different dynamical regimes. In order to derive analytical equations of motion, we consider either undeformable vesicles of ellipsoidal shape, or quasi-spherical vesicles corresponding to slightly deflated spheres. We solve these equations either analytically or numerically. We then compare our theoretical predictions to experiments to elucidate the various phenomena observed therein.

Chapter 2: Basics. In this chapter, we present the basic equations necessary to describe vesicles in external flow. First, at the microscopic scale of GUVs the inertial terms in the Navier-Stokes equations can be neglected. Hydrodynamic flows are then described by the Stokes equations which imply that forces and torques

are balanced at every time, i.e. that there is no motion without force. We also introduce a solution of the Stokes equations in spherical geometry known as Lamb's solution. Second, vesicles are strongly affected by the random kicks coming from the thermal agitation of the surrounding smaller fluid molecules. The influence of these thermal fluctuations is described by the Langevin equation or equivalently by the Fokker-Planck equation. Third, both thermal and hydrodynamic forces induce bending deformations of the membrane, which are described by the Helfrich curvature energy.

Chapter 3: Fluid vesicles in flow. The dynamics of vesicles in flow has been intensively investigated in the past years, as reviewed in this chapter. In planar linear flows, vesicles exhibit three main motions. In the tank-treading (TT) regime, the vesicle has a constant orientation relative to the flow direction while its membrane rotates around the interior fluid. In the tumbling (TB) regime, the vesicle undergoes a rigid-body-like rotation while roughly keeping an ellipsoidal form. At the transition between TT and TB, the trembling (TR) regime is observed, in which the orientation angle oscillates while the membrane shows strong asymmetric deformations. The transition between these three dynamical regimes is determined by the magnitude of the elongational and rotational parts of the flow, by the viscosity contrast between inner and outer fluid, and by the excess area of the vesicle relative to a sphere of the same volume. For strong enough flows, small-wavelength deformations like wrinkles are observed, similar to what happens in a suddenly reversed elongational flow. We investigate these questions further in the chapters 4, 5, and 6.

Chapter 4: Undeformable vesicles. The TT-TB transition at very low shear rates is well described by the Keller-Skalak (KS) model, which assumes fluid vesicles of constant ellipsoidal shapes. The dynamics of the vesicle is then described by only two variables, namely the orientation angle of the vesicle's long axis relative to the direction of the flow, and a phase angle measuring the displacement of a membrane point with respect to its equilibrium position. The Skotheim-Secomb (SS) model generalises the KS model by including an elastic energy which depends periodically on the phase angle thus modelling the shape memory of red blood cells. In this chapter, we add consistently thermal noise to these two models and derive analytically stochastic equations of motion. We solve the corresponding Fokker-Planck equations to obtain the steady-state probability distributions. We then construct dynamical phase diagrams for objects with dimensions accessible in experiments.

For fluid vesicles, the KS model predicts a transition between TT and TB at fixed viscosity contrast independently of the shear rate. With thermal fluctuations, this

transition depends on the shear rate. In particular, at small shear rates thermal fluctuations become dominant. As a result, a TB motion is observed for any viscosity contrast since vesicles then undergo a biased random walk. Intermittent TB rotations happen in the TT regime close to the transition. For elastic vesicles, the SS model predicts an oscillation of the inclination angle in the TT regime which is then called swinging (SW). Moreover, an intermittent (INT) regime appears in which SW and TB periods alternate. The transition between these regimes depends not only on the viscosity contrast, but also on the shear rate and on the elastic energy. With thermal fluctuations, the INT regime occupies a much larger region in the phase diagram. In particular, it appears also for parameters at which a direct SW-TB transition is predicted by the deterministic model, since then SW and TB have comparable energies and are thus mixed by thermal noise.

Chapter 5: Trembling regime. Shape deformations are taken into account in analytical models for quasi-spherical vesicles, i.e. vesicles with small excess area. In these models, the vesicle shape is expanded in spherical harmonics. Equations of motion for the expansion coefficients are then obtained by solving the Stokes equations inside and outside the vesicle and matching the solution at the virtual sphere of the same volume. Without thermal noise, three motions are predicted: TT, TB, and at their transition vacillating-breathing (VB), which consists in a periodic oscillation of the orientation angle accompanied by symmetric deformations. This VB motion is in strong disagreement with the experimental TR motion, in which strong asymmetric deformations are observed during the noisy oscillation of the orientation angle. A detailed analysis of experimental data shows that this long-standing discrepancy is probably due to the absence of thermal fluctuations in the previous models.

Here, we present a model for quasi-spherical vesicles in linear flow which consistently includes thermal fluctuations. Corrections coming from the third-order expansion of the bending energy are also taken into account. Our model correctly predicts the experimental TR motion in a quantitative way. The reason is that thermal fluctuations are amplified when the vesicle takes negative orientation angles. Then, asymmetric deformation modes can become larger than ellipsoidal ones, which are the only relevant ones in the deterministic VB motion. The shapes predicted by our model match experiments very well . Moreover, the deformation power spectra from our numerical results show the same features as the experimental ones. The predicted phase diagram too is in good agreement with experiments, emphasizing the fact that thermal noise is crucial for the flow dynamics of vesicles.

Chapter 6: Wrinkling instability. Vesicles exposed to a pure elongational flow adopt a steady ellipsoidal shape aligned with the flow. If the flow direction is

suddenly rotated by 90°, the vesicle tips are compressed and small-wavelength deformations appear for strong enough flows. These wrinkles are only transient because vesicles then relax to a new equilibrium shape perpendicular to the original one. In steady linear flow, vesicles are ellipsoidal at positive orientation angles but experience compression when this angle becomes negative, i.e. in TR and TB regimes. Then, wrinkles may appear if the flow rates are large enough.

In this chapter, we present experimental observations of such a wrinkling instability in the TR regime which are explained analytically and numerically. We extend the model used in chapter 5 to include hydrodynamics corrections describing the external flow not at a virtual sphere, but rather at the actual position of the membrane. The main parameter controlling the wrinkling instability is the strength of the elongational part of the flow, even though the flow vorticity and the vesicle excess area play a role as well. Like for the TR regime, thermal fluctuations are of crucial importance. Without them, our model fails to predict the appearance of wrinkles, whereas the results with thermal noise exhibit deformations comparable to the experimental ones. These deformations can be divided in symmetric and asymmetric contributions. The symmetric deformations evolve almost periodically with half the period of the orientation oscillations, both in experiments and stochastic simulations. In contrast, the asymmetric deformations are only slightly correlated with the orientation angle since they are caused directly by random thermal noise. The numerical simulations, however, tend to underestimate the experimental measurements due to the quasi-spherical approximation. Nevertheless, the agreement between theory and experiments is still very good and shows once again that thermal noise cannot be neglected even for strong flows.

1. Introduction

The frontier between biology, chemistry, and physics is blurry at the microscopic scale. The biological function of objects like proteins, polymers, or cells is determined by the chemical reactions and physical forces to which they are subject. For instance, red blood cells (RBCs) are not only responsible for the transport of oxygen in the body, but they also regulate blood pressure by releasing adenosine triphosphate (ATP) to induce the dilatation of blood vessels [1]. The ATP production, which happens through complex chemical reactions, is increased when RBCs are exposed to high shear stresses, i.e. when they are subject to strong deformations [2]. This example among many others explain why the interdisciplinary science of the "middle world" [3] has become a major research field from the second half of the twentieth century on.

From the point of view of physics, the study of such microscopic objects constitutes the field of *soft matter*, a term coined by M. Veyssié in the 70's [4] and later popularized by Nobel-prize winner P.-G. de Gennes [5]. The term *soft matter* describes microscopic objects which are strongly affected by the thermal agitation of the surrounding smaller molecules. A paradigmatic example is the random motion of pollen grains at the surface of quiescent water observed by R. Brown in 1827 [6]. The mathematical and physical description of this *Brownian motion* by Einstein [7], Smoluchowski [8], Langevin [9], and Perrin [10] provides the basis for the study of colloids [11], polymers [12], and membranes [13, 14].

One particularly interesting kind of soft matter objects are vesicles (also known as liposomes). Vesicles are microscopic bags filled with liquid and often suspended in an aqueous solution. Their size ranges from tens of nanometres to hundreds of micrometers. Their membrane is made up of amphiphilic lipids, i.e. lipids with a hydrophobic tail and a hydrophilic head, which are arranged in a closed bilayer such that the tails are not in contact with the surrounding water, see Fig. 1.1. They may form spontaneously in a lipid solution, and have therefore been proposed as primordial cells crucial to the origin of life [15]. Biological cells produce vesicles by membrane budding, using them for intra- and extracellular communication, for example in the exchange of neurotransmitters between neurons (see Nobel Prize for Medicine 2013 [16]) or the defence of marine bacteria against external viruses [17]. Vesicles can also be produced artificially to serve as pharmaceutical carriers [18] or as cell-mimicking systems [19] since almost all biological cells possess a lipid membrane. In the latter case, giant unilamellar vesicles (GUVs)

are used that typically have a radius of 1 µm to 100 µm, which is much larger than the membrane thickness of 5 nm. Therefore, the membrane can be considered as a two-dimensional surface enclosing a three-dimensional volume of fluid.

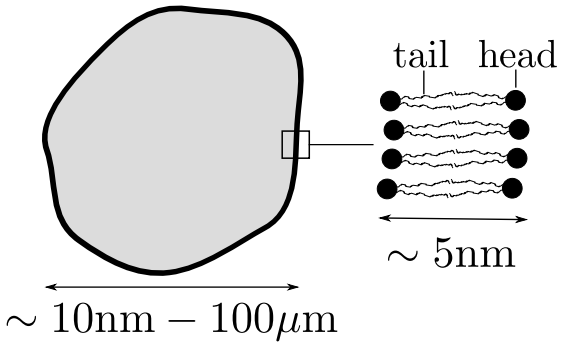

Figure 1.1.: Two-dimensional cross-section of a vesicle and structure of the lipid-bilayer membrane.

GUVs have become a paradigmatic soft matter system for different reasons. First, even in equilibrium, they exhibit an amazing variety of shapes. At fixed area and enclosed volume, these shapes result from the minimization of their total bending energy only [20–22] since shearing or stretching the membrane involve much larger energies than bending deformations. Systematic theoretical work in the 90's in combination with experiments using video microscopy has led to a quantitative understanding of how the subtle aspects of bilayer elasticity [22–24] determine the shape diagram, as comprehensively reviewed in [25]. Second, even though biological cells have a more complex architecture, vesicles have often served as a model system for anucleate cells such as red blood cells (RBC), whose equilibrium shapes can be predicted by minimising a generalised version of the vesicle bending energy [26]. Third, the behaviour of vesicles in external flow fields is determined by a complex interplay between membrane elasticity, hydrodynamic forces, and thermal fluctuations. Studying the resulting dynamics is fundamental for understanding more complex phenomena such as blood flow and more generally cellular transport in liquids.

In this thesis, we study the dynamics of single GUVs[1] in external flow, focussing on the importance of thermal fluctuations. In chapter 2, we recall the basics of fluid dynamics and Brownian motion, and the main properties of fluid vesicles. Chapter 3 constitutes a literature review on the flow dynamics of vesicles. The first part is dedicated to the dynamics in linear flows, constituting the basis for the rest of the thesis, while the second part deals with capillary flows and related questions. In chapter 4, we consider vesicles of fixed shape and show that thermal fluctuations play an important role at dynamical transitions. Moreover, we generalize the model by adding a membrane elastic energy mimicking the shape memory of red blood cells. For deformable vesicles, we show in chapter 5 that thermal noise creates a new dynamical regime which corresponds to experimental observations, thus resolving a long-standing discrepancy between numerical models and experimental

[1] We will use the terms "GUV" and "vesicle" interchangeably in the rest of this work.

results. In chapter 6, we generalise these results to stronger flows and find a wrinkling instability in steady flow which had previously been observed only in time-dependent elongational flow.

Publications

Parts of this thesis have been published previously:

- "Effect of thermal noise on vesicles and capsules in shear flow"
  D. Abreu and U. Seifert, Phys. Rev. E **86**, 010902(R) (2012)

- "Noisy nonlinear dynamics of vesicles in flow"
  D. Abreu and U. Seifert, Phys. Rev. Lett. **110**, 238103 (2013)

- "Fluid vesicles in flow"
  D. Abreu, M. Levant, V. Steinberg, and U. Seifert, Adv. Colloid Interface Sci., in print (2014), DOI: 10.1016/j.cis.2014.02.004

- "Wrinkling instability of vesicles in steady linear flow"
  M. Levant, D. Abreu, U. Seifert, and V. Steinberg, submitted (2014)

2. Basics

The vesicles we are interested in have typical sizes of 1 µm to 100 µm. At this length-scale, the aqueous solvent can be described as a continuum (section 2.1). Nevertheless, vesicles are small enough to feel the random forces caused by the thermal agitation of the surrounding water molecules (section 2.2). A basic physical description of vesicles is presented in section 2.3.

2.1. Hydrodynamics

We recall the basics equations of fluid dynamics which will be useful in the derivation of the models in sections 4 and 5. Due to small size of vesicles, viscous effects dominate over inertial ones leading to peculiar phenomena described in a classic article by E. M. Purcell [27]. Detailed considerations can be found in books on hydrodynamics at low Reynolds numbers [28–30].

2.1.1. Stokes equations

Consider an isothermal fluid as a continuous medium with density ρ flowing with the velocity $\mathbf{v}(\mathbf{r})$. The flow through a small, stationary volume within the fluid must obey both conservation of mass and of momentum. If the fluid is incompressible, its density ρ is constant and conservation of mass implies that the divergence of the flow vanishes

$$\nabla \cdot \mathbf{v} = \mathbf{0} \tag{2.1}$$

where ∇ is the vector differential operator and the dot represents the scalar product. We will further assume that the bulk viscosity of the fluid is zero and that its shear viscosity η is constant. Then, conservation of momentum leads to

$$\rho(\partial_t \mathbf{v} + (\mathbf{v} \cdot \nabla)\mathbf{v}) = -\nabla \hat{p} + \eta \nabla^2 \mathbf{v} + \rho \mathbf{F}_{\text{ext}} \tag{2.2}$$

where $\hat{p}$ is the hydrostatic pressure the fluid would support at rest and $\mathbf{F}_{\text{ext}}$ contains all external bulk forces such as gravity. The set of equations (2.1) and (2.2) are called the Navier-Stokes equations. They fully describe the flow of incompressible fluids under given boundary conditions.

Let L be a characteristic length of the system, U a characteristic velocity, and $T \equiv L/U$ the corresponding time-scale. If we neglect bulk forces, we can bring eq. (2.2) into the dimensionless form [28]

$$Re(\partial_{\tilde{t}}\tilde{\mathbf{v}} + (\tilde{\mathbf{v}} \cdot \tilde{\nabla})\tilde{\mathbf{v}}) = -\tilde{\nabla}\tilde{\hat{p}} + \tilde{\nabla}^2\tilde{\mathbf{v}} \tag{2.3}$$

where $Re \equiv \rho UL/\eta$ is the Reynolds number and the tilde indicates dimensionless variables. For small Reynolds numbers $Re \ll 1$, the inertial terms on the left-hand side of (2.3) can be neglected and the Stokes equations

$$\nabla\hat{p} = \eta\nabla^2\mathbf{v} \qquad\qquad \nabla \cdot \mathbf{v} = 0 \tag{2.4}$$

are obtained. For a vesicle of radius 10 µm suspended in water (viscosity of 10^{-3} Pa s) and subject to a shear flow with rate $1\,\mathrm{s}^{-1}$, i.e. $U \sim 10\,\mu\mathrm{m\,s}^{-1}$, the Reynolds number $Re \sim 10^{-4}$ is very low and the Stokes equations (2.4) apply. These equations are linear in velocity and pressure, such that any solution can be written as a linear superposition of fundamental solutions compatible with the boundary conditions. One particular basis for problems with spherical geometry is presented in section 2.1.2.

The momentum part of the Stokes equations (2.4) can be written in the form

$$\nabla \cdot \bar{\mathbf{\Pi}} = 0 \tag{2.5}$$

with the stress tensor

$$\bar{\mathbf{\Pi}} \equiv -\hat{p}\bar{\mathbf{1}} + \eta(\nabla \otimes \mathbf{v} + (\nabla \otimes \mathbf{v})^t) = (-\hat{p}\delta_{ij} + \eta(\partial_i v_j + \partial_j v_i))_{\{i,j\}} \tag{2.6}$$

where $\mathbf{1}$ is the unit tensor, $\otimes$ denotes the tensor product and the superscript ^{t} the transposition. Eq. (2.5) implies that, in Stokes flow, stresses balance at every point at all times since there is no inertia, i.e., no accelerations.

The total force exerted by a fluid on an object immersed in it is given by

$$\mathbf{F} = \int \bar{\mathbf{\Pi}}\mathbf{n}\,\mathrm{d}A \tag{2.7}$$

where $\mathbf{n}$ is the local normal vector pointing out of the object. Accordingly, the torque about the origin exerted by the fluid on the body is

$$\mathbf{M} = \int \mathbf{r} \times (\bar{\mathbf{\Pi}}\mathbf{n})\,\mathrm{d}A. \tag{2.8}$$

If the surface of the object moves at a speed $\mathbf{v}$ in the liquid, the rate at which the fluid applies work to the body is given by

$$\dot{W} = \int \mathbf{v} \cdot (\bar{\mathbf{\Pi}}\mathbf{n})\,\mathrm{d}A = \int \mathbf{n} \cdot (\bar{\mathbf{\Pi}}\mathbf{v})\,\mathrm{d}A. \tag{2.9}$$

If the object in question is a fluid volume, then Gauss's theorem leads to

$$\dot{W} = \int \nabla \cdot (\bar{\mathbf{\Pi}}\mathbf{v})\,\mathrm{d}V = \frac{\eta}{2}\int (\partial_i v_j + \partial_j v_i)^2\,\mathrm{d}V \equiv d \tag{2.10}$$

where d is the rate of mechanical energy dissipation in the fluid volume V [28].

2.1.2. Lamb's solution

One particular solution of eq. (2.4) exists in spherical coordinates [31]. We recall the main steps to derive this solution as presented in [28]. By taking the divergence of the first equation of eq. (2.4), one finds that the pressure field p obeys Laplace's equation

$$\nabla^2 \hat{p} = 0. \tag{2.11}$$

This suggests an expansion in solid spherical harmonics (see Appendix A)

$$\hat{p} = \sum_{l=-\infty}^{+\infty} \hat{p}_l. \tag{2.12}$$

The general solution then takes the form

$$\mathbf{v} = \sum_{\substack{l=-\infty \\ l\neq -1}}^{+\infty} \left[\nabla \times (\mathbf{r}\chi_l) + \nabla\varphi_l + \frac{l+3}{2\eta(l+1)(2l+3)} r^2 \nabla \hat{p}_l - \frac{l}{\eta(l+1)(2l+3)} \mathbf{r}\hat{p}_l \right] \tag{2.13}$$

where the velocity $\mathbf{v}$ and the solid spherical harmonics $\hat{p}_l$, χ_l, and φ_l all depend on the position vector $\mathbf{r} = r\mathbf{e}_\mathbf{r}$.

If boundary conditions are prescribed at a sphere of radius R, then the solid spherical harmonics can be expressed as

$$f_l(\mathbf{r}) = \sum_{m=-l}^{l} f_{lm} \left(\frac{r}{R}\right)^l \mathcal{Y}_{lm}(\theta, \phi) \tag{2.14}$$

where $f \in \{\hat{p}, \chi, \Phi\}$ and $\mathcal{Y}_{lm}$ are the spherical harmonics defined in eq. (A.5). To determine the expansion coefficients $\{\hat{p}_{lm}, \chi_{lm}, \varphi_{lm}\}$ from the boundary conditions, we consider the velocity field $\mathbf{V} \equiv \mathbf{v}(R, \theta, \phi)$ at the sphere $r = R$ and define the quantities

$$X(\theta,\phi) = \mathbf{V} \cdot \mathbf{e}_\mathbf{r} \ , \quad Y(\theta,\phi) = -r\nabla \cdot \mathbf{V}|_{r=R} \ , \quad Z(\theta,\phi) = \mathbf{r} \cdot (\nabla \times \mathbf{V})|_{r=R} \tag{2.15}$$

which are expanded in spherical harmonics as $X(\theta,\phi) \equiv \sum_{l,m} X_{lm}\mathcal{Y}_{lm}(\theta,\phi)$ (Y and Z are expanded in a similar fashion). For the flow in the interior of the sphere, only terms with $l \geq 1$ are retained ($l = 0$ does not contribute) in the expansions in order to avoid divergences of the velocity [28]. Similarly, if the flow exterior to the sphere must vanish or take a constant value at infinity, only harmonics with $l \leq -2$ have to be considered.

For the vesicles considered in chapter 5, the boundary conditions at the sphere are not fixed. We can nevertheless use the expansion described above for the interior and exterior velocity fields and match them at $r = R$. However, to fully solve the problem, we must also match hydrodynamic stresses and interface stresses (if any) at the sphere. The hydrodynamic stress vector is given by

$$\mathbf{T} = \mathbf{e_r} \cdot \bar{\mathbf{\Pi}} = -\hat{p}\mathbf{e_r} + \eta \left(\frac{\partial \mathbf{v}}{\partial r} - \frac{\mathbf{v}}{r} \right) + \frac{\eta}{r} \nabla (\mathbf{r} \cdot \mathbf{v}). \tag{2.16}$$

2.2. Brownian motion

Since they are microscopic objects, vesicles are subject to thermal fluctuations. The influence of these fluctuations is described by the Langevin equation or equivalently the Fokker-Planck equation [32, 33]. We first recall these equations in one dimension in section 2.2.1 before generalising the formalism to arbitrary many dimensions in section 2.2.2.

2.2.1. One dimension

The erratic motion of microscopic particles in water, known as Brownian motion, is described in one dimension by the Langevin equation

$$m\ddot{x} + \gamma\dot{x} = F(x,t) + \xi(t) \tag{2.17}$$

which is Newton's second law supplemented by a random force ξ modelling hits of water molecules against the Brownian particle. Here, m is the mass of the colloid, γ is the friction coefficient, and $F(x,t) \equiv -\partial_x V(x,t) + f(x,t)$ the sum of conservative forces coming from the total potential $V(x,t)$ and non-conservative ones $f(x,t)$ [34]. The random force $\xi(t)$ is a Gaussian white noise obeying the relations

$$\langle \xi(t) \rangle = 0 \ , \qquad \langle \xi(t)\xi(t') \rangle = 2\gamma k_\mathrm{B} T \delta(t - t') \tag{2.18}$$

where the brackets indicate the ensemble average over many realisations.

For overdamped systems, inertial terms can be neglected and the Langevin equation becomes

$$\dot{x} = \mu F(x,t) + \zeta(t). \tag{2.19}$$

where $\mu \equiv 1/\gamma$ is the mobility and the noise term $\zeta(t)$ obeys

$$\langle \zeta(t) \rangle = 0 \ , \qquad \langle \zeta(t)\zeta(t') \rangle = 2\mu k_\mathrm{B} T \delta(t - t') \equiv 2D\delta(t - t'). \tag{2.20}$$

The equality

$$D = \mu k_{\mathrm{B}} T \tag{2.21}$$

is the fluctuation-dissipation theorem and relates the diffusion and friction properties of the colloid. This Langevin equation is equivalent to the Fokker-Planck equation [32, 33]

$$\partial_t p(x,t) = -\partial_x(\mu F(x,t)p(x,t)) + D\partial^2_{x^2} p(x,t) \equiv -\partial_x j(x,t) \tag{2.22}$$

which gives the time-evolution of the probability density $p(x,t)$ of finding a particle at position x. The probability current $j(x,t)$ is constant for stationary probability distributions satisfying $\partial_t p(x,t) = 0$, i.e. $\partial_x j(x,t) = 0$. We will distinguish the equilibrium distribution $p^{\mathrm{eq}}(x)$ corresponding to a vanishing current from the stationary distribution $p^s(x)$ of a steady state with non-zero current, also called non-equilibrium steady state (NESS).

2.2.2. Arbitrary dimension

The overdamped Langevin equation (2.19) can be generalized to arbitrary many dimensions [33]. Let $\mathbf{x} = (x_1, x_2, ..., x_N)$ be the vector formed by N random variables obeying

$$\dot{x}_i = b_i(\mathbf{x}) + b_{ij}(\mathbf{x})\zeta_j(t) \tag{2.23}$$

where the b_i and b_{ij} do not depend explicitly on time and summation over repeated indices occurs. The Gaussian white noises ζ_i obey

$$\langle \zeta_i(t) \rangle = 0 \ , \qquad\qquad \langle \zeta_i(t)\zeta_j(t') \rangle = \delta_{ij}\delta(t-t'). \tag{2.24}$$

The set of Langevin equations (2.23) for $i \in [1, N]$, interpreted in the Stratonovich convention, is equivalent to the multidimensional Fokker-Planck equation

$$\partial_t p(\mathbf{x},t) = -\frac{\partial}{\partial x_i} D_i(\mathbf{x}) p(\mathbf{x},t) + \frac{1}{2}\frac{\partial^2}{\partial x_i x_j} D_{ij}(\mathbf{x}) p(\mathbf{x},t) \equiv -\frac{\partial j_i(\mathbf{x},t)}{\partial x_i} \tag{2.25}$$

for the probability distribution $p(\mathbf{x},t)$, where

$$j_i(\mathbf{x},t) = D_i(\mathbf{x})p(\mathbf{x},t) - \frac{\partial}{\partial x_j} D_{ij}(\mathbf{x}) p(\mathbf{x},t) \tag{2.26}$$

are the probability currents and $D_i(\mathbf{x})$ and $D_{ij}(\mathbf{x})$ the drift and diffusion coefficients, respectively. These coefficients are given by (see Ref. [33], p.55)

$$D_i(\mathbf{x}) = b_i(\mathbf{x}) + b_{kj}(\mathbf{x})\frac{\partial b_{ij}(\mathbf{x})}{\partial x_k} \tag{2.27}$$

where the second term on the right-hand side corresponds to a spurious drift coming from a position-dependent noise amplitude, and

$$D_{ij}(\mathbf{x}) = b_{ik}(\mathbf{x})b_{jk}(\mathbf{x}). \tag{2.28}$$

Stationary distributions obeying $\partial_i j_i(\mathbf{x}, t) = 0$ are only equilibrium ones if all currents vanish.

2.3. Fluid vesicles

We first describe basic properties of vesicles in section 2.3.1 before introducing the bending energy in section 2.3.2.

2.3.1. Physical description

Vesicles enclose an internal liquid of viscosity η_i and are suspended in an outer liquid of viscosity η_o, defining the viscosity contrast

$$\lambda \equiv \eta_i/\eta_o. \tag{2.29}$$

The lipid bilayer is often in a liquid phase at room temperature, with a surface viscosity of about 10^{-8} to $10^{-9}\,\mathrm{Pa\,s\,m}$ [35–40]. Typically, the membrane can be considered incompressible since the number of lipids in it is constant and the stretching energy is very large [41]. Therefore, the total membrane area A is constant. Moreover, the membrane is permeable to water but impermeable to many other molecules. For a vesicle in equilibrium, any influx of water creates an osmotic pressure which is relaxed by an outflux of the same magnitude [21]. In experiments, even when a small net flow exists, volume changes occur on a time-scale of several hours, which is much longer than the typical experimental time-scale of about 10 to 15 minutes. We can thus consider the vesicle volume V to be constant as well. From the volume, we define the effective radius

$$R_0 \equiv (3V/4\pi)^{1/3}, \tag{2.30}$$

which is the radius of a sphere of the same volume. Relatively to this sphere, the vesicle has the excess area [1]

$$\Delta \equiv A/R_0^2 - 4\pi \geq 0. \tag{2.31}$$

[1] Some authors define an effective radius over the area as $R_0' \equiv \sqrt{A/4\pi}$ and a reduced volume $\nu \equiv V/(4\pi {R_0'}^3/3) \leq 1$. The excess area is then given by $\Delta = 4\pi(\nu^{-2/3} - 1)$.

Since the radius of GUVs (∼10 µm) is much larger than the membrane thickness (∼5 nm), the membrane can be modelled as a two-dimensional surface [14, 42]. Using the notation of [41], the membrane is parametrized as $\mathbf{R}(s_1, s_2)$ with two internal coordinates s_1 and s_2. The tangential vectors

$$\mathbf{R}_i \equiv \partial_i \mathbf{R}(s_1, s_2) \quad , \; i = s_1, s_2 \tag{2.32}$$

define the metric tensor

$$g_{ij} \equiv \mathbf{R}_i \cdot \mathbf{R}_j \tag{2.33}$$

whose determinant g yields the surface element

$$\mathrm{d}A = \sqrt{g}\, \mathrm{d}s_1\, \mathrm{d}s_2. \tag{2.34}$$

The normal vector

$$\mathbf{n} \equiv \frac{\mathbf{R}_1 \times \mathbf{R}_2}{|\mathbf{R}_1 \times \mathbf{R}_2|} \tag{2.35}$$

serves to define the curvature tensor

$$h_{ij} \equiv (\partial_i \partial_j \mathbf{R}) \cdot \mathbf{n} \tag{2.36}$$

from which the mean curvature

$$H \equiv \frac{1}{2} h_i^i \tag{2.37}$$

and the Gaussian curvature

$$K \equiv \det(h_j^i) \tag{2.38}$$

follow, where $h_j^i = g^{ik} h_{kj}$. As an example of parametrization, the radius of quasi-spherical vesicles can be parametrized as

$$R(\theta, \phi) \equiv R_0 \left(1 + \sum_{l,m} u_{lm} \mathcal{Y}_{lm}(\theta, \phi) \right) \tag{2.39}$$

where $\mathcal{Y}_{lm}(\theta, \phi)$ are the spherical harmonics from eq. (A.5), and θ being the polar and ϕ the longitudinal angle in spherical coordinates. All geometrical quantities can then be expressed as a function of the expansion coefficients u_{lm}.

2.3.2. Bending energy

Bending deformations involve much lower energies than stretching and shearing ones which can be neglected [25]. The bending rigidity κ is typically between 10^{-20} J to 2×10^{-19} J (approximately $2 - 50 k_B T$ at room temperature) [25, 36, 37, 43]. The simplest energy functional describing bending deformations corresponds to the Helfrich energy [20–22]

$$\mathcal{H} = \int dA \left[\frac{\kappa}{2} (2H - C_0)^2 + \kappa_G K \right] \tag{2.40}$$

where κ_G is the bending energies associated with the Gaussian curvature K and C_0 a spontaneous curvature reflecting bilayer asymmetry. For simplicity, we will set $C_0 = 0$ in this thesis. Moreover, for a closed membrane, the integral over K is constant and is therefore not relevant for vesicles of fixed spherical topology [25]. The bending energy of the membrane reduces thus to

$$\mathcal{H}_\kappa = \frac{\kappa}{2} \int dA \left[(2H)^2 + \frac{\sigma}{R_0^2} \right], \tag{2.41}$$

where we introduced the position-dependent surface tension σ, a Lagrange multiplier that ensures local and global area conservation. Unlike for droplets, σ is here a dynamical variable, analogous to pressure for three-dimensional fluids, which adjusts itself to compensate external stresses. From the bending energy (2.41), we derive the local force density

$$\mathbf{f}(\mathbf{r}) = - \int \mathrm{d}A \left(\frac{1}{\sqrt{g}} \frac{\delta \mathcal{H}_\kappa}{\delta \mathbf{R}} \right) \delta(\mathbf{r} - \mathbf{R}(s_1, s_2)) \tag{2.42}$$

that the membrane exerts on the surrounding fluid. This force density compensates hydrodynamic stresses at every point of the membrane.

3. Fluid vesicles in flow: a review

In this chapter, we review the results on the question of vesicle dynamics in various types of flow. We first review the general theoretical, numerical, and experimental methods used to address this problem. Then, we consider the case of planar linear flow which will serve as a basis for the rest of this work. Afterwards, we describe the effect of walls and capillary flows on single vesicles, and discuss hydrodynamic interactions and the rheology of vesicle suspensions. Finally, we present related questions on the non-equilibrium dynamics of vesicles and similar objects. This chapter is based on the review article [44].

3.1. Methods

We present the theoretical tools for describing the dynamics of vesicles under hydrodynamic flows, then the techniques used in direct numerical simulations, and finally the experimental setups.

3.1.1. Theoretical modelling

The basic modelling of fluid vesicles was presented in section 2.3. The method to investigate theoretically the flow dynamics of vesicles is, in principle, quite straightforward. The Stokes equations (2.4) must be solved for the inner and outer fluids. The velocities and stresses are then matched at the membrane with no-slip boundary conditions and under the constraints of membrane incompressibility and impermeability, i.e. constant volume and surface area. Hydrodynamic stresses are given by eq. (2.16). Membrane stresses, given by eq. (2.42), arise on one hand from bending deformations and on the other hand from the incompressibility of the membrane. However, in order to derive analytical results, one needs further simplifying assumptions.

One strategy consists in describing the dynamics effectively with only a few degrees of freedom [45–51]. These models are based on the Keller-Skalak (KS) model [45], which assumes vesicles of fixed ellipsoidal shape with fluid membrane. Their dynamics in shear flow is then described by only two variables: the inclination angle Θ of the long axis of the vesicle relative to the flow direction, and the angle

$\tilde{\Phi}$ describing the displacement of a membrane element (see fig. 3.2 below). Deformations and thermal fluctuations can also be included in an effective way in such schemes [48, 51]. This approach is used in chapter 4.

Another strategy relies on looking at quasi-spherical vesicles, i.e., vesicles with small excess area $\Delta \ll 1$ [41, 52–58]. The radius of such vesicles can be parametrized by spherical harmonics as in eq. (2.39). Then, the inner and outer pressure and velocity fields are given by Lamb's solution of the Stokes equations, see section 2.1.2. The main approximation is to match these fields not at the membrane, but rather at the virtual sphere of radius R_0 [25] defined in eq. (2.30). This scheme can be applied in a perturbative way to analyse larger distortions from the spherical shape [56, 59, 60]. Moreover, thermal fluctuations can also be easily included [41, 58, 61, 62]. The results of chapters 5 and 6 are based on such a quasi-spherical expansion.

Of course, the equations obtained in such ways often have to be solved numerically [50, 51, 58, 60, 63–65]. However, we will distinguish numerical solutions of perturbative equations from direct numerical simulations as discussed in the next section.

3.1.2. Numerical approaches

Analytical models are either effective models or apply only in the quasi-spherical limit. Therefore, one has often to resort to direct numerical simulations to make quantitative predictions that can be compared to experiments. These numerical models either treat the fluids and the membrane on a continuum-level or model parts of the system as effective particles (see the review [66] for RBCs).

In continuum-based models, the hydrodynamic equations are directly solved. The boundary-integral method [29, 64, 67–84] uses Green's tensor formalism to calculate velocity fields. These are deduced by integration of the membrane forces over the vesicle surface. In this scheme, one does not need to follow explicitly the boundary of the vesicle. Moreover, the calculated velocity field obeys the Stokes equations per definition. Recently, spectral methods [73, 78, 85–87] have increased the accuracy of such simulations. However, the boundary-integral method is limited to Stokes flows and cannot include inertial effects. Other continuum-based methods offer more flexibility for including inertial and non-linear effects. Immersed-boundary algorithms [88–91] use the similarity of hydrodynamics and elasticity equations to simulate incompressible visco-elastic bodies immersed in incompressible fluids. The advected-field or phase-field method [92–94] replaces the membrane by a continuous field which varies strongly at the boundary between inner and outer fluids. Another continuum-based numeric schemes include level-set [95–97] and front-tracking [98, 99] methods. One important drawback of continuum-based models is that they fail to take thermal fluctuations into account,

since methods existing for flat membranes [100] have not been yet generalized to vesicles. This deficiency, which may seem negligible since $\kappa/k_BT \gtrsim 25$, explains why such models fail to predict the trembling motion observed experimentally, see section 3.2.2.

Particle-based methods define effective particles that interact in such a way that the actual equations of motion are recovered. Lattice-Boltzmann algorithms [101–104] discretise the fluids while keeping a continuum description of the membrane. These are, however, limited to two-dimensional models without thermal fluctuations. In the stochastic Euler-Lagrangian method [105], the equations of fluctuating hydrodynamics are solved while the membrane is coarse-grained. Dissipative particle dynamics can also include thermal fluctuations [106]. However, both methods have not been yet applied to vesicle dynamics. More interestingly, the multi-particle collision dynamics method [48, 50, 62, 64, 65, 107–112] takes hydrodynamic interactions, membrane properties, and thermal fluctuations into account. This numerical scheme is very flexible and allows to simulate complex flow geometries and many-body problems.

3.1.3. Experimental setups

Most experiments use dioleyol-phosphatidylcholine (DOPC) vesicles whose membrane is fluid at room temperature [113]. There are a lot of methods to produce them [19]. Due to their size, GUVs can be directly observed with phase-contrast microscopes (e.g. [113]). Epifluorescent microscopy is used to better detect and analyse the vesicle shape [114]. There, fluorescent lipids are added to the vesicle membrane during its formation. Both methods allow only to observe a two-dimensional cut of the three-dimensional vesicle. Three-dimensional images can be obtained either by confocal laser scanning microscopy [40, 115, 116] or by mechanical scanning of the narrow focal plane [117]. However, such scanning cannot be applied to monitor fast dynamical changes such as local shape perturbations. Markers can be used to track membrane or fluid motion, for example when the vesicle tank-treads [40, 113, 114, 118].

Several methods exist to generate an external flow. The most straightforward one is to generate a laminar flow in a micro-channel of rectangular section. This flow is parabolic but can be approximated to a linear shear close to the walls. Depending on the experimental question, vesicles can be exposed to a pure shear flow [40, 114, 115, 119–126] or to a Poiseuille flow [72, 127, 128] by properly adjusting the size of the micro-channel and the position of the vesicle in it. The channel can also be structured to investigate more complex geometries [110, 129]. One significant drawback of this method is that vesicles can only be observed for short periods since they flow. Observation periods can be slightly extended by placing a vesicle at the centre of a shear flow with zero mean velocity, either by

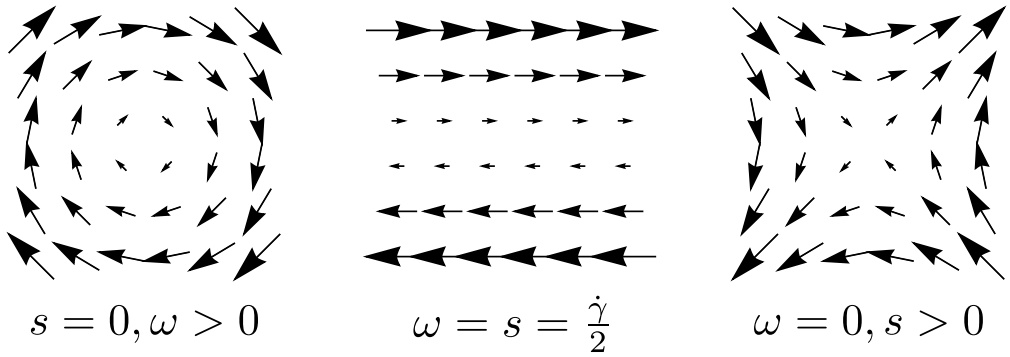

Figure 3.1.: A general linear flow is the sum of a rotational (left) and an elongational component (right). A shear flow (middle) corresponds to both components having the same magnitude.

moving two parallel walls [117] or two rotating cylinders [118, 130–132] in opposite directions with the same velocity. However, such setups introduce additional experimental difficulties since vesicles are positioned in an unstable location and tend to escape. The same remark applies to cross-slot micro-channels, which consist in two opposite inputs perpendicular to two opposite outputs, thus generating pure elongational flow [133, 134]. These stability limitations can be coped with by means of a closed-loop feedback system which corrects the flow. A significant improvement in observation periods is achieved in a micro-fluidic realization of the four-roll mill setup [135–139]. Such a setup allows to trap vesicles for observation periods significantly larger than the characteristic time-scales of their dynamics and generates a well-controlled general linear flow, see fig. 3.1.

3.2. Dynamics in linear flows

In this section, we consider unbounded planar linear flows, for which the unperturbed velocity profile in Cartesian coordinates has the form

$$\mathbf{v}^{\infty} \equiv s(y\mathbf{e_x} + x\mathbf{e_y}) + \omega(y\mathbf{e_x} - x\mathbf{e_y}) \tag{3.1}$$

in each plane with constant z, where $\mathbf{e_x}$ and $\mathbf{e_y}$ are the basis vectors of the (xy)-plane. The elongational flow of strength s tends to stretch the vesicle along the $(y = x)$-direction, while the rotational flow of vorticity ω causes rigid-body-like rotation. Varying s and ω leads to different types of flow; for example, setting $\omega = s \equiv \dot{\gamma}/2$ gives a linear shear flow with shear rate $\dot{\gamma}$, see fig. 3.1. Apart from the excess area Δ and the viscosity contrast λ defined in section 2.3.1, a third parameter, the capillary number

$$C_a \equiv \dot{\gamma}\eta_o R_0^3/\kappa \tag{3.2}$$

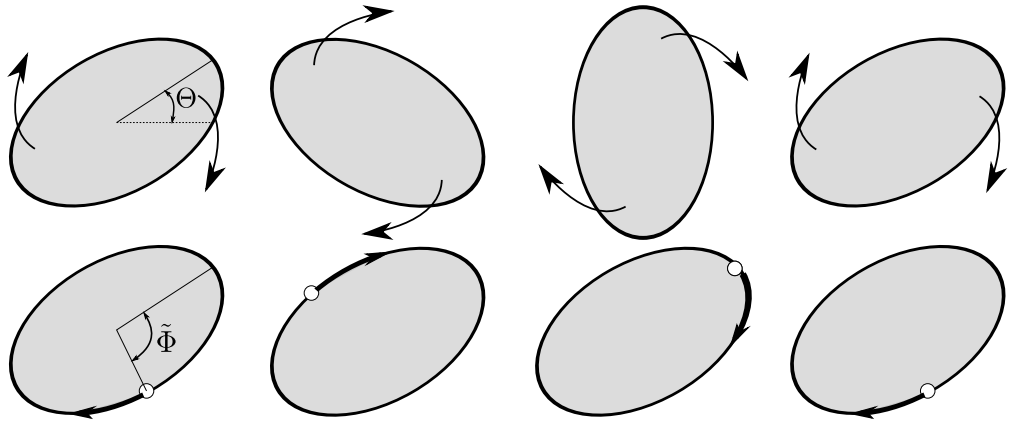

Figure 3.2.: Tumbling (top) and tank-treading (bottom) motions of an ellipsoidal vesicle. Θ is the inclination angle of the long axis of the vesicle, while $\tilde{\Phi}$ measures the displacement of a membrane element relative to this orientation.

will be important for the dynamics of a vesicle in linear flow. This dimensionless quantity compares the time-scale $1/\dot{\gamma}$ of the external flow with the relaxation time $\eta_o R_0^3/\kappa$ of bending deformations, where η_o is the external viscosity, R_0 the effective radius, and κ the bending energy (see section 2.3.1). The capillary number thus quantifies the relative strength of hydrodynamic forces to bending ones. The characterization of the vesicle dynamics is in most cases done by looking at the projection of the vesicle shape in middle flow plane, that is, the plane with constant z containing the centre of mass of the vesicle. Of course, due to the constraints of constant volume and area, three-dimensional deformations occur if the vesicle deforms in the (xy)-plane but the dynamics is mostly characterized by what happens in this middle flow plane.

3.2.1. Tank-treading and tumbling

At low capillary numbers $C_a \ll 1$, the deformation of the vesicle remains small. The KS model [45] describes the two possible dynamical regimes, which were first observed in experiments with RBCs [140–143]. In the tumbling (TB) regime, the vesicle rotates as a whole like a rigid body, see fig. 3.2. In the tank-treading (TT) regime, the vesicle adopts a constant orientation in the flow plane (up to thermal fluctuations) while its membrane rotates around the interior fluid. The TT motion is a consequence of the membrane fluidity. In the KS model, TT happens below and TB above a critical viscosity contrast $\lambda_c(\Delta) \geq 1$, which is independent of the strength of the shear flow but decreases with increasing excess area Δ [80]. Whereas this does not hold for RBCs [86, 144–146], for which this model was originally conceived, it describes remarkably well the TT-TB transition for

fluid vesicles at low shear rates. The TT-TB happens at lower λ_c if the membrane viscosity is increased [147] since it contributes to an effective increase of the inner viscosity. Taking into account a possible slip between the two layers of the membrane also changes the critical viscosity contrast [148]. If we consider a general linear flow of the form (3.1), the TT-TB transition can be triggered at fixed viscosity contrast by increasing the relative strength of rotational to elongational flow ω/s. Therefore, contrary to experiments in pure shear flow, in which the viscosity contrast determines the dynamics, a four-roll mill experiment [136, 139] allows to explore different dynamical regimes with a single vesicle. We will, however, focus on the case of a pure shear flow to describe TB and TT.

The inclination angle Θ of the vesicle evolves in the KS model according to

$$\partial_t \Theta = -\frac{\dot{\gamma}}{2}\left(1 - B\cos(2\Theta)\right), \tag{3.3}$$

where $B > 1$ is a constant depending on the vesicle geometry, see eq. (4.22). This equation is obtained by first balancing the torques coming from the TT motion, the TB motion, and the external shear flow, and second by equating the work applied by the flow on the membrane with the energy dissipated inside the vesicle, see section 4.1.1. This equation describes relatively well the experimental TB motion [119, 122] and numerical results [74, 93], at least for small capillary numbers. For larger ones, corrections due to deformations are needed [74, 123]. Upon approaching the TB-TT transition, a critical slowing down of the TB frequency is observed [56, 122] because the transition is a saddle-node bifurcation. Models including thermal fluctuations show additional dynamical features [48, 51] which are supported to some extent by experimental observations [114, 122, 137].

In the TT regime, models and experiments have analysed mainly three characteristics: membrane velocity, vesicle deformation, and inclination angle. The membrane velocity can be measured by tracking markers on the membrane [122, 124] or in the fluid [118]. The membrane velocity is periodic in $\tilde{\Phi}$ (defined in fig. 3.2) [122, 124], in accordance with the KS model which predicts a constant rotation frequency $\partial_t \tilde{\Phi}$. Moreover, this rotation frequency is proportional to the shear rate [67, 124]. The KS model, however, does not allow for deformations. The vesicle deforms into an ellipsoid under the action of the elongational part of the flow. This deformation saturates at large shear rates because the excess area is limited and the membrane cannot be stretched. For quasi-spherical vesicles, the Taylor parameter $\mathcal{D} \equiv (l_l - l_s)/(l_l + l_s)$, with l_l and l_s being the lengths of the long and short axes, saturates at a value proportional to $\sqrt{\Delta}$ [41] in good agreement with experimental results [114, 130]. Finally, the inclination angle decreases with increasing viscosity contrast λ and increasing excess area Δ [114, 122]. Its value and the fluctuations around it are very well described by the analytical theory for quasi-spherical vesicles [41]. It is also noteworthy that recent direct numerical

simulations [74, 78, 98] show an excellent agreement with experiments in the TT as well as in the TB regime. Recently, the TT motion has been analysed as a means of propulsion in shear flow if the membrane bending rigidity varies locally [149].

In chapter 4, we include thermal fluctuations in the KS model and investigate their impact on the TT-TB transition at low capillary numbers. Moreover, we generalise the model to vesicles with elastic membranes as a model for RBCs.

3.2.2. Deformations and transition regime

For larger capillary numbers $C_a \sim 1$, vesicle deformation changes the dynamics. A new regime appears at the TT-TB transition which was first observed experimentally [122]. This transition regime called trembling (TR) is characterized by irregular oscillations of the vesicle orientation accompanied by strong and asymmetric shape perturbations [117, 122, 136, 137, 139]. In contrast, analytical models without thermal fluctuations predict a transition motion called vacillating-breathing (VB) in which the orientation angle oscillates around 0 while the shape deforms with the same period [55–57, 59, 150–152]. These models, based on the quasi-spherical expansion (2.39), consider only harmonics with $l = 2$ since they possess the $r \to -r$ symmetry of the flow and are the only ones excited to lowest order. Refined models including higher-order even harmonics [60, 78] and deterministic numerical simulations [74, 78, 98] also predict only periodic and symmetric motions.

These models ignore thermal noise because bending forces are much larger than thermal ones since $\kappa/k_BT \gtrsim 25$. However, a detailed experimental examination has shown an amplification of thermal noise in TR, which is characteristic of non-linear dynamical systems close to bifurcations such as the TT-TB one [139]. In particular, the aperiodicity of the orientation angle and the presence of odd harmonics [137, 139] cannot be explained by deterministic predictions [60, 74, 78, 98].[1] On the other hand, simulations and phenomenological models with thermal fluctuations show similarities with the experimental TR motion [48, 50, 64, 147].

In chapter 5, we present a stochastic model based on a quasi-spherical expansion which reproduces quantitatively the characteristics of the experimental TR motion. This model shows that thermal fluctuations are the reason for the discrepancy between the predicted VB motion and the observed TR one.

[1] The presence of odd harmonics in the deterministic simulations of Ref. [98] is, as the authors admit, only due to numerical errors so that they do not observe the experimental TR. However, for shear rates much larger than those used in experiments on TR, they observe higher-order even harmonics which are a feature of the wrinkling instability explained in section 3.2.5

3.2.3. Phase diagram

The theoretical model of Refs. [56, 151], based on a quasi-spherical expansion to lowest order and including next-order corrections for the bending energy only, predicts that the phase diagram of the system merely depends on the two parameters

$$S \equiv \frac{14\pi}{3\sqrt{3}} \frac{\eta_o R_0^3}{\kappa \Delta} s \qquad \Lambda \equiv \frac{23\lambda + 32}{24} \sqrt{\frac{3\Delta}{10\pi}} \frac{\omega}{s}. \tag{3.4}$$

In contrast, deterministic theoretical models [60, 74, 78, 98, 150, 153] taking next-order hydrodynamic terms or harmonics with $l > 2$ into account argue that a third parameter, e.g., the excess area Δ, is necessary. In particular, in pure shear flow, the reduced viscosity contrast Λ at which the TT-TR/TB transition happens should strongly depend on Δ [60, 74, 78]. Only for $\lambda = 1$ do the phase diagrams for various Δ plotted as function of S and Λ overlap (see fig. 4 of [60]). This theoretical dependence on three parameters is in strong discrepancy with experimental results. The experimental phase diagrams in pure shear flow [117], where $\omega/s = 1$ and λ is varied, and in general linear flow [136], where $\lambda = 1$ and ω/s is varied, are both well described in terms of S and Λ. Even if different values of Δ are distinguished, the scaling still holds [137]. Deterministic simulations suggest that experimental motions might be wrongly classified due to long transients [74, 78, 98], but these are not observed in long experiments [137, 139]. Here again, thermal fluctuations have a great impact on the theoretical phase diagram as shown in chapter 5.

At large flow rates, several additional dynamical features are predicted, yet to be observed experimentally. An analytical model [151] and numerical simulations [74, 78] predict a three-dimensional motion called kayaking (or spinning), in which the vesicle precesses like a spinning top. For high excess areas corresponding to that of a RBC ($\Delta = 5$), a recent analytical work predicts the existence of some peculiar deformation modes at flow parameters corresponding to VB/TR [81]. However, it is not clear whether these shapes subsist with thermal fluctuations. Moreover, shape deformations observed in [98, 154] include higher-order harmonics, which is due to the wrinkling instability discussed in section 3.2.5. At even higher shear rates, inertial effects become important. For instance, simulations [91, 95, 96, 99] show that inertia inhibits tumbling. Experiments on vesicles exposed to acoustic streaming near a bubble seem to indicate that membrane rupture occurs at very large shear stresses [155]. Such membrane rupture has, however, not yet been observed in linear flows at large flow rates.

3.2.4. Stationary elongational flow

Setting $\omega = 0$ in eq. (3.1), one obtains an elongational flow which stretches the vesicle along the $(y = x)$-axis. In contrast to droplets and elastic capsules, a

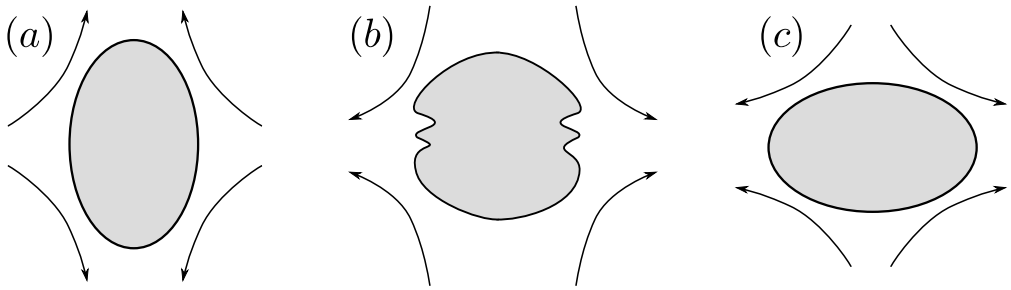

Figure 3.3.: Wrinkling instability in elongation flow. (a) The vesicle is stretched by the external flow into an ellipsoidal shape. (b) As the flow direction is inverted, the vesicle tips are compressed and transient wrinkles appear. (c) After relaxation, the vesicle is once again ellipsoidal.

vesicle deforms in such a flow only if it has a positive excess area $\Delta > 0$, since its area and volume are constant and a sphere is the only possible shape for $\Delta = 0$. For small excess areas, the vesicle deforms into an ellipsoid aligned with the flow, the deformation reaching a plateau at large elongation rates due to membrane incompressibility [63, 84, 133].

For large excess areas, a transition similar to the coil-stretch transition of flexible polymers [156] is found. Under a critical elongation rate, floppy tubular vesicles are only slightly stretched by the flow. Above the critical rate, they evolve into dumbbells connected by a thin tether whose length grows with the magnitude of the flow. At even higher flow rates, the tether becomes unstable and transient pearling configurations with different number of beads are observed until a stationary stretched dumbbell shape is established [134]. This phenomenon resembles somewhat the laser-induced pearling instability of tubular vesicles [157, 158]. In flow, the tubule-to-dumbbell transition is a continuous one accompanied by a slowing down of the dynamics and enhanced fluctuations close to the critical elongation rate, like for the coil-stretch transition of polymers [159]. This transition was observed recently in numerical simulations which showed asymmetric dumbbells and dynamical tether extension [84]. Such membrane nanotubes are used for intercellular communication or for directing the spread of viruses [160].

3.2.5. Time-dependent elongational flow

If the direction of the elongational flow is suddenly reversed, the transient phenomenon of vesicle wrinkling is observed [133], see fig. 3.3. The vesicle, which is initially stretched by the flow, is temporarily compressed after the flow reversal. This transient compression leads to an effective negative surface tension which amplifies harmonics with $2 < l < l_{max}$ where the highest mode l_{max} grows with the

flow strength [63]. Recent two-dimensional simulations [83] have shown qualitatively similar wrinkles, even though, contrary to experiments [133], odd harmonics are not observed due to the absence of thermal noise. This behaviour has clearly to be distinguished from the steady-state wrinkling of elastic capsules in elongation flow, which is due to the elasticity of the capsule membrane [161], whereas vesicles are in good approximation inelastic.

This phenomenon was recently observed experimentally in steady linear flow for trembling vesicles [154]. Due to the quasi-periodic oscillation of its orientation, a vesicle in TR motion is alternately stretched and compressed by the elongational part of the flow. Therefore, the surface tension becomes quasi-periodically negative and higher-order harmonics are excited. Contrary to the previous case, high-order modes do not necessarily decay fully until the next compression period, making the dynamics very complex. However, the mean wave-number of shape deformation depends on the flow strength in a similar fashion as in the case of time-dependent elongational flow [154].

In chapter 6, we show that thermal fluctuations are, like for the TR motion, crucial to explain the observed wrinkling in steady linear flow. Our model reproduces the most important features of the experimental wrinkling [154].

3.3. Walls, capillaries, and rheology

The study of vesicle dynamics is often cited as a first step to model blood flow [162]. In small capillaries, blood velocity has a parabolic profile also known as Poiseuille flow, see fig. 3.5. The maximal velocity, the degree of confinement, and the vesicle properties control the dynamics. Close to the walls, a Poiseuille flow can be approximated by a linear shear flow. We will thus first describe the dynamics of a single vesicle close to a wall in shear flow, before turning to Poiseuille flows, vesicle interaction, and rheology.

3.3.1. Influence of walls in shear flow

In linear shear close to a wall, a spherical object would move along with the flow while remaining at a constant distance from the wall because of the reversibility of the Stokes equations. One expects a transverse migration only for high Reynolds number due to the Magnus effect. In contrast, an object with broken fore-aft symmetry, such as a tank-treading vesicle with positive inclination angle, experiences a force pushing it away from the wall. In particular, a deformable vesicle sticking to a wall due to gravitational or adhesion forces is lifted by a strong enough flow, see fig. 3.4. By increasing the shear rate, the vesicle first deforms into an asymmetric shape and acquires a positive tilt, which increases with the

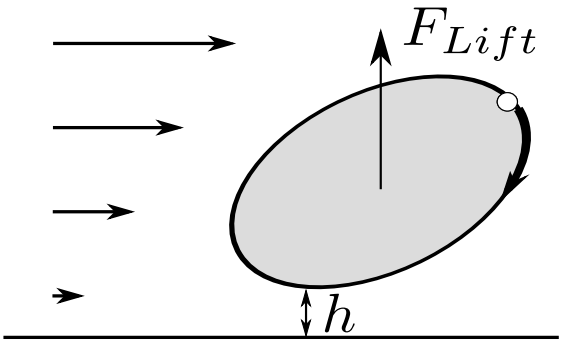

Figure 3.4.: Lift force acting on a TT vesicle in shear flow close to a wall.

shear rate. Above a critical shear rate, the vesicle is lifted and remains at a constant distance h from the wall where gravitation compensates the hydrodynamic lift [68, 70, 113, 115, 121, 163].[2] In the absence of gravitation, the vesicle drifts away from the wall with constant velocity [132]. Far from the wall, i.e., for $h > R_0$, the lift force scales with $\dot{\gamma}/h^2$, as predicted theoretically [53, 165] and observed in experiments [132] and numerical simulations [64, 70, 79]. Closer to the wall, the $\dot{\gamma}/h$ scaling observed in experiments [113, 121] is reproduced by recent numerical simulations [79]. Moreover, the lift force grows with increasing excess area Δ [53, 64, 113, 121]. This lift force may be responsible for the cell-free layers near the walls of blood vessels known as the Fåhraeus-Lindqvist effect [111, 121, 166] (see also the review article [167]).

For TB vesicles, the lift force was predicted to vanish since the motion is somewhat symmetric [168]. However, experiments with RBCs show that a lift force subsists in TB motion due to asymmetric deformations [169]. If the centre of the vesicle is closer to the wall than its radius, TB cannot happen. Even far enough from the wall, the TT-TB transition occurs at a higher critical viscosity contrast λ_c than in an unbounded flow because of the increased pressure between the wall and lower tip of the vesicle [64, 79]. A similar increase of λ_c is also observed in a shear flow confined between two walls, even if these walls are separated by a distance much larger than the vesicle radius [93, 101, 102]. More specifically, the closer the two walls are, the higher λ_c becomes. This factor might contribute to the shear thinning of blood in small capillaries [101, 102].

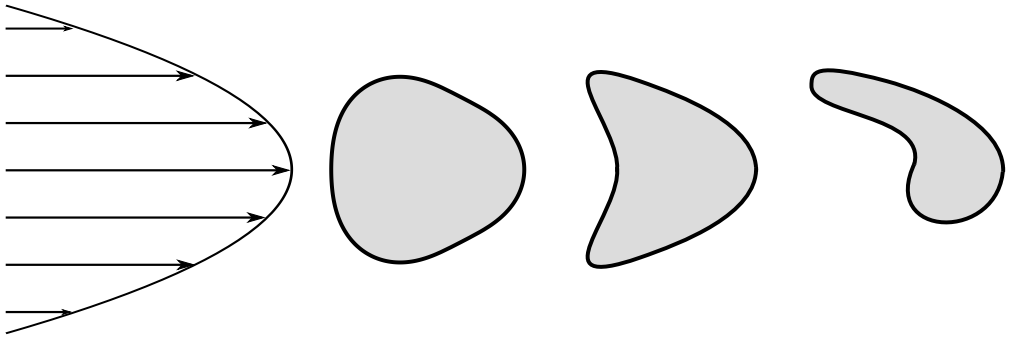

Figure 3.5.: Shapes of a vesicle in a Poiseuille flow (left) as predicted by [170]. For constant flow velocity, increasing the excess area Δ induces a transition from a bullet shape to a parachute one and then to an asymmetric, non-centered slipper.

3.3.2. Capillary flows

In a Poiseuille flow, vesicles migrate towards the tip of the flow where the shear rate is minimal [71, 72, 171]. [3] For low excess areas Δ, vesicles adopt a shape which is symmetric relative to the the axis of symmetry of the flow. Contrary to the case of linear flow, spherical harmonics with $l = 3$ are also excited to lowest order [168]. The two possible axisymmetric shapes are the bullet-like shape, with a convex rear end, and the parachute-like shape, with a concave rear end [127, 171]. For larger excess areas, these axisymmetric shapes become unstable and models predict an asymmetric off-centered slipper shape, which has already been observed for RBCs [107, 108, 170, 173, 174]. Fig. 3.5 shows some of the shapes that are predicted by the two-dimensional model of [170]. For slower flow rates as presented in this diagram, discoidal, prolate, or stomatocyte shapes are also predicted [107, 108, 174].

The previous results hold in unbounded flows. For small capillaries, confinement induces new effects, for example cross-streamline migration due to the wall lift force, see section 3.3.1. Vesicles migrate towards the centre due to the walls and to the flow profile, with a migration velocity proportional to $\dot{\gamma}(h)/h$, where $\dot{\gamma}(h)$ is the local shear rate at a distance h from the wall [72]. Once at the centre of the channel, vesicles move with the flow. Their velocity is then almost equal to the maximal velocity of the flow for low confinement, but much lower for strong confinement [127, 175]. In asymmetric channels, recent experiments show the existence of a croissant-like shape, for which the rear end is convex in

[2] The depinning dynamics of a settled vesicle have also been studied under an axisymmetric suction flow [164].

[3] If the flow were curved, however, the migration would be towards regions of higher curvature, i.e., higher shear rates [172].

one direction but concave in the perpendicular one [128]. Such three-dimensional effects cannot be captured by two-dimensional models, which, however, reproduce many experimentally observed features and make predictions that have not been tested yet in experiments [76]. A good agreement between models and experiments has been obtained for vesicles and RBCs flowing in micro-channels of oscillating width [110, 129]. In such channels, orientation and shape oscillations occur and asymmetric slipper-like shapes are observed.

3.3.3. Hydrodynamic interactions and rheology

Using the results obtained for quasi-spherical vesicles (see Sect. 3.2), the effective viscosity of a dilute suspension of vesicles in shear flow can be calculated [150, 176]. For TT vesicles, the analytical expression

$$\frac{\eta_{\text{eff}} - \eta_o}{\eta_o v_{\text{fr}}} = \frac{5}{2} - \frac{\Delta}{16\pi}(23\lambda + 32) \tag{3.5}$$

has been obtained [150], where η_{eff} is the effective viscosity of the suspension and v_{fr} the volume fraction of vesicles. The term $5/2$ corresponds to Einstein's correction for hard spheres. In these models, the effective viscosity first decreases with the viscosity contrast and reaches a minimum at the TT-TB transition ($\lambda_c > 1$), then grows with λ in the TB regime [150, 177–180]. While such a cusp has been observed in experiments with vesicles and RBCs [181], other experiments show that for $\lambda < 1$, η_{eff} rather increases with λ [125]. This discrepancy may come from the fact that rheological measurements of vesicle suspensions are complicated due to the wide dispersion of physical parameters of the constituents, such as size and excess area, and the inability to measure them directly. Therefore, individual objects in solution do not necessarily undergo the same dynamics, making the micro-macro relations much more complicated. Moreover, long-range hydrodynamic interactions between vesicles cause strong shape fluctuations even at relatively low volume fractions [125]. A way to determine the volume fraction at which a vesicle solution can be considered as dilute is to look first at the interaction between two vesicles [111, 138, 182–184]. Recent experiments show that hydrodynamic interactions are important for volume fractions larger than $v_{\text{fr}} = 0.08 - 0.13$, a result confirmed by the measurement of the back-reaction of a single vesicle on the ambient flow [138]. These interactions strongly influence the orientation and shape of the vesicles, in particular during crossing motions [111, 138, 180]. In addition, vesicles repel each other if they are in the same shear plane but hydrodynamic attraction can occur otherwise [184, 185].

For concentrated solutions in shear flow, shear-thinning happens because the cell-free layer at the walls grows with the shear rate in TT [111, 186]. In capillary flows, the effect of walls, shear gradient, and hydrodynamic interactions add up to

produce non-trivial vesicle migration dynamics [82]. Vesicles flowing at the centre of the channel form clusters due to hydrodynamic interactions if they come close enough to each other [187] similar to RBC clusters observed experimentally [188]. A transition between single files of parachute-shaped vesicles and a zigzag arrangement of slippers is predicted with increasing confinement and happens continuously due to thermal fluctuations [109, 174, 189].

3.4. Related questions

The dynamics of single vesicles in steady viscous flow is by now well understood. Many experimental observations have been successfully explained by models and simulations, even though the quantitative agreement between theoretical predictions and experimental results has to be improved, for example with the inclusion of thermal fluctuations and inertial effects in numerical models. Moreover, there are still a lot of questions to be answered as far as more complex setups are concerned. We briefly present some of these setups in the following.

Relaxation of stretched vesicles

A vesicle deformed by an external flow will relax back to its equilibrium shape once the flow is turned off. For vesicles relaxing from dumbbell to tubular shapes in elongational flow as described in section 3.2.4, relaxation times of several seconds have been found [134]. The same order of magnitude has been found with vesicles deformed by a strong uniform flow while trapped by optical tweezers [190] or directly deformed by optical tweezers [191]. This relaxation time also depends on the initial tension of the vesicle, as shown by experiments with vesicles point-attached to a solid substrate or to a moving particle [192]. In any case, the experimental relaxation times are an order of magnitude smaller than estimated from a model for quasi-spherical vesicles [56, 151], showing the need for a better modelling of these processes.

Time-dependent flow

In blood flow, RBCs do not experience a steady flow but rather an oscillatory one. Experiments on RBCs in oscillatory shear flow have been done [193–195], and among other features chaotic motions have been observed [195]. For vesicles, however, there are not so many studies in oscillatory shear flow. One experiment shows that fluctuations are suppressed by such a flow [120]. Numerical simulations for vesicles and capsules show complex dynamical regimes, in particular a delay between vesicle and flow dynamics and symmetry-breaking through thermal noise [196–198]. For dilute suspensions of vesicles, the effective viscosity is expected to

show resonances [199] similarly to what happens for elastic capsules [200]. These questions and many others still have to be investigated in time-dependent flows.

Dynamics of compound vesicles in linear flow

Compound vesicles are GUVs with another object inside. They are used to model the dynamics of cells having a complex internal structure such as white blood cells (WBCs). Recent simulations considering a solid inner particle of either spherical or elliptical shape show that new dynamical features in shear flow appear due to the hydrodynamic interaction between the inclusion and the membrane [77]. For example, the transition from TT to TB can occur in the absence of any viscosity contrast but at some critical value of the filling factor. Moreover, a vesicle can swing if the enclosed particle is non-spherical. A compound vesicle including another vesicle instead of a solid particle (referred to as bilamellar vesicle) demonstrates even more complex behaviour [103]. Experimental observations of such a vesicle in linear flow was realized in a four-roll mill device. While a compound vesicle can undergo the same TT, TR, and TB regimes as GUVs, a new swinging motion of the inner vesicle is found in TR in accord with simulations [201]. In addition, the inner and outer vesicles can exist simultaneously in different dynamical regimes and be either synchronized or unsynchronized depending on the filling factor. Multilamellar vesicles also deform and tank-tread in a complex fashion [126]. Whether these complicated models can mimic the dynamical behaviour of WBCs or whether one needs to take an additional non-Newtonian nature of the WBC and its nucleus (consisting of fibres, organelles, cytoplasm, etc...) into account remains an open question.

Role of spontaneous curvature and area-difference elasticity

Essentially all theoretical work for vesicles in flow has used the minimal model for curvature energy (2.41). Shape transformations in equilibrium are known to depend on a finer description with spontaneous curvature and/or area-difference elasticity [25]. These effects should also be investigated for vesicles in flow, in particular since work in other non-equilibrium situations [202–204] has shown their relevance. For instance, such bilayer effects might be important to explain the membrane budding observed in experiments in flow [133, 137].

Multicomponent flows

Numerical simulations [186, 205–207] and experiments [169] with only RBCs show shear-induced diffusion as well as the Fåhraeus-Lindqvist effect, i.e., the cell-free layer at the walls associated with a decrease in viscosity with the size of capillaries. Blood is, however, not only composed of RBCs but also of WBCs. In blood flow, it

is observed that RBCs migrate away from the walls while WBCs migrate towards them, a phenomenon known as margination [208]. Simulations of multi-component flows consisting of stiff and soft particles show that margination is probably due to this difference of stiffness [209–212]. Moreover, recent experiments use the wall-induced lift force discussed in Sect. 3.3.1 to efficiently separate cancer cells from RBCs [213]. One can therefore wonder whether such phenomena could be observed in suspensions of GUVs and compound vesicles.

Other setups and similar objects

Vesicles have also been studied under other non-equilibrium conditions. They move and deform under the influence of gravity [73, 214–218], electromagnetic fields [219–224], mechanical forces [191, 192, 225, 226], or pH-gradients [227]. Further investigation of such phenomena will constitute a basis for modelling the individual and collective behaviour of complex biological cells, as well as provide tools to understand the physics of microscopic non-linear systems.

Finally, many objects similar to vesicles have been studied under comparable conditions. Floppy vesicles with very low bending rigidity behave similarly to polymers [131, 228–230]. Ring polymers also tank-tread and tumble [231]. As opposed to vesicles, liquid droplets [232, 233] and capsules with visco-elastic membranes [112, 183, 234–241] respond in a linear fashion to shear flow since they can be stretched. Red blood cells also possess an incompressible bilayer membrane but are much less deformable than vesicles due to their cytoskeleton [143, 162, 242–244]. They exhibit not only TT and TB regimes, but also many other motions due to their elasticity [146]. Moreover, their membrane is much more complex than that of vesicles and they are sensitive to changes in ATP-concentration [245, 246]. The investigation of the dynamics of such objects will help understand to which extent vesicle properties can be generalized to other physical systems.

4. Undeformable vesicles in shear flow

For low capillary numbers, the transition between tank-treading (TT) and tumbling (TB) discussed in section 3.2.1 is well described by the Keller-Skalak (KS) model [45], which assumes vesicles of fixed ellipsoidal shape. This model has been extended by Skotheim and Secomb [145] to include the shape memory of red blood cells [247]. Based on these models, we investigate the influence of thermal fluctuations on the dynamics of vesicles in shear flow [51]. We first derive the equations of motion of the system, then focus on the case of vesicles with a purely fluid membrane, before analysing vesicles with a shape-memory, i.e. elastic membranes.

4.1. Reduced Model

In this section, we first recall the main features of the KS model [45] and its extension by Skotheim and Secomb [145], and then add thermal fluctuations consistently to the equations of motion.

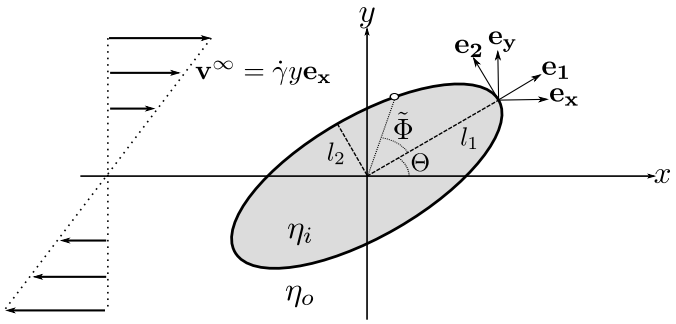

Figure 4.1.: Cross-section in the ($z = 0$)-plane of an ellipsoidal vesicle in shear flow and definition of the unit vectors $\mathbf{e_x}$, $\mathbf{e_y}$, $\mathbf{e_1}$, and $\mathbf{e_2}$.

4.1.1. Keller-Skalak model

We consider a vesicle of fixed ellipsoidal shape satisfying the equation

$$\frac{x^2}{l_1^2} + \frac{y^2}{l_2^2} + \frac{z^2}{l_3^2} = 1, \tag{4.1}$$

with main axes l_1, l_2, and l_3 and volume $V = 4\pi l_1 l_2 l_3/3$. The viscosities η_i and η_o of the inner and outer fluids define the viscosity contrast $\lambda \equiv \eta_i/\eta_o$. This vesicle is subject to the shear flow

$$\mathbf{v}^\infty \equiv \dot{\gamma} y \mathbf{e_x} \tag{4.2}$$

of shear rate $\dot{\gamma}$. Owing to the symmetry of the problem, the vesicle dynamics is determined by what happens in the (xy)-plane. It can be described by only two variables: the inclination angle $\Theta \in]-\pi/2, \pi/2]$ of the long axis relatively to the direction of the external flow, and the phase angle $\tilde{\Phi}$ describing the displacement of a fixed membrane element from its equilibrium position, see fig. 4.1. However, for mathematical simplicity, we will rather use the angle $\Phi \in]-\pi/2, \pi/2]$ which parametrizes the radius $\mathbf{r}$ of the vesicle in the $z = 0$ plane as

$$\mathbf{r}(\Phi) = l_1 \cos\Phi \mathbf{e_1} + l_2 \sin\Phi \mathbf{e_2}. \tag{4.3}$$

This angle Φ is linked to $\tilde{\Phi}$ through the relation

$$\tan\tilde{\Phi} = \frac{l_2}{l_1} \tan\Phi. \tag{4.4}$$

The TT motion is described by assigning the velocity

$$\mathbf{v^m} = \frac{\mathrm{d}\Phi}{\mathrm{d}t} \frac{\partial \mathbf{r}}{\partial \Phi} = \dot{\Phi} \left(-\frac{l_1}{l_2} x_2 \mathbf{e_1} + \frac{l_2}{l_1} x_1 \mathbf{e_2} \right) \tag{4.5}$$

to the membrane. Being proportional to the $\Phi-$derivative of the position vector $\mathbf{r}$, the velocity field $\mathbf{v_m}$ is always tangential to the membrane thus preserving the vesicle shape. However, since all points rotate at the same frequency $\dot{\Phi}$, they do not have the same velocity. Consequently, the area is not locally conserved although the membrane should be incompressible, which constitutes the main approximation of the KS model. This approximation allows us to derive simple equations of motion analytically, which would not be possible with area-conserving fields [46].

Due to the linearity of the Stokes equations, the total moment M acting on a vesicle can be calculated as the sum of three contributions. First, a fixed ellipsoid immersed in a shear flow is subject to the moment

$$M^{\mathrm{S}} = -\frac{\dot{\gamma}}{2} C[l_1^2(1 - \cos 2\Theta) + l_2^2(1 + \cos 2\Theta)], \tag{4.6}$$

with

$$C \equiv \frac{4\eta_o V}{l_1^2 g_1 + l_2^2 g_2}, \quad g_1 \equiv \int_0^\infty (\alpha_1^2 + s)^{-\frac{3}{2}} (\alpha_2^2 + s)^{-\frac{1}{2}} (\alpha_3^2 + s)^{-\frac{1}{2}} \, \mathrm{d}s \tag{4.7}$$

$$g_2 \equiv \int_0^\infty (\alpha_1^2 + s)^{-\frac{1}{2}} (\alpha_2^2 + s)^{-\frac{3}{2}} (\alpha_3^2 + s)^{-\frac{1}{2}} \, \mathrm{d}s \quad . \tag{4.8}$$

Second, an ellipsoid rotating (tumbling) at constant angular velocity $\dot{\Theta}$ in a quiescent fluid experiences the moment

$$M^{\mathrm{TB}} = -C\dot{\Theta}(l_1^2 + l_2^2). \tag{4.9}$$

Third, the TT motion of the vesicle membrane in a quiescent fluid induces the moment

$$M^{\mathrm{TT}} = -C2l_1 l_2 \dot{\Phi}. \tag{4.10}$$

Since we are under Stokes conditions, the total moment $M \equiv M^{\mathrm{S}} + M^{\mathrm{TB}} + M^{\mathrm{TT}}$ must vanish, leading to the equation of motion for the inclination angle

$$\dot{\Theta} = -\frac{\dot{\gamma}}{2}\left(1 - \frac{z_1}{z_0}\cos 2\Theta\right) - \frac{\dot{\Phi}}{z_0} \tag{4.11}$$

with the geometrical quantities

$$z_0 \equiv \frac{1}{2}\left(\frac{l_1}{l_2} + \frac{l_2}{l_1}\right) \qquad\qquad z_1 \equiv \frac{1}{2}\left(\frac{l_1}{l_2} - \frac{l_2}{l_1}\right). \tag{4.12}$$

The evolution of Φ is derived from the energy balance of the system. Due to the no-slip boundary condition, the velocity field is continuous across the membrane. Moreover, dissipation in the membrane is neglected. The rate of work done by the exterior fluid on the vesicle is

$$\dot{W} = 4V\eta_o z_1^2 \dot{\Phi}\left(\dot{\Phi}\left(1 - \frac{2}{z_2}\right) - \frac{\dot{\gamma}}{z_1 z_2}\cos 2\Theta\right). \tag{4.13}$$

Then, as showed in section 2.1.1, Gauss's divergence theorem implies that $\dot{W}$ must be equal to the dissipated energy in the inner fluid

$$d = 4\eta_i V z_1^2 \dot{\Phi}^2, \tag{4.14}$$

with

$$z_2 \equiv g_3'(\alpha_1^2 + \alpha_2^2), \; g_3' \equiv \int_0^\infty (\alpha_1^2 + s)^{-\frac{3}{2}} (\alpha_2^2 + s)^{-\frac{3}{2}} (\alpha_3^2 + s)^{-\frac{1}{2}} \, \mathrm{d}s \tag{4.15}$$

$$\alpha_i \equiv \frac{l_i}{(l_1 l_2 l_3)^{\frac{1}{3}}}. \tag{4.16}$$

Assuming $z_1 \neq 0$, i.e. $l_1 \neq l_2$, meaning that the cross-section is not circular, setting $\dot{W} = d$ leads to

$$\dot{\Phi} = -\frac{\dot{\gamma}}{z_1 z_2 \lambda'} \cos 2\Theta, \tag{4.17}$$

with the reduced viscosity contrast

$$\lambda' \equiv \lambda + \frac{2}{z_2} - 1. \tag{4.18}$$

4.1.2. Skotheim-Secomb extension

Skotheim and Secomb [145] generalized the KS model by adding the periodic energy

$$E \equiv E_0 \sin^2 \Phi \tag{4.19}$$

to the energy balance of the capsule. This energy tends to bring displaced membrane elements back to their initial position, thus modelling the shape memory observed in RBCs [247]. We will therefore call E_0 shape-memory energy. With the energy (4.19), the equations of motion for Θ and Φ become

$$\dot{\Theta} = -\frac{\dot{\gamma}}{2}(1 - B\cos 2\Theta) + \frac{E_0}{4 z_0 z_1^2 \lambda' \eta_o V} \sin 2\Phi, \tag{4.20}$$

$$\dot{\Phi} = -\frac{1}{z_1^2 \lambda'} \left(\dot{\gamma} \frac{z_1}{z_2} \cos 2\Theta + \frac{E_0}{4\eta_o V} \sin 2\Phi \right), \tag{4.21}$$

where

$$B \equiv z_1/z_0 + 2/\lambda' z_0 z_1 z_2. \tag{4.22}$$

In order to construct phase diagrams, we introduce the TB ratio [200]

$$\omega_{\mathrm{TB}} \equiv \frac{\langle \dot{\Theta} \rangle}{\langle \dot{\Theta} \rangle + \langle \dot{\Phi} \rangle} \tag{4.23}$$

where the brackets denote the temporal average in the steady state. This TB ratio plays the role of an order parameter: $\omega_{\mathrm{TB}} = 0$ corresponds to a pure TT motion and $\omega_{\mathrm{TB}} = 1$ to pure TB, intermediate values corresponding to a dynamics in which both TB and TT take place.

4.1.3. Thermal fluctuations

We quantify the influence of thermal fluctuations by adding the stochastic noises $\zeta_\Theta(t)$ and $\zeta_\Phi(t)$ to eqs. (4.20) and (4.21), respectively. They obey

$$\langle \zeta_i(t) \rangle = 0, \quad \langle \zeta_i(t)\zeta_j(t') \rangle = 2D_i\delta_{ij}\delta(t-t'), \tag{4.24}$$

where $\{i,j\} \in \{\Theta, \Phi\}$ and D_Θ and D_Φ are the respective diffusion constants which have to be derived in a consistent manner.

Let us consider again the torque experienced by an ellipsoid rotating at constant angular velocity in a quiescent fluid. The factor multiplying $\dot{\Theta}$ in eq. (4.9) is the inverse mobility of the TB motion. Applying the fluctuation-dissipation theorem leads to the rotational diffusion constant [248]

$$D_\Theta = \frac{k_\mathrm{B}T}{V\eta_o}\frac{l_1^2 g_1 + l_2^2 g_2}{4(l_1^2+l_2^2)}. \tag{4.25}$$

The shape-memory effect was introduced by adding the potential $E_0 \sin^2\Phi$ to the energy balance of the capsule. The fluctuation-dissipation theorem in equilibrium ($\dot{\gamma} = 0$) applied to equation (4.21) then implies

$$D_\Phi = \frac{k_\mathrm{B}T}{V\eta_o}\frac{1}{4z_1^2\lambda'}. \tag{4.26}$$

Note that the divergence of D_Φ for $z_1 \to 0$ can be overlooked, since eq. (4.21) is, as indicated above, only valid for $z_1 \neq 0$ [1]. The diffusion coefficients (4.25) and (4.26) depend on the inverse of the capsule volume V, i.e., the effects of thermal fluctuations become more important the smaller the capsules are. A small outer viscosity η_o also amplifies thermal effects.

Eqs. (4.20) and (4.21) supplemented with the thermal noises ζ_Θ and ζ_Φ form a set of coupled Langevin equations. They can be transformed into a single Fokker-Planck equation for the probability distribution $p(\Theta, \Phi, t)$ by applying the procedure of section 2.2.2. This Fokker-Planck equation reads

$$\partial_t p(\Theta,\Phi,t) = -\partial_\Theta j_\Theta - \partial_\Phi j_\Phi, \tag{4.27}$$

with the currents

$$j_\Theta = -\left[\frac{\dot{\gamma}}{2}(1 - B\cos(2\Theta)) - \frac{E_0}{4\eta_o V z_0 \lambda' z_1^2}\sin(2\Phi) + D_\mathrm{eff}\partial_\Theta - \frac{D_\Phi}{z_0}\partial_\Phi\right] p(\Theta,\Phi,t) \tag{4.28}$$

[1] For a detailed discussion, see [249]

and

$$j_\Phi = -\left[\frac{1}{z_1^2\lambda'}\left(\dot\gamma\frac{z_1}{z_2}\cos(2\Theta)+\frac{E_0}{4\eta_o V}\sin(2\Phi)\right)+D_\Phi\partial_\Phi-\frac{D_\Phi}{z_0}\partial_\Theta\right]p(\Theta,\Phi,t), \quad (4.29)$$

where we defined

$$D_{\text{eff}} \equiv D_\Theta + D_\Phi/z_0^2. \quad (4.30)$$

In the absence of shear flow ($\dot\gamma = 0$), the solution of $\partial_t p(\Theta,\Phi,t) = 0$ is the equilibrium probability distribution

$$p^{\text{eq}}(\Theta,\Phi) = \frac{1}{4\pi^2 I_0\left(\frac{E_0}{2k_\text{B}T}\right)}\exp\left(\frac{E_0}{2k_\text{B}T}(1-2\sin^2\Phi)\right), \quad (4.31)$$

where

$$I_0(x) = \frac{1}{\pi}\int_0^\pi \exp(x\cos\Theta)\,\mathrm{d}\Theta \quad (4.32)$$

is a modified Bessel function of the first kind. The distribution (4.31) does not depend on Θ since no orientation is preferred. For fluid vesicles, we have $E_0 = 0$, leading to a homogeneous distribution for both angles. For elastic ones, the distribution shows two peaks at the angles $\Phi = 0$ and $\Phi = \pi$ due to the energy (4.19). In the following, we will investigate separately these two cases.

All numerical results are obtained for an oblate vesicle with dimensions $l_1 = l_3 = 4\,\mu\text{m}$ and $l_2 = 1.5\,\mu\text{m}$, corresponding approximately to the dimensions of a RBC. The outer viscosity $\eta_o = 1\,\text{mPa s}$ corresponds to that of water at room temperature $T = 293\,\text{K}$. The numerical methods are explained in appendix C.

4.2. Fluid Vesicles

Vesicles with a purely fluid membrane do not exhibit shape memory, i.e. $E_0 = 0$. Then, the Fokker-Planck equation (4.27) does not contain any term depending explicitly on Φ. Therefore, the stationary probability distribution $p^s(\Theta,\Phi)$ depends only on the inclination angle. It is thus enough to analyse the dynamics of Θ to deduce the evolution of the system. In particular, the mean TT frequency can be expressed as

$$\langle\dot\Phi\rangle = -\frac{1}{\lambda' z_1 z_2 B}\left(2\langle\dot\Theta\rangle+\dot\gamma\right). \quad (4.33)$$

by averaging eq. (4.17).

4.2.1. Deterministic dynamics

We first neglect thermal noise. By inserting eq. (4.17) into eq. (4.11), we obtain the time-evolution of the inclination angle

$$\dot{\Theta} = -\frac{\dot{\gamma}}{2}\left(1 - B\cos 2\Theta\right). \tag{4.34}$$

A bifurcation happens at $B = 1$, or equivalently at the critical viscosity contrast

$$\lambda_c \equiv 1 + 2z_0/z_1z_2 \tag{4.35}$$

which depends only on the geometry of the vesicle. For the parameters we chose, $\lambda_c \sim 3.45$.

If $B \geq 1$, i.e. $\lambda \leq \lambda_c$, the vesicle acquires the stationary inclination angle

$$\Theta_{\mathrm{TT}} = \frac{1}{2}\arccos\left(\frac{1}{B}\right), \tag{4.36}$$

which gets smaller when B approaches 1, reaching 0 for $B = 1$. The TB frequency is zero, as is the order parameter $\omega_{\mathrm{TB}} = 0$. The moment coming from the external flow leads to a TT motion of the membrane with constant frequency

$$\dot{\Phi} = -\frac{\dot{\gamma}}{\lambda' z_1 z_2 B}. \tag{4.37}$$

If $B < 1$, the right-hand side of eq. (4.34) is always strictly negative since $\cos 2\Theta \leq 1$. The vesicle therefore rotates monotonously around the z-axis. The steady-state distribution is given by

$$p^s_{\mathrm{KS}}(\Theta, \lambda > \lambda_c) = \frac{\sqrt{1 - B^2}}{2\pi(1 - B\cos 2\Theta)}, \tag{4.38}$$

and the corresponding mean TB frequency is

$$\langle\dot{\Theta}\rangle = -\frac{\dot{\gamma}}{2}\sqrt{1 - B^2}. \tag{4.39}$$

Note that even though the capsule tumbles, the mean TT frequency (4.33) does not vanish. Fig. 4.2 shows the TB ratio and the corresponding TT and TB frequencies as a function of λ for $\dot{\gamma} = 1\,\mathrm{s}^{-1}$, the dashed lines corresponding to the deterministic model. The order parameter $\omega_{\mathrm{TB}} > 0$ is only equal to 1 in the limit of infinite viscosity contrast, in which case the vesicle becomes a rigid ellipsoid.

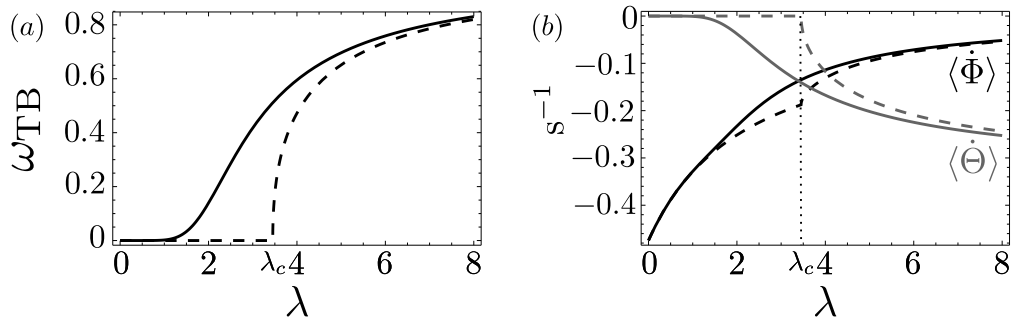

Figure 4.2.: Left: Tumbling ratio ω_{TB} as a function of the viscosity contrast. Right: Corresponding TB frequency $\langle\dot{\Theta}\rangle$ and TT frequency $\langle\dot{\Phi}\rangle$. The shear rate is $\dot{\gamma} = 1\,\mathrm{s}^{-1}$. The full lines correspond to the stochastic model, the dashed ones to the deterministic one, with the parameters defined in Sect. 4.1.3.

4.2.2. Stochastic dynamics

If we include thermal noise, the stationary solution of the Fokker-Planck equation (4.27) becomes

$$p^s(\Theta) = \frac{1}{\mathcal{N}} \int_0^\pi \mathrm{d}\Theta' \exp\left(\frac{\dot{\gamma}}{2D_{\mathrm{eff}}}\left[\Theta' - B\sin\Theta'\cos(\Theta'+2\Theta)\right]\right), \tag{4.40}$$

where

$$\mathcal{N} = 2\pi \int_0^\pi \exp\left(\frac{\dot{\gamma}}{2D_{\mathrm{eff}}}\Theta'\right) I_0\left(\frac{\dot{\gamma}}{2D_{\mathrm{eff}}}B\sin\Theta'\right) \mathrm{d}\Theta' \tag{4.41}$$

is the normalization constant and I_0 the Bessel function (4.32). The stationary probability distribution (4.40) depends on the shear rate $\dot{\gamma}$, which was not the case without thermal fluctuations. The mean TB frequency

$$\langle\dot{\Theta}\rangle = -2\pi\frac{D_{\mathrm{eff}}}{\mathcal{N}}\left(\exp\left[\frac{\dot{\gamma}\pi}{2D_{\mathrm{eff}}}\right] - 1\right) \tag{4.42}$$

is never exactly zero, such that ω_{TB} is always positive. However, as can be seen from the full line in fig. 4.2(a), it may become extremely small. We can thus set an arbitrary cut-off under which a TT regime can be effectively identified. Fig. 4.2 also shows that thermal fluctuations are most important around the critical viscosity contrast λ_c, that is close to the TT-TB bifurcation. Far from it, the deterministic and stochastic results are similar.

The contour plot of fig. 4.3, which represents ω_{TB} as a function of λ and $\dot{\gamma}$, can therefore be seen as a dynamical phase diagram. Pure TT occurs approximately in the black region ($\omega_{\mathrm{TB}} < 0.1$), and TB in the grey regions. Contrary to the deterministic case, in which the TT-TB transition occurs at λ_c (white dashed line),

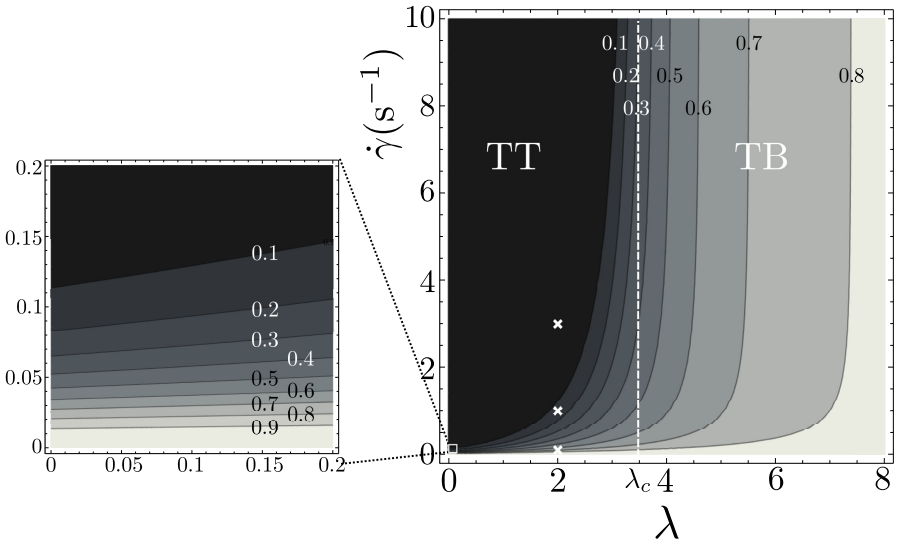

Figure 4.3.: Phase diagram for the KS model with thermal noise as a function of the shear rate $\dot{\gamma}$ and the viscosity contrast λ. The dashed line corresponds to the deterministic critical viscosity contrast (4.35). An enlargement of the bottom left corner is also shown. The white crosses correspond to fig. 4.5.

with thermal noise this transition depends also on the shear rate $\dot{\gamma}$. In the limit of high shear rates, fluctuations are less important. The critical viscosity contrast is then close to the deterministic one, although a little bit smaller due to stochastic rotations happening at low TT inclination angles. For low but still positive shear rates, the critical viscosity contrast goes to 0. As the enlargement in fig. 4.3 shows, a TB motion is always present for $\dot{\gamma}$ lower than approximately $0.1\,\mathrm{s}^{-1}$, which is a new feature with respect to the deterministic phase diagram derived in Ref. [151]. This TB motion happens because, at low shear rates, thermal fluctuations become dominant.

In order to illustrate this shear-induced transition, we plot the time-evolution of Θ and Φ for $\lambda = 2$ and three different values of $\dot{\gamma}$ in fig. 4.4 (corresponding to the crosses in fig. 4.3). For $\dot{\gamma} = 3\,\mathrm{s}^{-1}$, the TT angle Φ decreases continuously while the orientation angle Θ fluctuates around Θ_{TT}. The dynamics is the deterministic one and thermal fluctuations have a minor role ($\omega_{\mathrm{TB}} = 0.0052$). For $\dot{\gamma} = 1\,\mathrm{s}^{-1}$, TT still takes place but there are some intermittent TB rotations caused by thermal noise ($\omega_{\mathrm{TB}} = 0.13$). If we decrease the shear rate further to $\dot{\gamma} = 0.1\,\mathrm{s}^{-1}$, thermal fluctuations dominate and both angles undergo a biased random walk, which explains the high value of $\omega_{\mathrm{TB}} = 0.68$. We can therefore distinguish two kinds of TB motion. For $\lambda > \lambda_c$, the inclination angle decreases monotonously (up to thermal fluctuations) because the deterministic system is unstable. For $\lambda \leq \lambda_c$, thermal

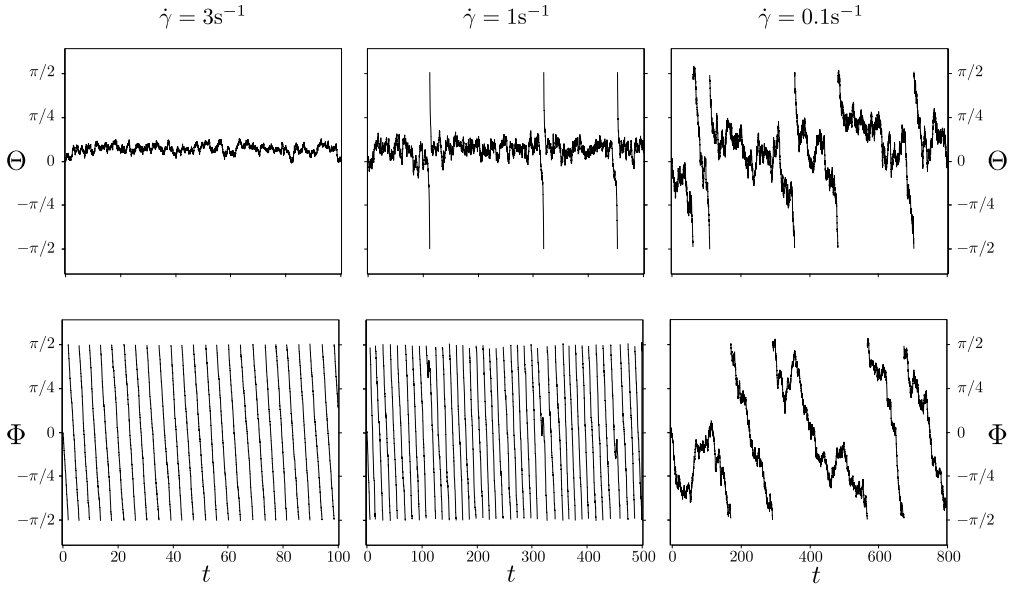

Figure 4.4.: Time-evolution of Θ and Φ for $\lambda = 2$ and $\dot\gamma = 3\,\mathrm{s}^{-1}$, $1\,\mathrm{s}^{-1}$, and $0.1\,\mathrm{s}^{-1}$. The jumps in the plot are because both Θ and Φ are defined between $-\pi/2$ and $\pi/2$.

fluctuations induce intermittent TB rotations, making the TB ratio positive thus creating an effective TB regime.

The probability distributions $p^s(\Theta)$ corresponding to the trajectories of fig. 4.4 are shown in fig. 4.5 (a). For high shear rates, the distribution is symmetrically centered around the deterministic TT angle Θ_{TT} (vertical line), whereas for lower ones, the distribution becomes flatter and asymmetric. The mean inclination angle $\langle\Theta\rangle$ as a function of λ is also influenced by thermal noise - a fact already seen in [48] - and an exponential tail appears instead of sharp transition, as illustrated by fig. 4.5 (b). Such a tail is similar to the one observed in a simulation including thermal noise [64]. A similar slow decay of the mean inclination angle has also been recently measured in experiments [137], but it seems that it can be reproduced in deterministic simulations as well [98].

4.3. Elastic Vesicles

We now consider vesicles with shape-memory energy, i.e. $E_0 > 0$. As opposed to the previous case, the currents (4.28) and (4.29) now depend on both Θ and Φ. We have to resort to numerical methods, described in appendix C, to solve eq. (4.27) in the steady state.

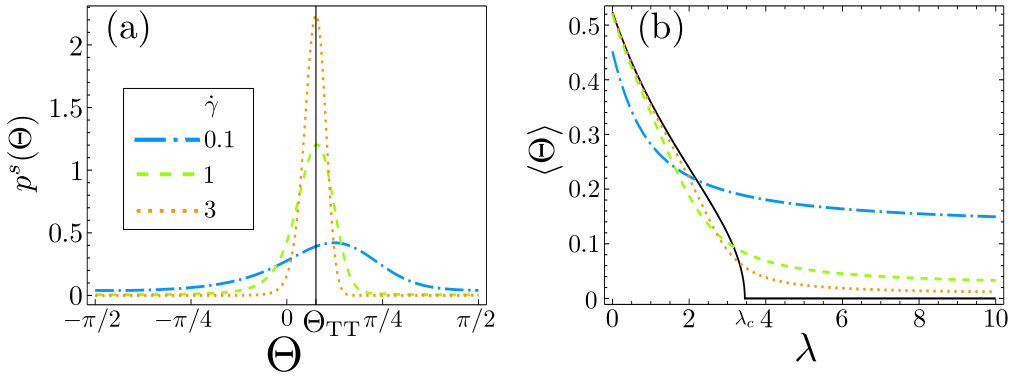

Figure 4.5.: (a) Probability distribution of the orientation angle Θ at $\lambda = 2$ and different shear rates. (b) Mean inclination angle $\langle\Theta\rangle$ as a function of the viscosity contrast. The solid black lines represent the deterministic model.

4.3.1. Deterministic dynamics

By non-dimensionalizing eqs. (4.20) and (4.21), it can be shown that, for fixed ratios l_2/l_1 and l_3/l_1 (here equal to 3/8 and 1, respectively), the phase diagram of the system depends only on two parameters [145]: the viscosity contrast λ and the dimensionless shape-memory energy

$$U_e \equiv \frac{E_0 z_2}{4V\eta_o\dot{\gamma}z_1}. \tag{4.43}$$

The phase diagram plotted in fig. 4.6(a) has been obtained by taking the time-average of ω_{TB} over steady-state trajectories of 500 s. It exhibits three types of motion, which have all been observed experimentally [144, 146]. The TT regime of the KS model becomes the swinging (SW) regime ($\omega_{TB} = 0$, black region): the orientation angle oscillates around Θ_{TT} while the membrane tank-treads. As for fluid vesicles, the TB regime consists in a monotonous rigid-body-like rotation. However, contrary to fluid vesicles, there is no net TT rotation but rather an oscillation of the phase angle. Therefore, $\langle\dot{\Phi}\rangle = 0$ and $\omega_{TB} = 1$ in the white region. Both TT and TB motions are periodic motions, meaning that they converge to a limit cycle starting from any initial condition, see fig. 4.6(b).

For $0 < \omega_{TB} < 1$, elastic vesicles are in the intermittent regime (INT, colored region). Note that for the same value of the order parameter, the motion of a fluid vesicle ($E_0 = 0$) would be classified as TB. The difference is that the decrease of the orientation angle in INT is not monotonous, the vesicle being sometimes pushed back by the elastic reaction of the membrane. In this regime, TB and TT motions alternate either in periodic (fig. 4.6(c)) or aperiodic fashion (fig. 4.6(d)) depending on the value of U_e [250]. The existence of the aperiodic motion is only

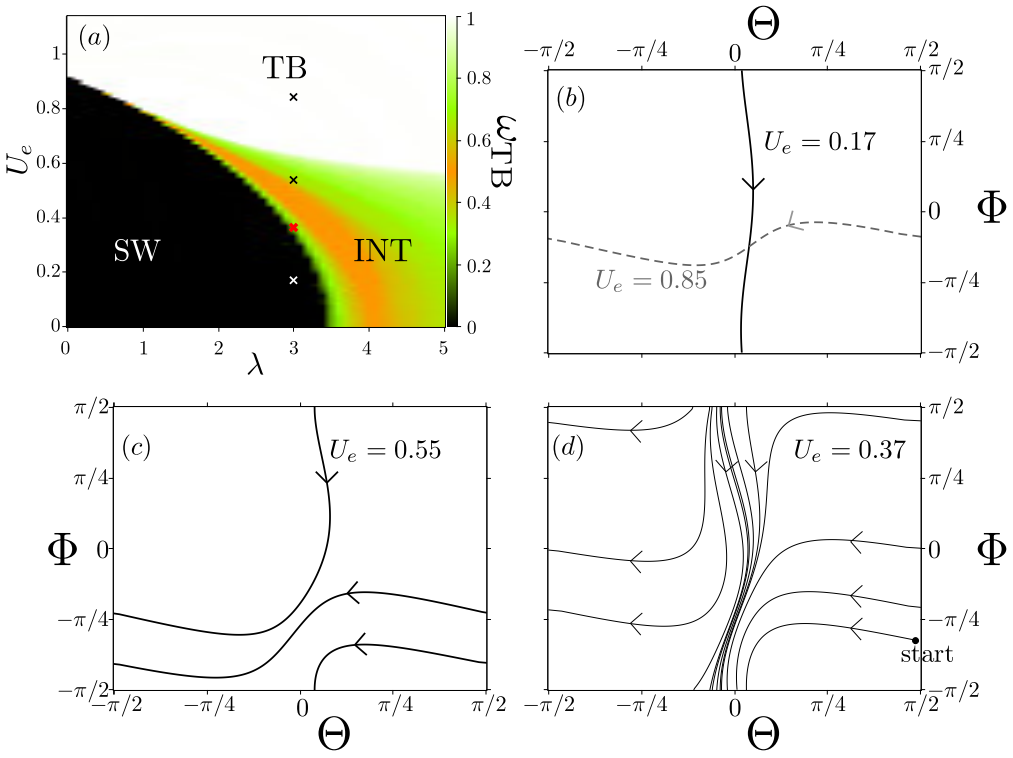

Figure 4.6.: (a) Phase diagram of the Skotheim-Secomb model as a function of the viscosity contrast λ and the dimensionless shape-memory energy U_e. (b) Typical SW ($U_e = 0.17$) and TB ($U_e = 0.85$) limit cycles in the (Θ, Φ) plane. (c) Periodic intermittent trajectory. (d) Aperiodic intermittent trajectory of length 150 s starting at the marked point. Plots (b)-(d) correspond to $\lambda = 3$ (crosses in (a)).

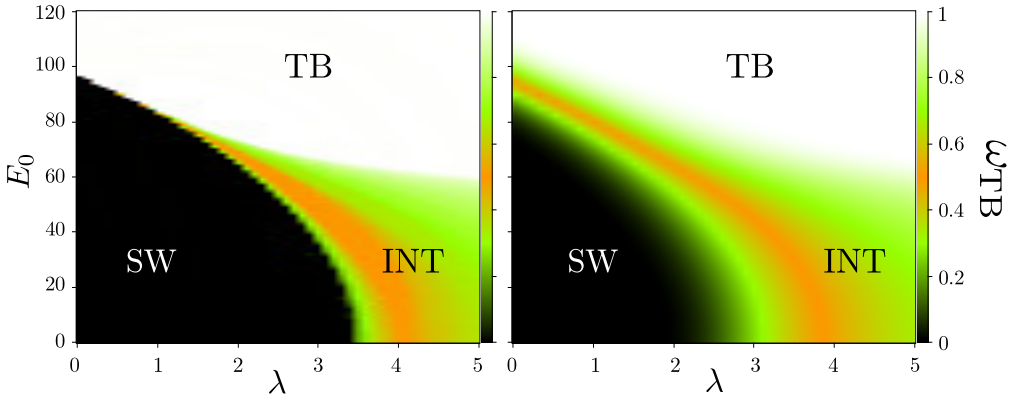

Figure 4.7.: Phase diagrams of the dynamics of capsules as a function of λ and E_0 (in units of k_BT) for $\dot{\gamma} = 1\,s^{-1}$ in the deterministic (left) and stochastic (right) case.

possible because the phase-space has the topology of a torus [200, 251]. Therefore, the trajectory in the (Θ, Φ)-space is either a limit-cycle or an aperiodic trajectory which passes infinitesimally close to each point and does not intersect itself.

4.3.2. Stochastic dynamics

If we now take thermal fluctuations into account, the dynamics of the system depends not only on λ and U_e but also on the temperature T. For a clearer quantitative discussion, we let $T = 293\,K$ and go back to dimensional variables.

The phase diagrams of fig. 4.7 represent the TB ratio ω_{TB} as a function of the viscosity contrast λ and the shape-memory energy E_0 for $\dot{\gamma} = 1\,s^{-1}$. As for vesicles, ω_{TB} is never exactly 0 or 1 with thermal noise, but the values are extremely close in the black and white regions such that we can still effectively identify the SW and TB regimes, respectively. The overall structure of the phase diagram is not changed, but the region for which intermittent dynamics takes place is much wider in the presence of thermal noise. In particular, the intermittent region for $\lambda \leq 1$ is then large while it is almost not distinguishable in the deterministic case.

To investigate the noise-induced intermittent regime, we take a closer look at ω_{TB} as a function of E_0 for $\lambda = 0$ as plotted in fig. 4.8(a). In the deterministic case (black line), the transition is very sharp. We determine numerically that it happens between $E_0 = 96$ (in units of k_BT), where the vesicle is in TT, and $E_0 = 97$, where pure TB is observed. Thermal fluctuations make the transition smoother. We observe intermittent motion in a region of approximately $40k_BT$ around the deterministic transition energy. Figs. 4.8(b)-(d) show the stationary probability distribution at different values of the shape-memory energy. For $E_0 = 60$, the

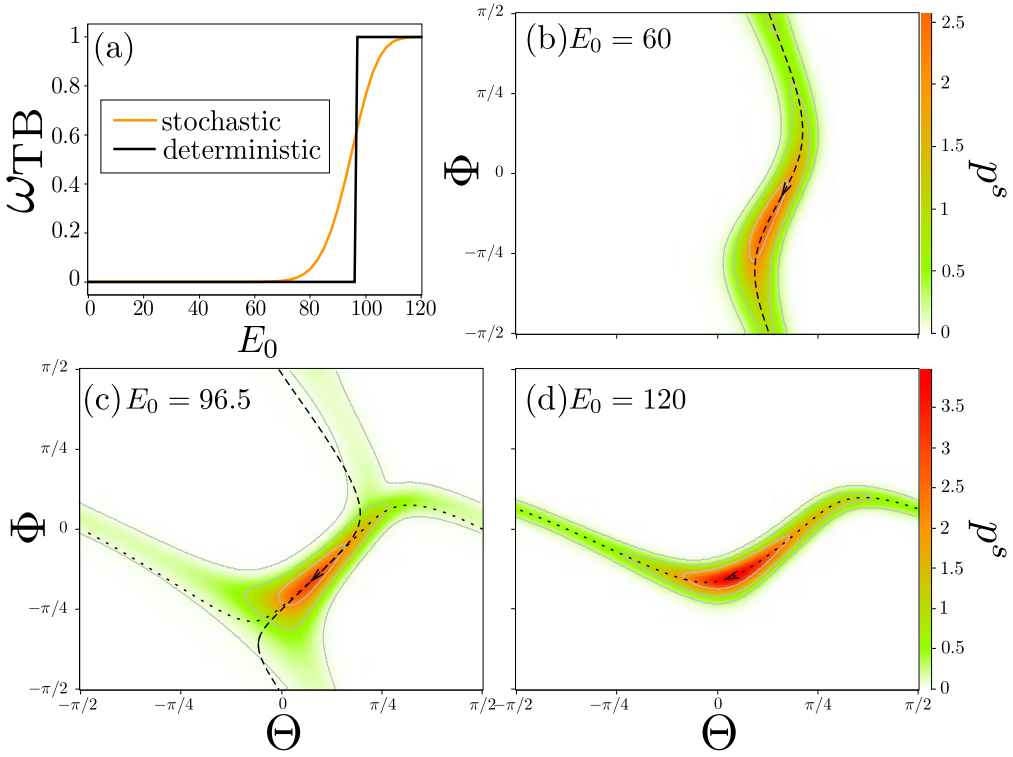

Figure 4.8.: (a) ω_{TB} as a function of the shape-memory energy E_0. (b)-(d) Stationary probability distribution $p^s(\Theta, \Phi)$ three different values of E_0. The other parameters are $\lambda = 0$ and $\dot{\gamma} = 1\,\mathrm{s}^{-1}$. The dashed and dotted lines correspond to deterministic trajectories.

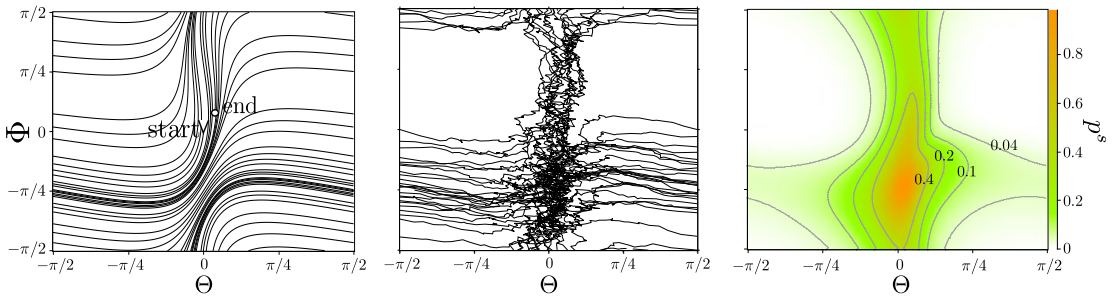

Figure 4.9.: Intermittent behaviour with $\dot{\gamma} = 1\,\mathrm{s}^{-1}$, $\lambda = 4$ and $E_0 = 40 k_\mathrm{B} T$. Left: Deterministic trajectory of length 500 s. Centre: Same trajectory with thermal noise. Right: Steady-state probability distribution with thermal noise.

vesicle is in the TT regime and the probability distribution follows exactly the deterministic trajectory (dashed line), but the mean amplitude of the oscillations in Θ is approximately two times larger. Similarly, for $E_0 = 120$, the vesicle is in TB and the most probable path is the deterministic one (dotted line) with larger oscillations of Φ. At the transition ($E_0 = 96.5$), however, we observe a thermal mixing of TT and TB regimes. The vesicle exhibits both motions with a slight offset with respect to the deterministic paths at $E_0 = 96$ (dashed line) and $E_0 = 97$ (dotted line). Thus thermal fluctuations create an effective intermittent regime by mixing TT and TB when these two motions are energetically close.

The intermittent regime predicted by the deterministic model still exists but its properties are altered by the presence of thermal noise, as shown in fig. 4.9. The left panel shows a deterministic trajectory for $\dot{\gamma} = 1\,\mathrm{s}^{-1}$, $\lambda = 4$, and $E_0 = 40 k_\mathrm{B} T$, starting at $(0, 0)$ and ending at the marked point. This trajectory is aperiodic and consists of complete TB rotations (horizontal curves) interrupted by incomplete TT motions since there cannot be any intersection. The middle panel shows a stochastic trajectory with the same parameters. Complete TB rotations as well as complete TT rotations may occur since an intersecting trajectory is not forbidden for a stochastic motion. This properties are also visible on the right panel, which shows the stationary probability distribution $p^s(\Theta, \Phi)$ with thermal noise. The vesicle spends most time TT at low inclination angles but full TB rotations occur regularly. In the same time, points in the white areas on the top right and top left are almost excluded, which was not the case in the deterministic trajectory.

4.4. Conclusion

Under realistic conditions, the effect of thermal fluctuations on the dynamics of vesicles with or without shape memory should be observable. For fluid vesicles,

the important prediction concerns the TB motion at very low shear rates. This phenomenon has not yet been investigated experimentally, but the conditions for such experiments are already met [114, 139]. Undeformable elastic vesicles are a good model system for RBCs, but these have been studied at too high viscosities to show thermal effects [144, 195]. Moreover, their shape-memory energy is of the order of $1000 - 2000 k_{\mathrm{B}}T$ [145], which also makes thermal effects more subtle. Nevertheless, it still remains conceivable that the noise-induced intermittent regime could be observed with synthetic capsules.

A much more detailed analysis of the system can be found in the Master's thesis of J. G. Müller [249]. There, it is shown that, even for RBCs, thermal fluctuations influence the estimation of elastic parameters such as membrane shear elasticity and viscosity. Moreover, the analysis has been extended to general linear flow of the form (3.1), for which a fourth regime exists in which both angles Θ and Φ remain constant. The results in [249] can be directly compared to future experiments.

5. Trembling vesicles in linear flow

For fluid vesicles, the model presented in chapter 4 is only valid at very low flow rates, as explained in section 3.2.2. Here, we present a model for deformable quasi-spherical vesicles in general linear flow of the form (3.1). The analysis presented in this chapter is an extension of the model for quasi-spherical vesicles of [41] in which we expand the bending energy to next order. We consider not only harmonics directly excited by the flow but also higher-order ones. We show that our model correctly predicts the trembling motion observed in experiments [122, 137, 139], which is due to the amplification of thermal noise during compression phases. The most important results of this chapter have already been published [58].

5.1. Model

We consider a vesicle with effective radius R_0 and excess area Δ defined by eqs. (2.30) and (2.31). Both quantities are fixed since the volume and the area are constant. The inner and outer fluids are the same such that the viscosity contrast λ is equal to 1. We assume that the vesicle is quasi-spherical, i. e., its excess area Δ is small. We then expand the radius

$$\mathbf{R}(\theta,\phi) \equiv R_0\left(1+u(\theta,\phi)\right)\mathbf{e_r} \equiv R_0\left(1+\sum_{l=0}^{\infty}\sum_{m=-l}^{l} u_{lm}\mathcal{Y}_{lm}(\theta,\phi)\right)\mathbf{e_r} \tag{5.1}$$

in the basis of spherical harmonics $\mathcal{Y}_{lm}$, see fig. 5.1 and appendix A. The expansion coefficients obey $u_{l,-m} = (-1)^m u_{lm}^*$. This vesicle is subject to a planar linear flow of the form (3.1) with vorticity ω and strain rate s, see fig. 5.2. We first express the vesicle properties as a function of the expansion coefficients u_{lm}, for which we then derive equations of motion.

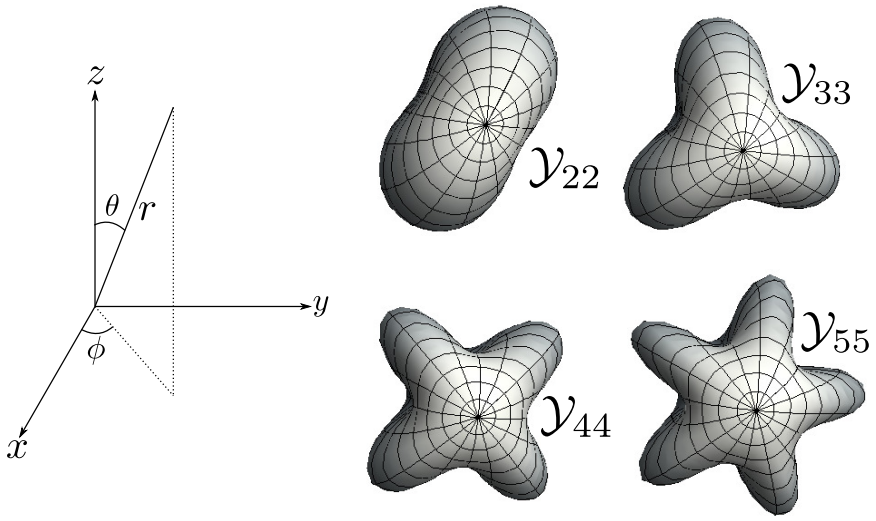

Figure 5.1.: Left: Coordinate system. Right: Examples of spherical harmonics. The represented function is $r(\theta, \phi) = 1 + \mathrm{Re}(\mathcal{Y}_{ll}(\theta, \phi))$ for $l = 2, 3, 4, 5$. The node corresponds to $\theta = 0$.

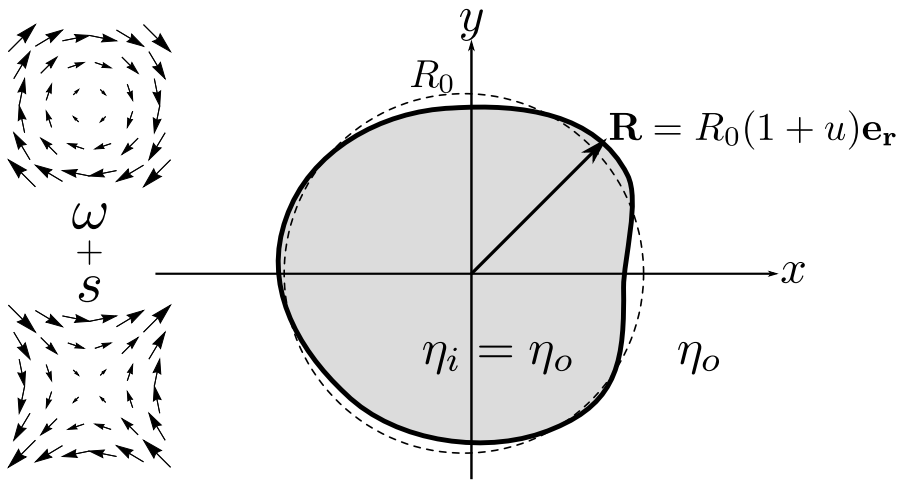

Figure 5.2.: Cross-section in the (xy)-plane ($\theta = \pi/2$) of a quasi-spherical vesicle in general linear flow with strain rate s and vorticity ω. The dashed line represents the virtual sphere of radius R_0.

5.1.1. Vesicle properties

Using the results from [252] (see details in appendix B), the expansion of the volume to third-order in u is given by

$$V = R_0^3 \left[\frac{4\pi}{3} \left(1 + \frac{u_{00}}{\sqrt{4\pi}} \right)^3 + \left(1 + \frac{u_{00}}{3\sqrt{4\pi}} \right) \sum_{l\geq 1,m} |u_{lm}|^2 + \sum_{l_i \geq 1, m_i} \frac{1}{3} C_{123}^{lm} u_{l_1 m_1} u_{l_2 m_2} u_{l_3 m_3} \right] + O(u^4) \tag{5.2}$$

where the coupling term C_{123}^{lm} is given by eq. (A.11). Since the volume $V = (4\pi/3)R_0^3$ remains constant, the lowest mode u_{00} can be expressed as function as the higher-order modes as

$$u_{00} = -\frac{1}{\sqrt{4\pi}} \left[\sum_{l\geq 1} |u_{lm}|^2 + \sum_{l_i \geq 1} \frac{1}{3} C_{123}^{lm} u_{l_1 m_1} u_{l_2 m_2} u_{l_3 m_3} \right] + O(u^4). \tag{5.3}$$

The expansion to third-order in u of the area is given by

$$A = R_0^2 \left[4\pi \left(1 + \frac{u_{00}}{\sqrt{4\pi}} \right)^2 + \sum_{l\geq 1} \left(1 + \frac{l(l+1)}{2} \right) |u_{lm}|^2 \right] + O(u^4). \tag{5.4}$$

Inserting the expression (5.3), we find that the excess area $\Delta = A/R_0^2 - 4\pi$ is equal to

$$\Delta = \sum_{l\geq 1} \frac{(l-1)(l+2)}{2} |u_{lm}|^2 - \frac{2}{3} \sum_{l_i \geq 1} C_{123}^{lm} u_{l_1 m_1} u_{l_2 m_2} u_{l_3 m_3} + O(u^4) \equiv \Delta^{(3)} + O(u^4). \tag{5.5}$$

The membrane forces are given by eq. (2.41). The surface tension, which enforces the local and global incompressibility, can be expanded in spherical harmonics as

$$\sigma \equiv \sum_{l,m} \sigma_{lm} \mathcal{Y}_{lm}. \tag{5.6}$$

To calculate the bending energy (2.41), we will only consider the homogeneous part σ_{00} which is responsible for the global area conservation. The coefficients $\sigma_{l\geq 1,m}$ will ensure local incompressibility and are treated separately [41]. The bending energy (2.41) can then be expressed to third order in u as [253]

$$\mathcal{H}_\kappa = 2\pi\kappa(4 + \sigma_{00}) + \frac{\kappa}{2} \sum_{l\geq 1,m} (l-1)(l+2)[l(l+1) + \sigma_{00}]|u_{lm}|^2 + \frac{\kappa}{2} \sum_{l_i \geq 1, m} \left[(l_1 - 1)l_1(l_1+1)(l_1+2) - \frac{2}{3}\sigma_{00} \right] C_{123}^{lm} u_{l_1 m_1} u_{l_2 m_2} u_{l_3 m_3}. \tag{5.7}$$

5.1.2. Equations of motion

To derive equations of motions for the coefficients u_{lm}, we adapt the solution of [41], where the detailed calculations can be found. There, the vesicle is immersed in a shear flow with $\omega = s \equiv \dot{\gamma}/2$. Lamb's solution from section 2.1.2 is used to match the inner and outer flows and stresses not at the membrane, but rather at the virtual sphere of radius R_0. The equation of motion

$$\dot{u}_{lm} = i\frac{\dot{\gamma}}{2} m u_{lm} - \mu_l (l-1)(l+2)[l(l+1) + \sigma_{00}]u_{lm} - ic\frac{\dot{\gamma}}{2}\varepsilon_{lm} + \zeta_{lm}(t) \tag{5.8}$$

is obtained, where the dot stands for the time derivative and $c \equiv 24\sqrt{2\pi/15}/11$, $\varepsilon_{lm} \equiv \pm\delta_{l,2}\delta_{m,\pm 2}$, $\mu_l \equiv \Gamma_l \kappa/(\eta_o R_0^3)$, and $\Gamma_l \equiv l(l+1)/(4l^3+6l^2-1)$. The complex thermal noise $\zeta_{lm}(t)$ is white and its correlations

$$\langle \zeta_{lm}(t)\zeta^*_{l'm'}(t')\rangle = 2\mu_l k_B T(-1)^m \delta_{l,l'}\delta_{m,-m'}\delta(t-t') \tag{5.9}$$

are given by the fluctuation-dissipation theorem in equilibrium. The condition of local incompressibility is already taken into account in eq. (5.8). The homogeneous surface tension σ_{00} is determined by the condition $\partial_t \Delta = 0$ at every time which couples all modes together. However, in the absence of thermal noise, only u_{22} does not decay to 0 since it is directly excited by the flow. Moreover, eq. (5.7) predicts a TT motion for all shear rates $\dot{\gamma}$ since $\lambda = 1$, see section 3.2.1.

In order to describe couplings between modes and to observe TB and TR motions while keeping the viscosity contrast λ equal to 1, we generalise the model to linear flows of the form (3.1). As a result, $\dot{\gamma}/2$ is replaced by the vorticity ω in the first term and by the elongation rate s in the third term of the right-hand side of eq. (5.8). The second term corresponds to the derivative of the second-order expansion of the bending energy (5.7) with respect to u^*_{lm}. In our model, we take the bending energy up to third order in u. As pointed out in [151], these terms are necessary for the deterministic dynamics to be independent of the initial conditions. Of course, the sensitivity to initial conditions disappears with thermal noise. However, the couplings will still be very important in the following. The noise term remains the same. We do not include the hydrodynamic corrections discussed in Refs. [60, 150], even though they become relevant for strong enough flows as shown in chapter 6. The new equations of motion are then

$$\dot{u}_{lm} = im\omega u_{lm} - \mu_l \frac{\partial \mathcal{H}_\kappa}{\partial u^*_{lm}} - ics\varepsilon_{lm} + \zeta_{lm}(t). \tag{5.10}$$

The first term on the right-hand side of eq. (5.10) is a norm-preserving rotation of all harmonics u_{lm} due to the vorticity ω of the external flow. The second term depending on $\mathcal{H}_\kappa$ contains the non-linear coupling between the modes. In

particular, terms with even l and m are coupled together through the third order of the bending energy (5.7) and the excess area (5.4). The third term corresponds to the elongation part of the flow which only acts on the prolate ellipsoidal harmonics $\mathcal{Y}_{2,\pm 2}$. For this reason, we can distinguish between different regimes by looking at the evolution of the orientation angle ϕ_{22} defined by

$$u_{22} \equiv |u_{22}| \mathrm{e}^{-2i\phi_{22}}. \tag{5.11}$$

ϕ_{22} corresponds to good approximation to the inclination angle of the long axis of the vesicle in the flow plane, since u_{22} is most of the time the largest mode. The equation of motion for ϕ_{22} follows from (5.10) as

$$\dot{\phi}_{22} = -\omega \left(1 - \frac{c \cos(2\phi_{22})}{2|u_{22}|} \frac{s}{\omega} \right) + \frac{\zeta_\phi(t)}{2\sqrt{2}|u_{22}|} \tag{5.12}$$

where ζ_ϕ is a Gaussian white noise having the correlations (5.9)[1].

In the following, we solve the set of equations (5.10) numerically. We neglect the modes with $l = 1$ since they correspond to translations and a therefore not relevant to our problem. We keep all harmonics between $l = 2$ and $l = 5$ (corresponding to eighteen coupled equations) in order to analyse the difference between even and odd modes. In the numeric scheme, we replace the homogeneous surface tension σ_{00}, which strictly enforces the constraint of constant area, by the force

$$f^A_{lm} \equiv -\mu_l \frac{\partial U_A}{\partial u^*_{lm}} \tag{5.13}$$

coming from the energy

$$U_A \equiv \frac{K_A}{2} (\Delta^{(3)} - \Delta)^2, \tag{5.14}$$

where K_A is the spring constant and $\Delta^{(3)}$ is the third-order expansion of the excess area Δ from eq. (5.5). For $K_A \to \infty$, we recover the same dynamics as with the rigid constraint σ_{00}. The soft constraint, however, is much easier to treat numerically since it avoids the intricacies of multiplicative noise [254]. Furthermore, in order to compare our results to other models and to experiments, we will use the quantities

$$S \equiv \frac{14\pi}{3\sqrt{3}} \frac{\eta_o R_0^3}{\kappa \Delta} s \qquad \Lambda \equiv \frac{55}{24} \sqrt{\frac{3\Delta}{10\pi}} \frac{\omega}{s}. \tag{5.15}$$

already defined in eq. (3.4) (here with $\lambda = 1$). We set $T = 293\,\mathrm{K}$, $R_0 = 15\,\mu\mathrm{m}$, $\kappa = 25 k_B T$ and $\eta_o = 1\,\mathrm{mPa\,s}$, which correspond to typical experimental values [139]. The comparison to the deterministic case is done by ignoring the thermal noise in our equations. The details of the algorithm are presented in appendix C.

[1] Transforming the noise in eq. (5.10) from Cartesian to polar coordinates is a subtle issue, see section 4.4.5 of Ref. [32].

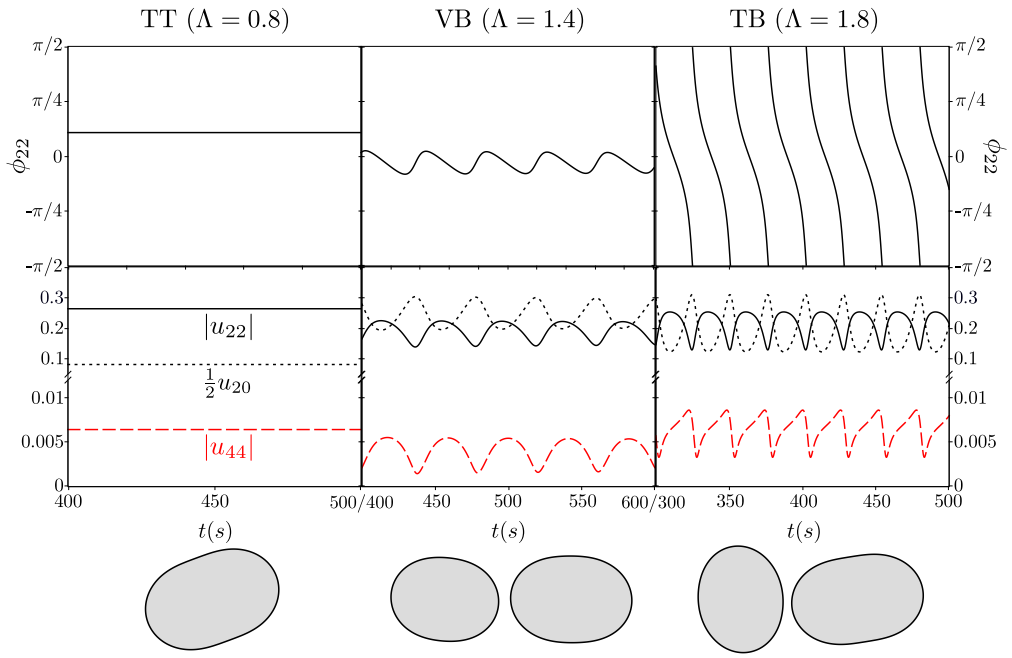

Figure 5.3.: Top: Temporal evolution of the inclination angle ϕ_{22} for $\Delta = 0.3$, $S = 30$ and $\Lambda = 0.8$, 1.4, and 1.8 (corresponding to $s = 0.032\,\mathrm{s}^{-1}$, and $\omega = 0.066\,\mathrm{s}^{-1}$, $0.11\,\mathrm{s}^{-1}$, and $0.15\,\mathrm{s}^{-1}$). Middle: Corresponding evolution of $|u_{22}|$ (black line), $\frac{1}{2}u_{20}$ (black dots), and $|u_{44}|$ (red dashes). Note the axis break. Bottom: Corresponding snapshots. For VB and TB, the first and second shapes correspond to minimal and maximal $|u_{22}|$, respectively.

5.2. Regimes of motion

For small values of the ratio ω/s, the deterministic part of eq. (5.12) may have a fixed point, whereas for larger ratios, the right-hand side is always negative. These two cases correspond roughly to the TT and TB motions, respectively. Of course, since $|u_{22}|$ might vary as well, more complex dynamics take place. The most characteristic harmonics in the flow plane $\theta = \pi/2$ are thus $\mathcal{Y}_{20}$, which is a sphere, and $\mathcal{Y}_{ll}$ ($l = 2, .., 5$), which correspond to the number of lobes[2] of the vesicle shape, i.e. the characteristic wavelength of shape deformations, see fig. 5.1. We will first present the deterministic results for the dynamics of ϕ_{22}, and u_{20} and u_{ll}, and then show that thermal fluctuations create a new trembling regime.

[2]This is true for $\mathcal{Y}_{44}$ and $\mathcal{Y}_{55}$, but only approximate for $\mathcal{Y}_{22}$ (resp. $\mathcal{Y}_{33}$) since $\mathcal{Y}_{42}$ (resp. $\mathcal{Y}_{53}$) also corresponds to elliptical (resp. triangular) deformations in the flow plane. However, $|u_{42}|$ (resp. $|u_{53}|$) is most of the time much lower than $|u_{22}|$ (resp. ($|u_{33}|$).

5.2.1. Deterministic dynamics

In the deterministic case, only the harmonics with both l and m even survive while those with odd l or m decay very fast to zero. Three types of motion are observed, as shown in fig. 5.3. For low vorticity-to-elongation ratios ω/s, i.e. small Λ, the TT regime is observed in which the orientation angle ϕ_{22} remains strictly constant. The vorticity of the flow produces a rotation of the membrane, while the elongation part stretches the membrane into an ellipsoidal shape for which $\mathcal{Y}_{22}$ is the dominant harmonic.

At intermediate Λ, the VB regime takes place. There, ϕ_{22} oscillates around a slightly negative value. The dynamics of $|u_{22}|$ is perfectly correlated with this oscillation albeit with a short lag behind. When the orientation angle is positive, the vesicle is stretched and the second mode $|u_{22}|$ grows. When it is large enough, the right-hand side of eq. (5.12) becomes negative, triggering a decrease of the inclination angle ϕ_{22}, which becomes negative. At negative inclination angles, the external flow compresses the tips of the ellipsoid. The vesicle becomes rounder, corresponding to a growth of u_{20} and a decrease of $|u_{22}|$. This decrease happens until the right-hand side of eq. (5.12) becomes positive again and the ϕ_{22} grows. This interplay between u_{20} and $|u_{22}|$ characterises the VB motion. $|u_{44}|$ is perfectly synchronized with $|u_{22}|$, exhibiting minima and maxima at the same times.

For larger Λ, the vesicle is in the TB regime characterised by full rotations. The interplay between u_{20} and $|u_{22}|$ is still present since the vesicle passes through negative inclination angles, i.e. compression phases. However, the dynamics of $|u_{44}|$ is different than in VB. The growth of $|u_{44}|$ shows two distinct slopes. The first one is due to the deterministic coupling with the second mode already observed in the VB motion. The second phase of the growth happens at large negative inclination angles. There, the surface tension σ_{00} becomes lower than -20 and the second term on the right-hand side of eq. (5.8) becomes then positive, leading to a growth of $|u_{44}|$. This phenomenon will be analysed in more details in chapter 6.

The snapshots of fig. 5.3 show that the deformations in the deterministic model are weak and axisymmetric. Higher-order deformations like $|u_{44}|$ are always much lower than second-order ones. Moreover, both VB and TB are strictly periodic motions. These observations are in strong contrast with the experimental dynamics [122, 137, 139], which show irregular oscillations and strong asymmetric shape deformations. We show in the next section that this discrepancy is resolved by taking thermal fluctuations into account.

5.2.2. Stochastic dynamics

If we include thermal fluctuations, all $|u_{lm}|$ have a strictly positive mean value and contribute to the dynamics. Figure 5.4 shows the temporal evolution of the

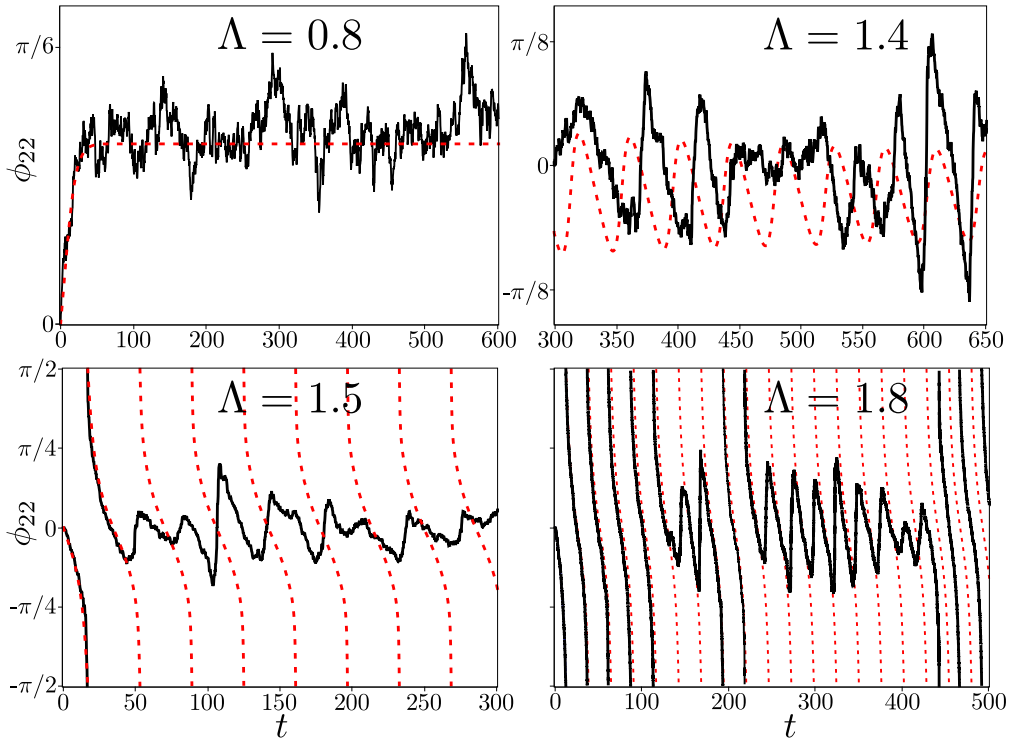

Figure 5.4.: Temporal evolution of the inclination angle ϕ_{22} (solid black curves) for $\Delta = 0.3$, $S = 30$ and $\Lambda = 0.8$, 1.4, 1.5, and 1.8 (corresponding to $s = 0.032\,\mathrm{s}^{-1}$ and $\omega = 0.066\,\mathrm{s}^{-1}$, $0.11\,\mathrm{s}^{-1}$, $0.12\,\mathrm{s}^{-1}$ and $0.15\,\mathrm{s}^{-1}$). The red dashed curves are the corresponding deterministic trajectories.

inclination angle ϕ_{22} for $S = 30$ ($s = 0.032\,\mathrm{s}^{-1}$) and four different values of Λ. For small values of the vorticity ($\Lambda = 0.8$), the vesicle is in the TT regime, in which its orientation fluctuates around the deterministic value but remains positive. If we increase the vorticity of the flow, we observe the TR motion ($\Lambda = 1.4$ and $\Lambda = 1.5$), for which the oscillation angle irregularly oscillates around 0. Without thermal noise, the model predicts a periodic VB motion for $\Lambda = 1.4$ but TB already for $\Lambda = 1.5$, whereas the stochastic motion is still TR. This observation is in agreement with experimental results, which find that TR happens for a much broader range of parameters than predicted by deterministic models [117, 136]. For $\Lambda = 1.8$, we see a mixture between TR and TB, with bursts of TR happening between the TB cycles. Thermal fluctuations mix both regimes at the TR-TB transition, a similar effect to what happens for undeformable elastic vesicles at the SW-TB transition investigated in section 4.3.2.

The difference between stochastic and deterministic models becomes even clearer if we looks at the vesicle shape in the TR regime. Figure 5.5 shows the time

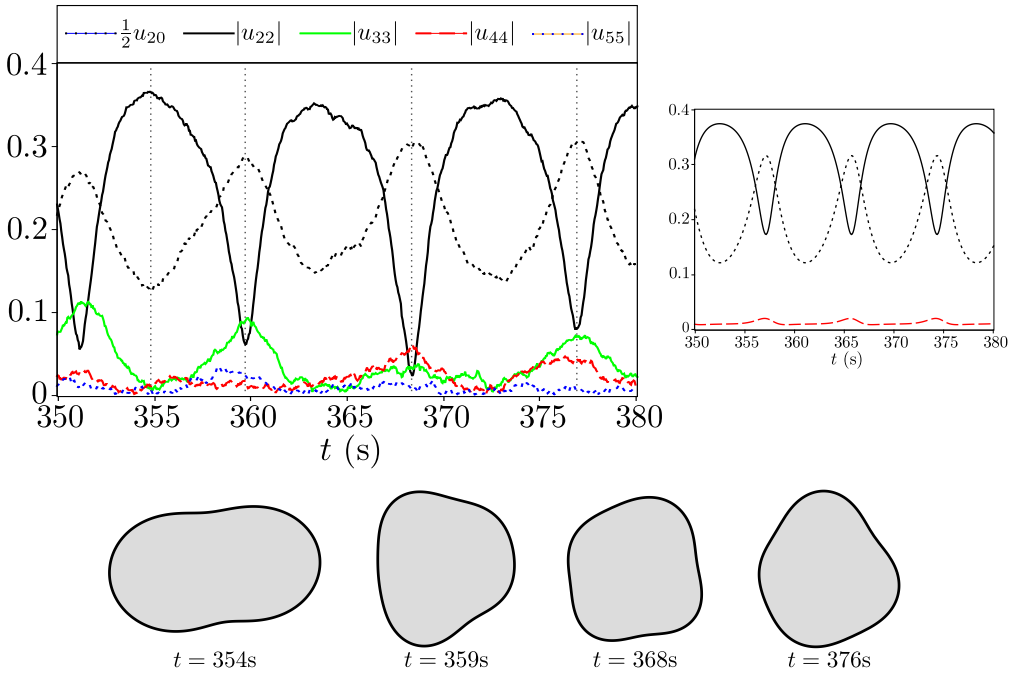

Figure 5.5.: Top: Evolution of some mode amplitudes for $\Delta = 0.66$, $S = 60.7$, and $\Lambda = 1.8$ (corresponding to $s = 0.14\,\mathrm{s}^{-1}$ and $\omega = 0.44\,\mathrm{s}^{-1}$). The right panel shows the corresponding deterministic dynamics. Bottom: Instantaneous shape contours in the flow plane at four different times corresponding to the vertical lines in the plot.

evolution of the coefficients u_{20} and $|u_{ll}|$ ($l = 2, ..., 5$) for a typical mixed TR and TB motion, using the same parameters as in the experimental results of fig. 2 of Ref. [139]. For these parameters, the deterministic model predicts a TB motion for which the odd harmonics $|u_{33}|$ and $|u_{55}|$ are strictly equal to zero, whereas $|u_{44}|$ remains much smaller than u_{20} and $|u_{22}|$. With thermal noise, all modes are excited. In particular, $|u_{33}|$ and $|u_{44}|$ become regularly larger that $|u_{22}|$, leading to strongly distorted shapes. Such shapes are shown by the four snapshots, which are similar to the experimental ones [139]. The first shape is for a positive inclination angle, for which the vesicle is stretched by the external flow. The three other shapes are for negative inclination angles, i.e. the vesicle is compressed by the external flow. The excess area from that $|u_{22}|$ loses during these compression phases does not only go to u_{20} as in VB but also to higher-order modes. The TR motion presented here exists only with thermal fluctuations and is a dynamical steady state.

This kind of shape deformations are also present in TB, since the vesicle also passes through negative inclination angles. However, for large vorticities ω, the

time for which the vesicle is compressed is short and large deformations cannot build up. In the TT regime, the second mode $|u_{22}|$ is dominant and only small shape fluctuations are observed. TB and TT are therefore similar to deterministic predictions. However, at the transition between these two regimes, thermal fluctuations become crucial for the dynamics. As an aside, appendix D shows that for two-dimensional vesicles, no deterministic VB regime exists but the inclusion of thermal fluctuations also results in a TR regime at the TT-TB transition. The TR motion is therefore not just a noisy VB. In the following, we will take a closer look at the statistical properties of the different regimes.

5.3. Statistical analysis

The set of coupled Langevin equations (5.10) that describes our system can be transformed into a Fokker-Planck equation as shown in section 2.2. At constant external flow parameters s and ω, the system has a unique steady-state probability distribution. Therefore, we can characterise the system by its statistical properties and compare these directly to experiments [117, 122, 136, 137, 139]. We will first investigate the power spectra of shape deformations in the different regimes, before constructing the phase diagram of the system.

5.3.1. Power spectrum

The coupling between modes with even l and m is given by the third-order terms of Eqs. (5.4) and (5.7). This coupling becomes stronger with increasing excess area Δ. Consequently, the distinction between the power spectra of shape deformations in TT, TR, and TB becomes stronger at large Δ. The power spectrum is here defined as the mean value of $|u_{ll}|^2$ (rescaled by Δ as the second-order terms of eq. (5.5) suggest) as a function of l, as shown in fig. 5.6 in the three regimes for $S = 30$ and four values of Δ.

In the TT regime, the flow stretches the vesicle making u_{22} the dominant harmonic and suppressing higher-order ones. Already for $\Delta = 0.1$, these features distinguish the TT power spectrum from the equilibrium one [25]. By increasing Δ, the coupling between even modes becomes stronger, and in addition s becomes larger (since S is constant) thus suppressing the effect of thermal fluctuations. Therefore, the odd harmonics u_{33} and u_{55}, which are only there due to thermal noise, are suppressed while u_{44}, which is directly coupled to u_{22}, is excited. This characteristic sawtooth shape has been observed in experiments as well [137, 139]. The TB spectrum presents a similar behaviour although the sawtooth shape is less marked because odd harmonics are excited during compression phases at negative inclination angles.

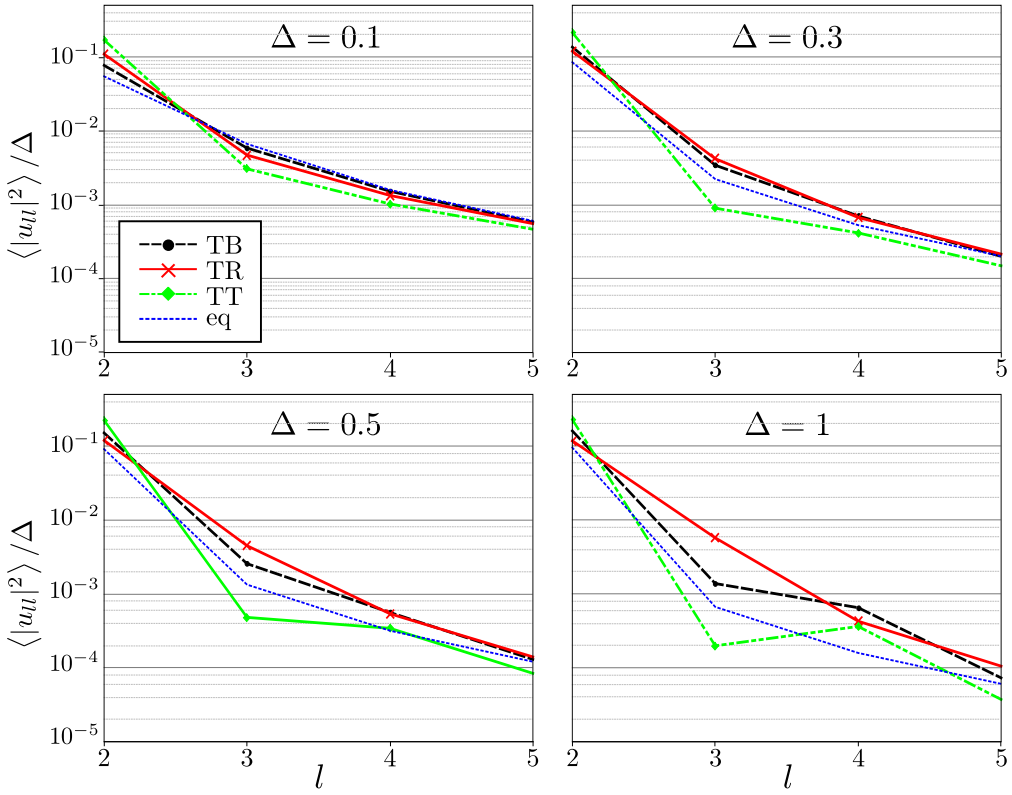

Figure 5.6.: Power spectra of the rescaled amplitudes $|u_{ll}|^2/\Delta$ as a function of the mode number $l = 2, ..., 5$ for $S = 30$ and $\Lambda = 0.8$ (TT, green dash-dotted line), 1.5 (TR, red full line) and 2.5 (TB, black dashed line) and four different excess areas Δ. The blue dotted lines are the corresponding equilibrium spectra [25].

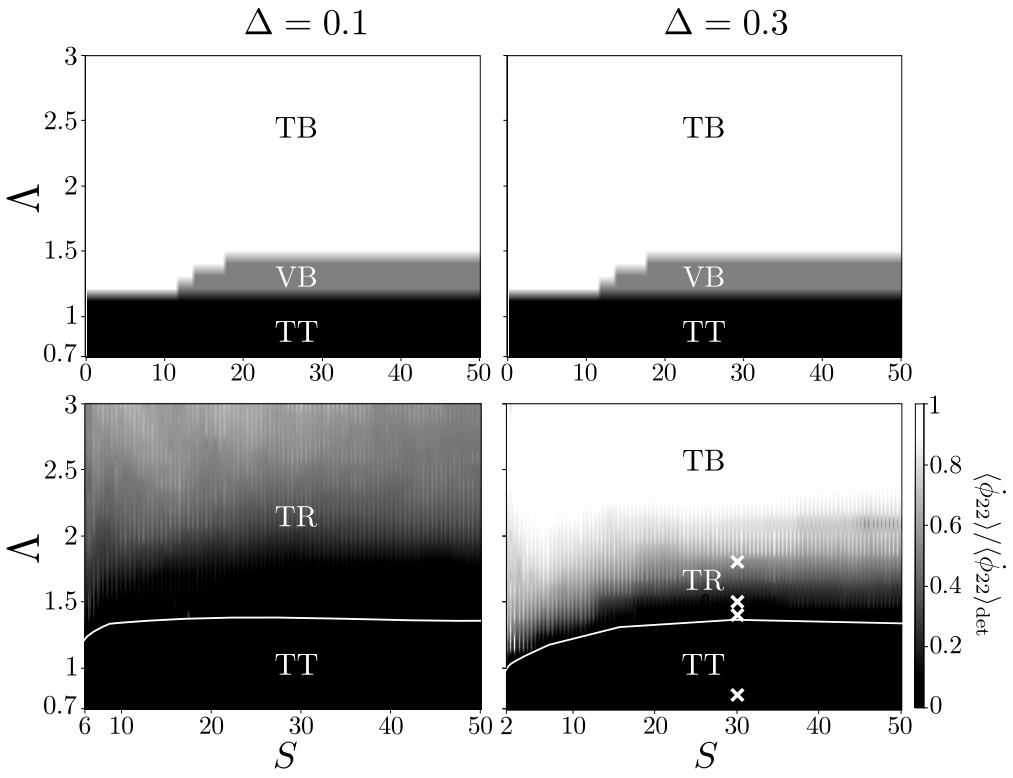

Figure 5.7.: Top: Deterministic phase diagram. Bottom: Stochastic phase diagram representing the mean velocity $\langle\dot{\phi}_{22}\rangle$ rescaled by the deterministic one $\langle\dot{\phi}_{22}\rangle_{\mathrm{det}}$ as a function of the dimensionless variables S and Λ for $\Delta = 0.1$ and 0.3. The white lines correspond to the TT-TR transition. The four crosses correspond to fig. 5.4.

In contrast, the power spectrum in the TR is qualitatively different from the TT and TB ones. Its main feature is that, even for large excess areas Δ, the third-order mode u_{33} remains larger than u_{44}, even though it is not deterministically coupled to the second mode u_{22}. The fifth-order mode u_{55} is also larger than in the other regimes. These properties come from the amplification of thermal noise in the TR regime [139] and distinguish clearly the three regimes. However, in order to construct the phase diagram presented in the next section, we only considered the dynamics of the orientation angle ϕ_{22} which is easier to treat systematically.

5.3.2. Phase diagram

The phase diagram of the system is shown in fig. 5.7 for two different excess areas with and without thermal noise. In the deterministic case (top), the TT, VB, and TB regimes can be identified without ambiguity. In the stochastic case (bottom),

the transitions between the different regimes are smoothed out by thermal fluctuations. Therefore, we choose the mean tumbling velocity $\langle\dot{\phi}_{22}\rangle$ as a continuous order parameter. When the deterministic prediction is TB, we rescale this order parameter by the deterministic mean velocity $\langle\dot{\phi}_{22}\rangle_{\text{det}} > 0$ so that we clearly see the effect of thermal noise. In the TB regime, this ratio is close to 1 (white regions) while it is almost 0 in the TT and TR regimes (black regions). The grey regions indicate a mixed TR and TB motion (see fig. 5.4 for $\Lambda = 1.8$). We further define TT as the regime in which the mean orientation angle is larger than its standard deviation, such that we are able to distinguish between TT and TR. For small S, the dynamics is dominated mainly by diffusive motion of the orientation angle, making it hard to distinguish between different regimes. For this reason, the lower phase diagrams do not extend to $S = 0$.

The first striking feature is that the TT-TR transition happens approximately at fixed values of Λ for all Δ in agreement with experimental observations [117, 136, 137]. Moreover, the width of the TR region for both values of Δ is only comparable to the experimental one if thermal noise is included. Therefore, we can conclude that thermal fluctuations widen the TR region dramatically and are thus necessary to explain experiments. In addition, the two stochastic phase diagram of fig. 5.7 have a great overlap which might explain why S and Λ are so effective to classify the experimental data [137]. Of course, the vesicles used in experiments have typically larger excess areas. If we go to larger Δ in our model, the TR region becomes thinner. However, further corrections might then be necessary. For instance, the deterministic model of [60] shows that the VB region becomes larger with Δ and S if next-order hydrodynamic terms are included. In section 6.3.2, these corrections are implemented and a TR motion is still observed for $\Delta > 1$ and $\Lambda > 2$ at large S, in accordance with the widening of the experimental phase diagram with growing S [137].

5.4. Conclusion

We have shown that thermal fluctuations are crucial to understand the dynamics of GUVs in linear flow, even though these vesicles are large and the ratio $k_BT/\kappa \sim 0.04$ is small. The reason is that the non-linear dynamics of the vesicle is very sensible to small perturbations close to the TT-TB transition, a phenomenon reminiscent of the prebifurcation noise amplification analysed in [255–257]. In our case, the small perturbations correspond to the always present thermal fluctuations which incessantly destabilize the system, generating the trembling motion. As already pointed out in section 3.2, our results thus give an explanation for the strong shape fluctuations observed in experiments that are not predicted by deterministic models thus resolving a long-standing controversy.

Of course, our results are based on a simplified model for quasi-spherical vesicles and are thus not in full quantitative agreement with experiments. It would be interesting to investigate the TR motion in more complex numeric schemes taking thermal fluctuations into account, see section 3.1.2. Moreover, the influence of thermal noise on rheology still has to be investigated.

6. Wrinkling of vesicles in linear flow

In chapter 5, we investigated the TR motion happening at low flow rates ($S \lesssim 60$). In the present chapter, we consider the possible appearance of wrinkles in stronger flows. A vesicle in TR motion is compressed by the external flow when its orientation angle Θ takes negative values. At large enough S, one can expect short-wavelength deformations to appear as illustrated by fig. 6.1. This mechanism is similar to the transient wrinkling observed in a suddenly reversed elongation flow, see section 3.2.5. However, the wrinkling described here happens in stationary flow and is a steady-state dynamical property of TR a large S.

We first describe the model and the main quantities of interest. We then present experimental observations, and explain them theoretically through analytical considerations and numerical simulations. The experiments have been performed by M. Levant at the Weizmann Institute in Rehovot, Israel. The results presented in this chapter have been submitted for publication [154].

6.1. Model

The basic modelling of the vesicle and the notation is the same as in section 5.1. We consider a quasi-spherical vesicle of radius (5.1) in a general linear flow of the form (3.1). The equation of motion to lowest order for the modes u_{lm} (5.8) can be written in dimensionless form as

$$\tau\partial_t u_{lm} = i\frac{S\Lambda}{2}u_{lm} - \nu_l(l(l+1)+\sigma_{00})u_{lm} - i\frac{S}{2}\sqrt{\Delta}\varepsilon_{lm} + \tau\zeta_{lm} \tag{6.1}$$

with $\nu_l \equiv (l-1)(l+2)\tau\mu_l$ and the characteristic timescale [151]

$$\tau \equiv \frac{385}{72}\sqrt{\frac{\pi}{10\Delta}}\frac{\eta_{out}R_0^3}{\kappa}. \tag{6.2}$$

The correlations of the Gaussian white noise ζ_{lm} are given by eq. (5.9).

In Eq. (6.1), the term $iS\sqrt{\Delta}\varepsilon_{lm}/2$ is derived from the quantities X^∞ and Y^∞ defined as in eq. (2.15) describing the external flow $\mathbf{v}^\infty$ at the virtual sphere $r = R_0$ [41], see appendix B. If we instead define X^∞ and Y^∞ at $r = R_0(1+u)$, correction terms of the form Su_{lm} will induce a coupling between $u_{2,\pm2}$ and higher-order modes with even l and m, see appendix B for the detailed derivation. The

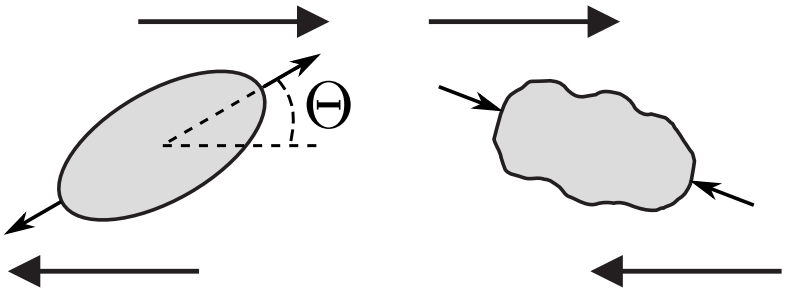

Figure 6.1.: Schematic representation of the wrinkling instability in linear flow. When the inclination angle Θ is positive, the vesicle is almost ellipsoidal, while for negative Θ, short-wavelength deformations may appear due to compression.

numerical results of section 6.3.2 are obtained by simulating eqs. (6.1) for all harmonics between $l = 2$ and $l = 16$ (150 coupled equations) with these additional flow correction terms. Contrary to chapter 5, we do not take third-order terms in the bending energy into account for computational reasons. The simulation method is detailed in appendix C.

In order to compare the simulations with the experiments, the shape in the flow plane $\theta = \pi/2$ is expanded in Fourier coefficients a_k as

$$R(\pi/2,\phi) = R_0\left(1+\sum_{l=0}^{\infty}\sum_{m=-l}^{l} u_{lm}\mathcal{Y}_{lm}(\pi/2,0)e^{im\phi}\right) \equiv R_0\left(1+\sum_{k=-\infty}^{+\infty} a_k e^{ik\phi}\right). \tag{6.3}$$

The inclination angle Θ is defined through the second mode

$$a_2 \equiv |a_2|\exp(-2i\Theta). \tag{6.4}$$

We quantify the presence of high-order modes in the vesicle shape with the mean wave number

$$k^* = \sqrt{\frac{\sum_{k=3}^{k_{\max}} k^2|a_k|^2}{\sum_{k=3}^{k_{\max}} |a_k|^2}} \tag{6.5}$$

where the highest wave number $k_{\max}$ is determined by the experimental or numerical precision. In the following, we will set $k_{\max} = 16$. We also define the quantities k^*_{even} and k^*_{odd} by performing the sums in eq. (6.5) only over even or odd modes, respectively. These two quantities will be important to analyse the asymmetry between even and odd modes induced by the hydrodynamical corrections discussed above.

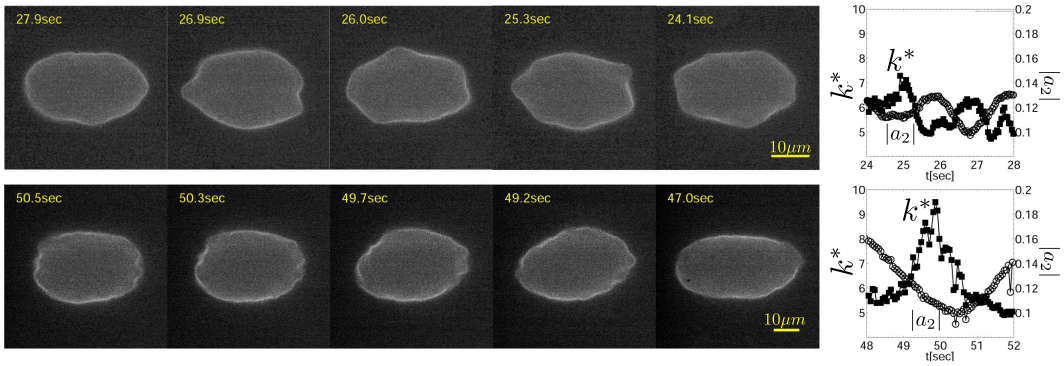

Figure 6.2.: Snapshots of vesicles in TR at $S = 421$, $\Lambda = 1.87$, $\Delta = 1.22$ (top) and $S = 1147$, $\Lambda = 1.78$, $\Delta = 1.27$ (bottom). The corresponding time series of k^* and $|a_2|$ are shown on the right.

6.2. Experimental observations

Fig. 6.2 shows experimental snapshots of wrinkled vesicles. The time series for $S = 1147$ shows deformations with a shorter wavelength, i.e. a larger k^* than for $S = 421$. A simplified explanation for that observation is that when the inclination angle becomes negative, $|a_2|$ decreases and the thus available excess area goes either to u_0 or to higher-order modes. This transfer of excess area may lead to an increase of k^*, whose maximal value is then roughly determined by the strength S of the elongational part of the flow. These arguments are, however, only approximate since other factors such as the minimal inclination angle or random fluctuations enter into account.

A more detailed dynamical picture is provided by fig. 6.3. The first interesting feature is that the mode $|a_4|$ is synchronized with $|a_2|$ but with half the period - $|a_4|$ exhibits maxima when $|a_2|$ is minimal, but also when it is maximal. At the same time, the mean wave number of the even modes k^*_{even} is almost perfectly anti-correlated with $|a_4|$. On the contrary, k^*_{odd} has very erratic dynamics which are only slightly correlated with $|a_2|$. Therefore, all even modes are coupled together by the TR dynamics while the odd modes are mostly randomly excited by thermal fluctuations.

In the experiments in elongational flow of [133], k^* scales with the strength of the flow to the power of 1/4 above a critical elongation rate. One can thus wonder if a similar scaling exists in linear flow. Fig. 6.4(a) shows that the probability density of k^* for $S = 1147$ as a larger mean value and a fatter tail as the one for $S = 60.7$. The corresponding power spectra indicate an amplification of high-order modes for larger S. Consequently, we can expect the mean value of k^* to increase with S. Such an increase should by even clearer if we consider k^*_{even} since

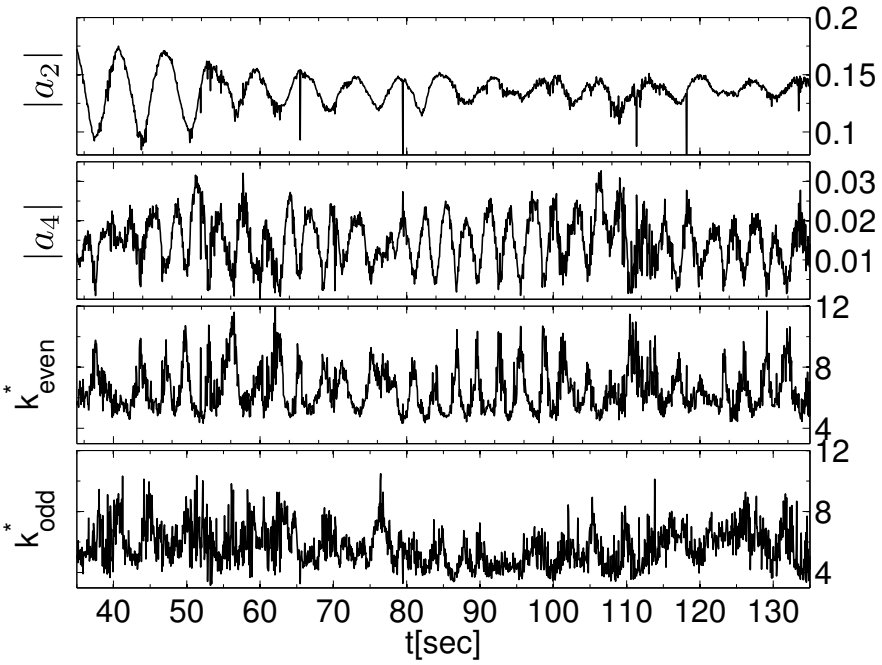

Figure 6.3.: Dynamics of $|a_2|$, $|a_4|$, k^*_{even}, and k^*_{odd} at $S = 1147$, $\Lambda = 1.78$, and $\Delta = 1.27$.

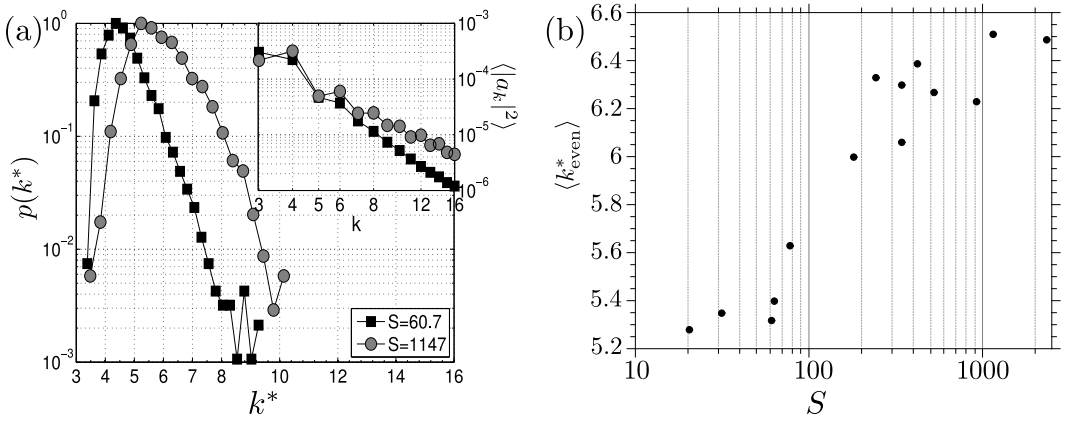

Figure 6.4.: (a) Probability distribution function of k^* for $S = 60.7$, $\Lambda = 1.8$, $\Delta = 0.66$, and $S = 1147; \Lambda = 1.78; \Delta = 1.27$. The inset shows the corresponding power spectra. (b) Mean wave number of the even modes $\langle k^*_{\text{even}} \rangle$ as a function of the dimensionless elongation rate S for various Λ and Δ given in fig. 6.5.

it has a much more regular dynamics than k^* which also contains k^*_{odd}, see fig. 6.3. In Fig. 6.4(b), we plot the mean wave number $\langle k^*_{\mathrm{even}} \rangle$ as a function of S for various vesicles, where the brackets denote the average over long trajectories. It is hard to read any clear exponential dependence because of the dispersion of the data. Nevertheless, an increase above $S \sim 60$ is clearly visible, even though these vesicles have a wide range of excess areas $\Delta \in [0.43; 1.65]$ and $\Lambda \in [1.3; 2.42]$. The dimensionless elongation rate S is thus the main control parameter for the wrinkling instability, a fact that we investigate theoretically in section 6.3.

6.3. Theoretical analysis

The main mechanism triggering the wrinkling instability can already be understood with the equations to lowest order (6.1) as shown in section 6.3.1. However, in order to reproduce accurately the experimental observations, the hydrodynamic corrections discussed in section 6.1 must be taken into account. The equations of motion are then solved numerically. These numerical results are presented in section 6.3.2.

6.3.1. Low-order considerations

We first neglect thermal noise and decompose the expansion coefficients as

$$u_{lm} \equiv |u_{lm}| \exp(-im\phi_{lm}). \tag{6.6}$$

From eq. (6.1) we obtain the equation of motion

$$\tau \partial_t |u_{lm}| = -\nu_l (l(l+1) + \sigma_{00}) |u_{lm}| + \frac{S}{2} |u_{22}| \sin(2\phi_{22}) \varepsilon_{lm} \tag{6.7}$$

for the amplitudes $|u_{lm}|$. For $(l, m) \neq (2, \pm 2)$, $\varepsilon_{lm} = 0$ and Eq. (6.7) describes an exponential decay or growth, depending on the sign of $l(l+1) + \sigma_{00}$. The surface tension σ can be obtained from the condition that the excess area Δ (5.5) remains constant to lowest order, i.e, that the equality

$$\Delta = \sum_{l,m} \frac{(l-1)(l+2)}{2} |u_{lm}|^2 \tag{6.8}$$

is always obeyed. Taking the time-derivative of Eq. (6.8) leads to

$$l(l+1) + \sigma_{00} = \frac{4S|u_{22}| \sin(2\phi_{22}) + \sum_{l',m'} [l(l+1) - l'(l'+1)](l'-1)(l'+2)\nu_{l'} |u_{l'm'}|^2}{\sum_{l',m'} (l'-1)(l'+2)\nu_{l'} |u_{l'm'}|^2}. \tag{6.9}$$

Whether the mode (l, m) decays or grows depends on the sign of (6.9). We first see that positive contributions come from all modes with $l' < l$: the excess area is transferred from high-order modes to low-order ones. Moreover, the external flow has a contribution which has the sign of the angle ϕ_{22}, which is approximately the inclination angle, and a strength proportional to S. In TR and TB motions, the flow compresses the vesicle when the inclination angle takes negative values, leading to negative surface tension and amplification of the modes with $l(l+1) + \sigma_{00} < 0$. With increasing S, higher-order modes will be excited during compression phases since the surface tension will take larger negative values. However, harmonics with $l > 2$ obeying Eq. (6.7) will decay to 0 in the long run due to the stretching at positive inclination angles and the transfer of excess area from high to low-order harmonics. The deterministic low-order equations therefore only predict a transient wrinkling similar to the one observed in elongation flow, see section 3.2.5.

The hydrodynamic correction terms introduced in section 6.1 will induce a coupling between $u_{2,\pm2}$ and higher-order modes with even l and m. However, modes with odd l and/or m will still vanish. Therefore, we have to take thermal noise into account to explain the presence of odd modes in experiments. In section 6.3.2, we show that thermal fluctuations are not only responsible for the presence of odd modes, but also for the dynamics of the even modes observed in section 6.2.

6.3.2. Numerical results

All simulations with the same physical parameters as in fig. 6.4 predict a TR motion in the steady state. The root mean square of Θ in simulations is comparable to the experimental measurements as shown in fig. 6.5. As already discussed at the end of section 5.3.2, this is a hint that the numerical phase diagram would be in good agreement with the experimental one even at large S.

Fig. 6.6 shows a simulated trajectory for $S = 1147$, $\Lambda = 1.78$, and $\Delta = 1.27$ corresponding to fig. 6.2 bottom. The first panel shows the almost regular oscillation of the inclination angle Θ around 0. The amplitude of the second mode $|a_2|$ oscillates with the same period, which is comparable to the experimental one (see fig. 6.3), although it lags slightly behind Θ. The surface tension σ shown in the second panel, which corresponds to Eq. (6.9) with flow correction terms, is strongly correlated with Θ, reaching minima and maxima almost at the same times. This strong correlation is the basis of the wrinkling phenomenon. The third and fourth panel show k^*_{even} and k^*_{odd}, respectively. As in the experimental data of fig. 6.3, k^*_{odd} exhibits a rather erratic evolution while k^*_{even} is regular since even modes are coupled by the flow. Moreover, like in the experiments, k^*_{even} has a period approximately equal to half the period of Θ. This fact is due to thermal fluctuations, as explained below.

Δ	Λ	S	$\Theta_{\mathrm{rms,exp}}$	$\Theta_{\mathrm{rms,sim}}$
0.99	1.3	2334	0.0532	0.0267
0.43	1.87	76.8	0.14	0.1947
0.95	1.44	241	0.099	0.0505
0.66	1.8	60.7	0.2	0.1781
0.5	2	62.8	0.085	0.2437
0.95	1.75	20.3	0.1658	0.3310
1.13	1.8	180	0.089	0.0722
1.27	1.78	1147	0.064	0.0525
1.22	1.87	421	0.0392	0.0603
1.17	1.94	31.1	0.11	0.2852
1.08	2.05	521	0.0362	0.0696
1.05	2.42	338	0.525	0.1002
1.31	2.26	915	0.0775	0.0792
1.65	2.17	38	0.061	0.0748

Figure 6.5.: Comparison of the root mean square (rms) of the inclination angle Θ in experiments and simulations at different values of Δ, Λ, and S. For each set of parameters, we simulated 10 steady-state trajectories of approximately 500 periods to obtain a mean $\Theta_{\mathrm{rms,sim}}$ with a standard deviation of $\pm 10\%$.

Fig. 6.7 compares the evolution of the zeroth, second, and fourth modes with that of k^*_{even}. The top panel shows the deterministic case which corresponds to a vacillating-breathing motion [55]: when the inclination angle is negative, the amplitude of the second mode $|a_2|$ decreases while $|a_0|$ and modes out of plane increase. The dynamics of all higher-order even modes, e.g., $|a_4|$, is perfectly synchronized with $|a_2|$, as is the evolution of k^*_{even}. In addition, k^*_{even} varies between 4.002 and 4.005, meaning that the fourth mode is always much larger than the higher ones. With thermal fluctuations, the picture changes dramatically. The zeroth and second modes do not show qualitative changes, but $|a_4|$ has a totally different behaviour. It now exhibits a maximum not only when $|a_2|$ is maximal but also when it is minimal. This new peak is due to the amplification of thermal noise at negative inclination angles described in chapter 5 and corresponds to the observed wrinkles. Moreover, the mean wave number k^*_{even} reaches large values, comparable with the experimental ones, and is strongly anti-correlated with $|a_4|$. The explanation is that when the inclination angle reaches its minimum, high-order deformations grow fast, thus increasing k^*_{even}. However, as Eq. (6.9) shows, this excess area is transferred to low-order deformations, leading to a decrease of k^*_{even} and a growth of $|a_4|$, which promptly decreases again in favor of $|a_2|$. Then the inclination angle becomes positive, and $|a_4|$ increases again due to the

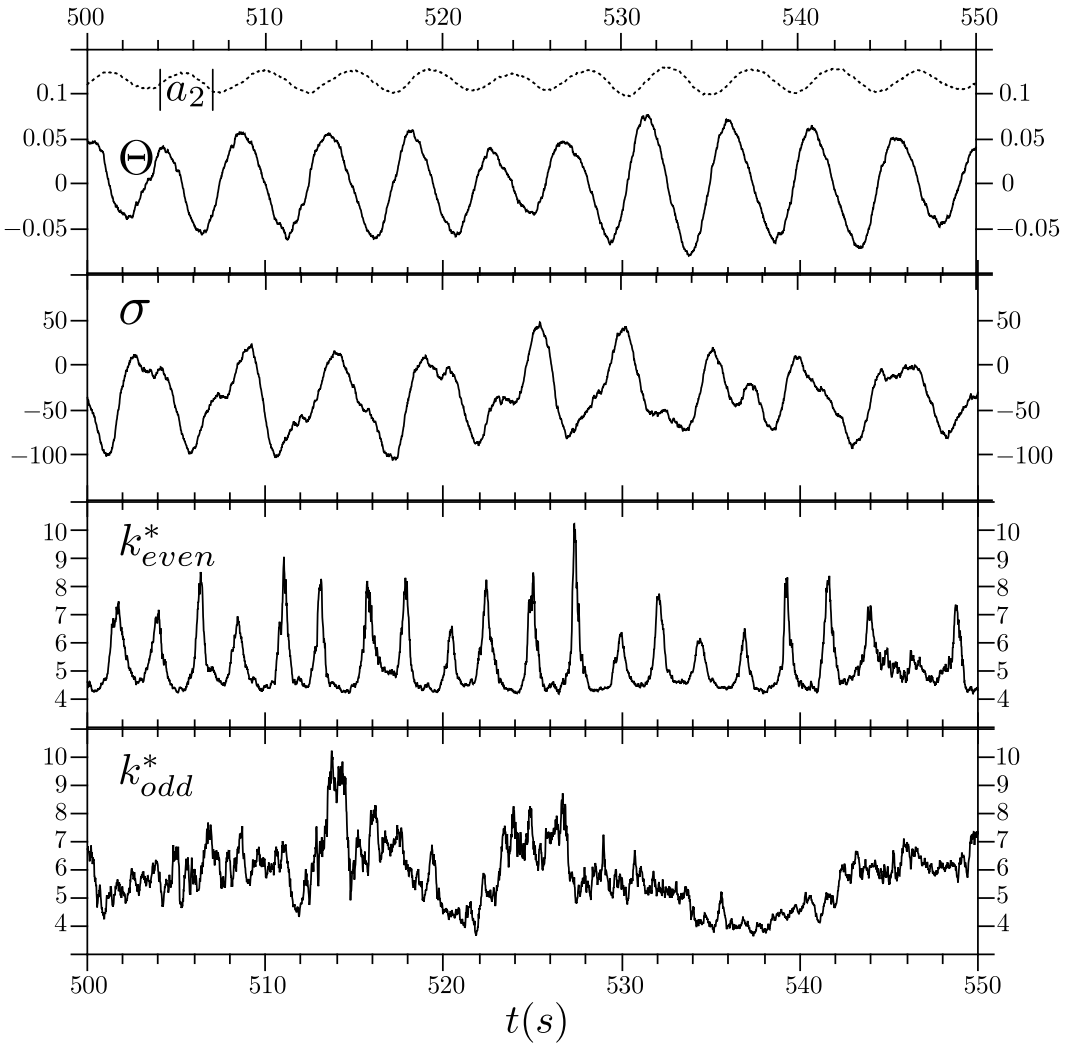

Figure 6.6.: Dynamics of the inclination angle Θ (full line) and the second mode amplitude $|a_2|$ (dashed), the surface tension σ, and the mean wave numbers k^*_{even} and k^*_{odd} for $S = 1147$, $\Lambda = 1.78$, and $\Delta = 1.27$.

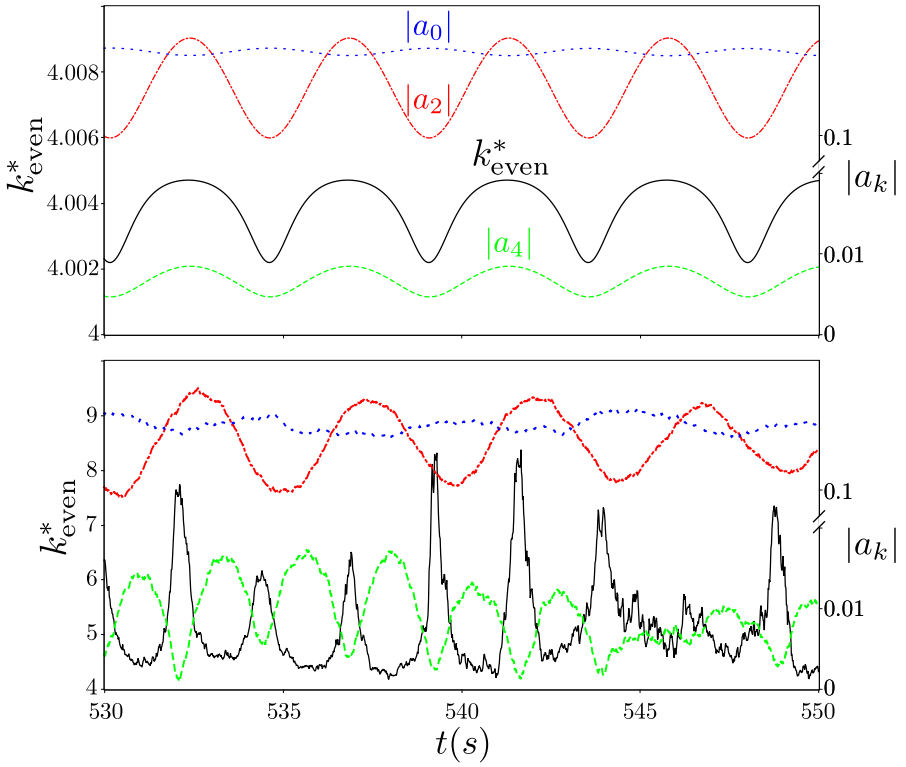

Figure 6.7.: Evolution of $|a_0|$ (blue dots), $|a_2|$ (red dash-dots), $|a_4|$ (green dashes), and k^*_{even} (black) without (top) and with (bottom) thermal noise. The left scale is for k^*_{even} and the right one (which has a break) for the $|a_k|$.

deterministic coupling with $|a_2|$. Therefore, thermal fluctuations not only excite odd modes, but change drastically the dynamics of the even modes as well.

Fig. 6.8 shows further comparisons of simulation results with experimental ones. The probability distribution function of k^* of Fig. 6.8(a) shows the same main features as fig. 6.4(a) : for $S = 1147$, it has a larger tail and a higher average than for $S = 60.7$, even though the difference is not as large as in the experiments. Furthermore, the simulations could not reproduce the transition shown in fig. 6.4(b) due to a marked dependence not only on S but also on Λ and Δ. Fig. 6.8(b) shows, however, that for fixed Δ and Λ, the expected increase in the average k^*_{even} is observed, although with a smaller magnitude than in experiments. The snapshots at $S = 421$ of Fig. 6.8(c) show clearly visible wrinkles which are, however, not as pronounced as the ones of Fig. 6.2. The numerical results seem to underestimate the experimental ones. This discrepancy is probably due to the quasi-spherical approximation which does not describe faithfully vesicles with large Δ. However, in spite of this approximation, the model still captures most experimental features, mainly because it includes thermal fluctuations consistently.

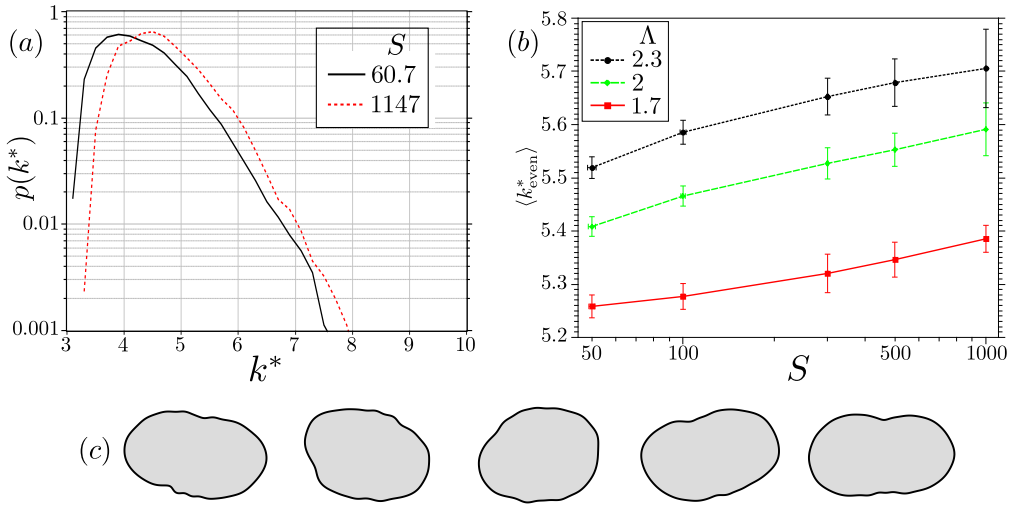

Figure 6.8.: (a) Probability distribution function of k^* for $S = 60.7$, $\Lambda = 1.8, \Delta = 0.66$, and $S = 1147$, $\Lambda = 1.78, \Delta = 1.27$. (b) Mean k^*_{even} as a function of S for $\Delta = 1$ and different values of Λ. (c) Snapshots from simulations at $S = 421$, $\Lambda = 1.87, \Delta = 1.22$.

6.4. Conclusion

We have shown that a wrinkling instability occurs for vesicles in the TR regime at large enough strain rates. Even though the dynamics is much more complex than in pure elongation flow, the experiments show that the normalized strain rate S is the main control parameter triggering the instability. The onset of wrinkling occurs approximately above $S \simeq 60$, which comes from a statistical analysis of the power spectrum. The main experimental features are reproduced by a simple numerical model, which shows that thermal fluctuations are crucial to describe wrinkling correctly.

This model does not, however, provide a full quantitative agreement with the experiments due to the quasi-spherical approximation. In order to compare theory and experiment on a more quantitative level, it would be interesting to include thermal noise in more complex numerical schemes such as [78, 98] which show a strong coupling between even modes at large S, or to analyse single TR vesicles with the algorithm of [109, 112], which already takes thermal fluctuations into account. Finally, whether the results of chapters 5 and 6 can be generalised to similar objects such as elastic capsules or RBCs remains to be seen.

A. Spherical Harmonics

In spherical coordinates (r, θ, ϕ), Laplace's equation

$$\nabla^2 f = 0 \tag{A.1}$$

is solved by the solid spherical harmonics

$$f_{lm}(r, \theta, \phi) = r^l \mathcal{Y}_{lm}, \tag{A.2}$$

where $l \in \mathbb{Z}$ and $m \in [-l, l]$. The spherical harmonics $\mathcal{Y}_{lm}$ are eigenvectors of the Laplace-Beltrami operator on the surface

$$\Delta_s \equiv \nabla_s^2 = \left(\mathbf{e}_\theta \partial_\theta + \frac{\mathbf{e}_\phi}{\sin\theta}\partial_\phi\right)^2 = \frac{\partial^2}{\partial\theta^2} + \frac{1}{\sin^2\theta}\frac{\partial^2}{\partial\phi^2} + \cot\theta\frac{\partial}{\partial\theta} \tag{A.3}$$

with eigenvalues

$$\Delta_s \mathcal{Y}_{lm} = -l(l+1)\mathcal{Y}_{lm}. \tag{A.4}$$

A detailed description of spherical harmonics can be found in [258]. They are explicitly given by

$$\mathcal{Y}_{lm}(\theta, \phi) = \sqrt{\frac{2l+1}{4\pi}\frac{(l-m)!}{(l+m)!}} P_l^m(\cos\theta) e^{im\phi} \tag{A.5}$$

where $l \geq 0$, $m \in [-l, l]$, P_l^m are the associated Legendre polynomials, $\theta \in [0, \pi]$ is the polar angle, and $\phi \in [0, 2\pi]$ the longitudinal one, see Fig 5.1. The spherical harmonics can be extended to negative l by defining

$$\mathcal{Y}_{lm} \equiv \mathcal{Y}_{-(l+1)m}. \tag{A.6}$$

The associated Legendre polynomials are defined as

$$P_l^m(x) = \frac{(-1)^l}{2^l l!}(1-x^2)^{m/2}\frac{d^{l+m}}{dx^{l+m}}(x^2-1)^l \tag{A.7}$$

for $m \geq 0$, and extended to negative m by the relation

$$P_l^{-m}(x) = (-1)^m \frac{(l-m)!}{(l+m)!} P_l^m(x). \tag{A.8}$$

This last relation implies

$$\mathcal{Y}_{l-m}(\theta,\phi) = (-1)^m \mathcal{Y}^*_{lm}(\theta,\phi). \tag{A.9}$$

The spherical harmonics are normalized as

$$\int_0^{2\pi}\int_0^{\pi} \mathcal{Y}_{lm}(\theta,\phi)\mathcal{Y}^*_{l'm'}(\theta,\phi)\sin\theta\,\mathrm{d}\theta\,\mathrm{d}\phi = \delta_{ll'}\delta_{mm'}. \tag{A.10}$$

The integral over the product of three spherical harmonics is equal to

$$\begin{aligned} C^{lm}_{123} &= \int_0^{2\pi}\int_0^{\pi} \mathcal{Y}_{l_1m_1}\mathcal{Y}_{l_2m_2}\mathcal{Y}_{l_3m_3}\sin\theta\,\mathrm{d}\theta\,\mathrm{d}\phi \\ &= \sqrt{\frac{(2l_1+1)(2l_2+1)(2l_3+1)}{4\pi}} \begin{pmatrix} l_1 & l_2 & l_3 \\ 0 & 0 & 0 \end{pmatrix} \begin{pmatrix} l_1 & l_2 & l_3 \\ m_1 & m_2 & m_3 \end{pmatrix} \end{aligned} \tag{A.11}$$

where the terms in parenthesis are Wigner $3j$-symbols [258].

B. Quasi-spherical expansions

In this appendix, we present detailed calculations needed to construct the models of chapters 5 and 6. We first derive the expansions used in section 5.1.1, then calculate the hydrodynamic corrections mentioned in section 6.1.

Area, volume, bending energy In this paragraph, we adapt the results of [252] to expand the surface area, the volume and the bending energy of a vesicle to third-order in the coefficients u_{lm} of the quasi-spherical expansion (5.1). In [252], the equilibrium shape $\mathbf{Y}'$ of a vesicle is expanded as

$$\mathbf{Y}' = \mathbf{Y} + \psi(u, v)\mathbf{n} \tag{B.1}$$

where $\mathbf{Y}$ is the equilibrium configuration. In our notation, we have $\mathbf{Y} \equiv R_0\mathbf{e_r}$, $\mathbf{n} \equiv \mathbf{e_r}$, and

$$\psi(u, v) \equiv R_0 u(\theta, \phi) = R_0 \sum_{l,m} u_{lm}\mathcal{Y}_{lm}. \tag{B.2}$$

The properties of the spherical harmonics $\mathcal{Y}_{lm}$ are recalled in appendix A and are important to perform the integrals below. Using eqs. (42) and (80) of [252], we find for the area

$$A = 4\pi R_0^2 + R_0^2 \oint \left[2u + u^2 - \frac{1}{2}u\Delta_s u + O(u^4)\right] \sin\theta \,\mathrm{d}\theta \,\mathrm{d}\phi. \tag{B.3}$$

The integral of the first term of the integrand vanishes for all (l, m) except $(0, 0)$. The second term can be calculated with the normalisation property (A.10). The third term first has to be transformed with (A.4). As a result we obtain for the area

$$A = R_0^2 \left[4\pi \left(1 + \frac{u_{00}}{\sqrt{4\pi}}\right)^2 + \sum_{l\geq 1} \left(1 + \frac{l(l+1)}{2}\right) |u_{lm}|^2\right] + O(u^4). \tag{B.4}$$

Similarly, the vesicle volume is given by

$$V = \frac{4\pi}{3}R_0^3 + R_0^3 \oint \left[u + u^2 + \frac{u^3}{3} + O(u^4)\right] \sin\theta \,\mathrm{d}\theta \,\mathrm{d}\phi \tag{B.5}$$

The integral of the u^3 term is calculated with (A.11). The volume then reads

$$V = R_0^3 \left[\frac{4\pi}{3} \left(1 + \frac{u_{00}}{\sqrt{4\pi}} \right)^3 + \left(1 + \frac{u_{00}}{3\sqrt{4\pi}} \right) \sum_{l \geq 1} |u_{lm}|^2 + \sum_{l_i \geq 1} \frac{C_{123}^{lm}}{3} u_{l_1 m_1} u_{l_2 m_2} u_{l_3 m_3} \right] + O(u^4). \tag{B.6}$$

The bending energy can be derived from the general equations of [252]. The calculation is straightforward but is not shown here since it is pretty lengthy and can be found in details in [253]. The integral form the bending energy (2.41) without the surface tension σ reads

$$\mathcal{H}_\kappa = 8\pi\kappa + \frac{\kappa}{2} \oint \left[2u\Delta_s u + (\Delta_s u)^2 + O(u^4) \right] \sin\theta \, \mathrm{d}\theta \, \mathrm{d}\phi \tag{B.7}$$
$$+ \frac{\kappa}{2} \oint \left[-4u^2 \Delta_s u - 2u(\Delta_s u)^2 - 4u(\nabla_s u)^2 + 2\nabla_s u \cdot \nabla_s ((\nabla_s u)^2) \right] \sin\theta \, \mathrm{d}\theta \, \mathrm{d}\phi.$$

This integral can be transformed as into the sum [253]

$$\mathcal{H}_\kappa = 8\pi\kappa + \frac{\kappa}{2} \sum_{l \geq 1, m} (l-1) l (l+1)(l+2) |u_{lm}|^2 + \frac{\kappa}{2} \sum_{l_i \geq 1, m} (l_1 - 1) l_1 (l_1 + 1)(l_1 + 2) C_{123}^{lm} u_{l_1 m_1} u_{l_2 m_2} u_{l_3 m_3} + O(u^4). \tag{B.8}$$

Flow correction terms In [41], linear flows of the form

$$\mathbf{v}^\infty(\mathbf{r}) \equiv \mathcal{G}\mathbf{r} \equiv \mathcal{G}_s \mathbf{r} + \boldsymbol{\Omega} \times \mathbf{r} \tag{B.9}$$

are considered, where $\mathcal{G}$ is a traceless $\mathbf{r}$-independent matrix, $\mathcal{G}_s$ its symmetric part and $\boldsymbol{\Omega} = \Omega \mathbf{e}_z$ the vorticity vector describing the rotational part of the flow. The quantities X^∞ and Y^∞ are defined similarly as in eq. (2.15) by

$$X^\infty \equiv \mathbf{v}^\infty(R_0, \theta, \phi) \cdot \mathbf{e}_\mathbf{r} \equiv \sum_{l,m} X_{lm}^\infty \mathcal{Y}_{lm}(\theta, \phi) \tag{B.10}$$

$$Y^\infty \equiv -R_0 \nabla \cdot \mathbf{v}^\infty(R_0, \theta, \phi) \equiv \sum_{l,m} Y_{lm}^\infty \mathcal{Y}_{lm}(\theta, \phi) \tag{B.11}$$

and describe the flow at the virtual sphere of radius R_0. The general equation of motion

$$\partial_t u_{lm} = -i\Omega u_{lm} - \mu_l (l-1)(l+2)(l(l+1) + \sigma_{00}) u_{lm} + \frac{X_{lm}^\infty + B_l Y_{lm}^\infty}{R_0} + \zeta_{lm} \tag{B.12}$$

for the coefficients u_{lm} of the expansion (5.1) is obtained, where

$$B_l = \frac{1}{2l^2 + 2l - 1}. \tag{B.13}$$

If we consider a linear flow of the form (3.1), then

$$\Omega = -\omega \qquad X^\infty_{lm} = Y^\infty_{lm} = -2isR_0\sqrt{\frac{2\pi}{15}}\delta_{l,2}(\delta_{m,2} - \delta_{m,-2}) \tag{B.14}$$

and we recover eq. (5.8).

From eqs. (B.12) and (B.14), we see that while the rotational part of the flow corresponds to a term of first order in u_{lm}, the elongational part is described by a constant term which is only non-zero for the modes $u_{2\pm2}$. To induce a hydrodynamical coupling between $u_{2\pm2}$ and higher modes, we will add correction terms to the elongation flow of first order in u_{lm}. These terms are obtained by defining X^∞ and Y^∞ not at the virtual sphere $r = R_0$ but rather at the actual membrane position $r = R_0(1 + u)$. The external flow (3.1) can be written as

$$\mathbf{v}^\infty = sr\left(\sin^2\theta\sin(2\phi)\mathbf{e_r} + \frac{1}{2}\sin(2\theta)\sin(2\phi)\mathbf{e}_\theta + \sin\theta\cos(2\phi)\mathbf{e}_\phi\right) - \omega r\sin\theta\mathbf{e}_\phi. \tag{B.15}$$

The new radial part of the flow is then equal to

$$X^\infty \equiv \mathbf{v}^\infty(R_0(1+u),\theta,\phi)\cdot\mathbf{e_r} = -2isR_0(1+u)\sqrt{\frac{2\pi}{15}}(\mathcal{Y}_{22} - \mathcal{Y}_{2,-2}) \tag{B.16}$$

with

$$\mathcal{Y}_{2\pm2} = \frac{1}{4}\sqrt{\frac{15}{2\pi}}\sin(2\theta)\exp(\pm2i\phi). \tag{B.17}$$

The divergence term becomes

$$\begin{aligned} Y^\infty &\equiv -r\nabla\cdot\mathbf{v}^\infty(R_0(1+u),\theta,\phi)|_{r=R_0(1+u)} \\ &= R_0(s\sin^2\theta\sin(2\phi) + \omega\partial_\phi u - s\cos(2\phi)\partial_\phi u - \frac{s}{2}\sin(2\theta)\sin(2\phi)\partial_\theta u) \end{aligned} \tag{B.18}$$

where the first term in the parenthesis is the zeroth order term given in eq. (B.14) and the terms with derivatives correspond to correction terms. To get the new equations of motions, we must calculate

$$\frac{X^\infty_{lm} + B_l Y^\infty_{lm}}{R_0} = \oint \frac{X^\infty + B_l Y^\infty}{R_0}\mathcal{Y}^*_{lm}\sin\theta\,\mathrm{d}\theta\,\mathrm{d}\phi. \tag{B.19}$$

Explicitly, the external flow in eq. (B.12) is now described by the following terms. The term proportional to ω becomes

$$i\omega m \frac{2l(l+1)}{2l^2+2l-1} u_{lm}, \tag{B.20}$$

the zeroth-order elongational term is

$$-is\frac{24}{11}\sqrt{\frac{2\pi}{15}}\delta_{l,2}(\delta_{m,2}-\delta_{m,-2}), \tag{B.21}$$

and the three first-order correction terms proportional to the strain rate are

$$\begin{aligned} &-2is\sqrt{\frac{2\pi}{15}}(-1)^m\left(\frac{2l(l+1)+m-4}{2l^2+2l-1}\right)\times \\ &\times\sum_{l',m'}\sqrt{\frac{5(2l+1)(2l'+1)}{4\pi}}\begin{pmatrix} l & l' & 2\\ 0 & 0 & 0\end{pmatrix}\left[\begin{pmatrix} l & l' & 2\\ -m & m' & 2\end{pmatrix}-\begin{pmatrix} l & l' & 2\\ -m & m' & -2\end{pmatrix}\right] \end{aligned} \tag{B.22}$$

where the brackets are the Wigner $3j$-symbols and $\times$ is the regular multiplication,

$$\begin{aligned} &-\frac{(-1)^m is}{4(2l^2+2l-1)}\sum_{l',m'} m' u_{l'm'}(\delta_{m',m-2}+\delta_{m',m+2})\times \\ &\times\sqrt{(2l+1)(2l'+1)\frac{(l+m)!(l'-m')!}{(l-m)!(l'+m')!}}\int_{-1}^{1} P_l^{-m}(x)P_{l'}^{m'}(x)\,\mathrm{d}x, \end{aligned} \tag{B.23}$$

and

$$\begin{aligned} &-\frac{(-1)^m is}{4(2l^2+2l-1)}\sum_{l',m'} u_{l'm'}(\delta_{m',m-2}-\delta_{m',m+2})\times \\ &\times\sqrt{(2l+1)(2l'+1)\frac{(l+m)!(l'-m')!}{(l-m)!(l'+m')!}}\times \\ &\times\left[(2-m)\int_{-1}^{1} P_l^{-m}(x)P_{l'}^{m'}(x)\,\mathrm{d}x+\int_{-1}^{1} P_l^{-m+1}(x)P_{l'}^{m'}(x)x\sqrt{1-x^2}\,\mathrm{d}x\right] \end{aligned} \tag{B.24}$$

where the associated Legendre polynomials p_l^m are defined in eq. (A.7). The integrals can be evaluated with Mathematica. One interesting property of these correction terms is that they couple the mode (l,m) with the modes $(l\pm2, m\pm2)$. In particular, even modes are not coupled with odd modes, which explains the difference in dynamics between k^*_{even} and k^*_{odd} observed in chapter 6.

C. Numerical methods

In chapters 4, 5, and 6 we simulate Langevin equations with additive noise. To that effect, we use a simple Euler-Maruyama method as described in [259] that we integrate with C/C++ or Octave. A stochastic differential equation of the form

$$\frac{\partial x}{\partial t} = f(x,t) + \zeta(t), \tag{C.1}$$

where f is the total force and ζ a Gaussian white noise, is integrated along a discrete trajectory $\{x_i\}_{i\geq 0}$ of time-step $\Delta t = t_{i+1} - t_i$ according to

$$x_{i+1} = x_i + \Delta t \left(f(x_i, t_i) + \frac{1}{\sqrt{\Delta t}} \zeta_i \right) \tag{C.2}$$

where ζ_i is a normally distributed random number and the pre-factor $1/\sqrt{\Delta t}$ is needed to recover the diffusion law $\langle x^2(t)\rangle = 2Dt$ for $f = 0$. The time-step must be small enough for the deterministic dynamics to converge to a unique solution under given initial conditions, and for the stochastic dynamics to yield the correct statistical properties of the Brownian motion.

In chapter 4, the different trajectories shown were obtained by integrating eqs. (4.20) and (4.21) with thermal noise as described above with the initial conditions $\theta = \phi = 0$. The stochastic phase diagram of fig. 4.6 and the probability distributions of fig. 4.7 were constructed by solving the Fokker-Planck equation (4.27) in the stationary state. This was done numerically with Octave through a Fourier decomposition.

In chapter 5, the forces coming from the third-order expansion of the bending energy (5.7) were calculated exactly with Mathematica, as were the flow correction terms in chapter 6. The spring constant K_A of eq. (5.14) was chosen such that the area constraint to third-order (5.5) was obeyed to a precision of at least 1 %. Moreover, the complex noise (5.9) was decomposed in real and imaginary parts as

$$\zeta_{lm} = (\chi_{lm} + i\xi_{lm})/\sqrt{2} \tag{C.3}$$

where χ_{lm} and ξ_{lm} are real Gaussian white noise obeying

$$\langle \chi_{lm}(t)\chi_{l'm'}(t')\rangle = \delta_{l,l'}\delta(t-t')[\delta_{m,m'} + (-1)^m \delta_{m,-m'}] \tag{C.4}$$

$$\langle \xi_{lm}(t)\xi_{l'm'}(t')\rangle = \delta_{l,l'}\delta(t-t')[\delta_{m,m'} - (-1)^m \delta_{m,-m'}]. \tag{C.5}$$

The initial conditions were such that the u_{lm} had their equilibrium mean amplitude given in [25]. We simulated long enough trajectories so that initial transient effects would vanish, which was particularly important in the deterministic case.

D. Two-dimensional vesicles

Chapters 5 and 6 deal with three-dimensional quasi-spherical vesicles. In this appendix, we present briefly similar results for two-dimensional quasi-circular vesicles. In particular, the TR regime exists in two dimensions too, even though there is no deterministic VB. The model is based on Ref. [62] in which detailed calculations can be found.

Geometry In two dimensions, the area $A_{2\mathrm{D}}$ and contour length $L_{2\mathrm{D}}$ of the vesicle are constant. We define the effective radius $R_{2\mathrm{D}} \equiv \sqrt{A_{2\mathrm{D}}/\pi}$ of a circle with the same area. The length of the vesicle can then be expressed as

$$L_{2\mathrm{D}} \equiv (2\pi + \Delta_{2\mathrm{D}})R_{2\mathrm{D}}, \tag{D.1}$$

where Δ_L is the normalized excess length of the vesicle. We expand the vesicle radius $\mathbf{R}_{2\mathrm{D}}$ in Fourier modes as

$$\mathbf{R}_{2\mathrm{D}}(\phi) = R_{2\mathrm{D}}(1 + a(\phi))\mathbf{e}_{\mathbf{r}} \tag{D.2}$$

with

$$a(\phi) \equiv \sum_{m=-\infty}^{\infty} a_m \frac{e^{im\phi}}{\sqrt{2\pi}} \tag{D.3}$$

and $a_m^* = a_{-m}$. This expansion is only valid if $\mathbf{r}(\phi)$ is a single-valued function, that it for quasi-circular vesicles, i.e., small excess lengths $\Delta_{2\mathrm{D}}$. The area of the vesicle is given by

$$A_{2\mathrm{D}} = \int_0^{2\pi} \frac{r^2(\phi)}{2}\,\mathrm{d}\phi = \pi R_{2\mathrm{D}}^2 + \frac{R_{2\mathrm{D}}^2}{2}\int_0^{2\pi}(2a(\phi) + a^2(\phi) + O(a^4))\,\mathrm{d}\phi. \tag{D.4}$$

Like the volume in three dimensions, the area is here conserved, which implies

$$a_0 = -\frac{1}{\sqrt{8\pi}}\sum_{m\neq 0}|a_m|^2 + O(a^4). \tag{D.5}$$

The length of the vesicle is given by

$$L_{2\mathrm{D}} = \int_0^{2\pi}\sqrt{r^2(\phi) + \left(\frac{\mathrm{d}r}{\mathrm{d}\phi}\right)^2}\,\mathrm{d}\phi = R_0\int_0^{2\pi}(1 + a + \frac{a'^2}{2} - \frac{aa'^2}{2} + O(a^4))\,\mathrm{d}\phi \tag{D.6}$$

so that the excess length reads

$$\Delta_{2\mathrm{D}} = \frac{1}{2}\sum_{m\neq 0}\left[(m^2-1)|a_m|^2 + \frac{a_{-m}}{\sqrt{2\pi}}\sum_{n=-m}^{m} n(m-n)a_n a_{m-n}\right] + O(a^4) \quad \text{(D.7)}$$

where we already inserted (D.5).

The bending energy reads

$$\mathcal{H}_{2\mathrm{D}} = \frac{\kappa_{2\mathrm{D}}}{2R_{2\mathrm{D}}}\int_0^{2\pi}\left(k^2(\phi) + \frac{\sigma}{R_{2\mathrm{D}}^2}\right)(r^2+r'^2)^{1/2}\,\mathrm{d}\phi. \quad \text{(D.8)}$$

where the curvature is given by

$$k(\phi) = \frac{r^2+2r'^2-rr''}{(r^2+r'^2)^{3/2}}. \quad \text{(D.9)}$$

To third-order in a, this bending energy reads

$$\begin{aligned}\mathcal{H}_{2\mathrm{D}} = \frac{\kappa_{2\mathrm{D}}}{R_{2\mathrm{D}}}\Bigg[&\pi + \sum_{m>0}(m^2-1)(m^2-3/2+\sigma_0)a_m a_{-m} \\ &+\frac{1}{\sqrt{2\pi}}\sum_{m>0}\sum_{n=-m}^{m} f^{\sigma}(m,n)\mathrm{Re}(a_{-m}a_n a_{m-n})\Bigg]\end{aligned} \quad \text{(D.10)}$$

where

$$f^{\sigma}(m,n) = -1 + 6m^2 - 3n^2(n-m)^2 + n(m-n)(9/2+m^2+\sigma_0). \quad \text{(D.11)}$$

and σ_0 is the homogeneous surface tension.

Dynamics Adapting the solution of [62][1] to a general flow of the form (3.1), we obtain the equations of motion

$$\partial_t a_m = i\omega m a_m - \Gamma_m \frac{\partial \mathcal{H}_{2\mathrm{D}}{}^{(3)}}{\partial a_{-m}} - is\frac{\sqrt{2\pi}}{4}(\delta_{m,2}-\delta_{m,-2}) + \zeta_m(t) \quad \text{(D.12)}$$

with the mobility

$$\Gamma_m = \frac{1}{\eta_o R_{2\mathrm{D}}^3}\frac{|m|}{2(\lambda+1)(m^2-1)} \quad \text{(D.13)}$$

[1] There are some small mistakes in eq. (25) of Ref. [62]: the first term should have a negative sign; the second term should have R_0^4 instead of R_0^3; the prefactor in the third term should read $D_m = 2m^2/(\lambda+1)(|m|+1)$.

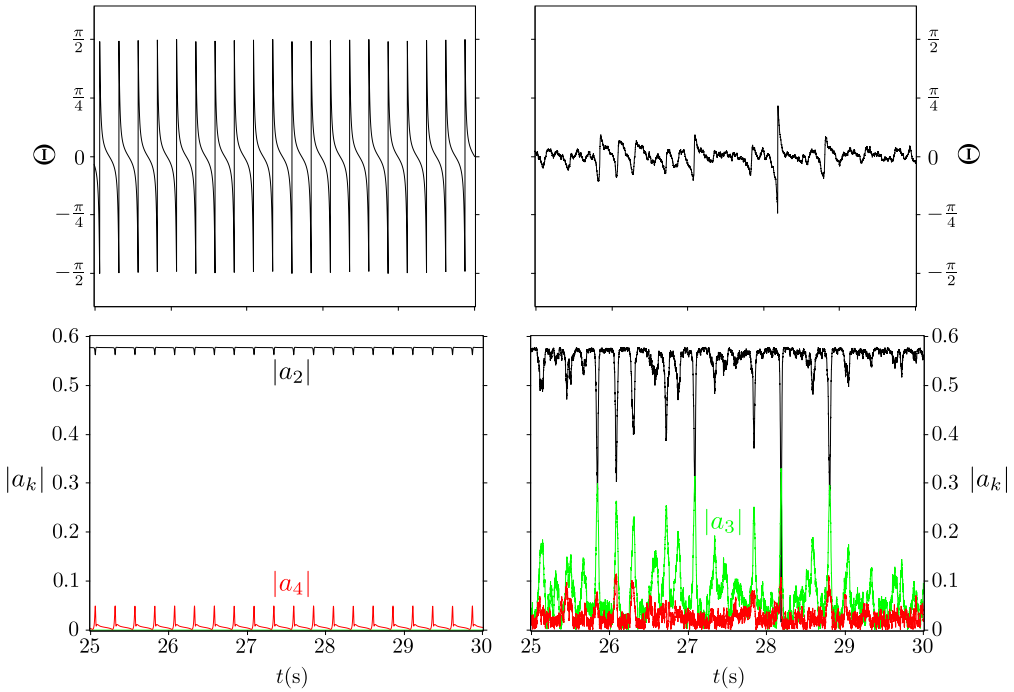

Figure D.1.: Top: Evolution of the orientation angle Θ of the vesicle without (left) and with (right) thermal fluctuations. Bottom: Corresponding evolution of the harmonic amplitudes $|u_2|$, $|u_3|$, and $|u_4|$. These trajectories were obtained for $\Delta_{2D} = 0.3$, $\Lambda_{2D} = 45$, and $S_{2D} = 50$.

and the Gaussian white noise ζ_m obeying

$$\langle \zeta_m(t) \rangle = 0 \qquad \langle \zeta_m(t)\zeta_{m'}(t') \rangle = 2k_B T \Gamma_m \delta_{m,-m'} \delta(t-t'). \tag{D.14}$$

Eqs. (D.12) have a similar structure to the three-dimensional Eqs. (5.10). We may thus expect a similar phenomenology. However, in the deterministic case eqs. (D.12) predict TT and TB dynamics, but no VB. This discrepancy is due to the fact that in three dimensions $\mathcal{Y}_{20}$, $\mathcal{Y}_{21}$, and $\mathcal{Y}_{22}$ have the same bending energy to lowest order. Then, the periodic transfer of excess area between the u_{2m} is an energetically stable. On the contrary, a_2 is always the mode with lowest energy in two dimensions, therefore no VB can take place[2].

If we now include thermal fluctuations, the picture changes dramatically. A TR regime appears at the TT-TB transition for large enough s as shown in fig. D.1. The trajectories shown there were obtained by simulating (D.12) for $m = 2, 3, 4$

[2]Note that if we artificially give the same bending energy as a_2 to a higher-order mode, e.g. a_3, then VB dynamics can be observed.

with the parameters $\Delta_{2D} = 0.3$, $\Lambda_{2D} = 45$, and $S_{2D} = 45$ with

$$\Lambda_{2D} \equiv \frac{\eta_o R_{2D}^4}{\kappa_{2D}} \omega \qquad\qquad S_{2D} \equiv \frac{\eta_o R_{2D}^4}{\kappa_{2D}} \frac{\sqrt{2\pi}}{4} s. \tag{D.15}$$

In the deterministic case (left), the predicted motion is TB: the orientation angle Θ undergoes full rotations while the shape remains ellipsoidal, i.e. dominated by u_2. The fourth mode u_4 is correlated with the second one since they are coupled by the bending energy (D.10). The amplitude $|u_3|$ of the third mode has already decayed to 0. With thermal noise, the motion becomes TR: Θ oscillates irregularly around 0 while strong shape deformations happen. In particular, $|u_3|$ becomes regularly the dominant mode during compression phases at negative oscillation angles. This mechanism of amplification of thermal fluctuations is therefore enough to create a TR regime out of a deterministic TB motion. Moreover, at large flow rates, wrinkles are also observed if higher-order harmonics are included.

The two-dimensional model thus shows almost the same phenomenology as the three-dimensional one. However, it does not agree quantitatively with experiments because three-dimensional deformations are important there. In particular, the length and surface area of the vesicle cross-section in the flow plane are not necessarily constant in three dimensions. Nevertheless, this two-dimensional model could describe ring polymers in linear flow which also exhibit TT and TB motions [231].

Bibliography

[1] M. L. Ellsworth and R. S. Sprague. Regulation of blood flow distribution in skeletal muscle: role of erythrocyte-released ATP. *J. Physiol.*, 590:4985, 2012.

[2] J. Wan, W. D. Ristenpart, and H. A. Stone. Dynamics of shear-induced ATP release from red blood cells. *Proc. Natl. Acad. Sci. U. S. A.*, 105:16432, 2008.

[3] M. Haw. *Middle World: The Restless Heart of Matter and Life*. Macmillan, 2007.

[4] E. Brézin and S. Balibar, editors. *Demain la Physique*, chapter 7 - La matière molle, page 183. Odile Jacob, 2009.

[5] P.-G. de Gennes. Soft Matter (Nobel Lecture). *Angew. Chem. Int. Ed.*, 31:842, 1992.

[6] R. Brown. XXVII. A brief account of microscopical observations made in the months of June, July and August 1827, on the particles contained in the pollen of plants; and on the general existence of active molecules in organic and inorganic bodies. *Philosophical Magazine Series 2*, 4:161, 1828.

[7] A. Einstein. Über die von der molekularkinetischen Theorie der Wärme geforderte Bewegung von in ruhenden Flüssigkeiten suspendierten Teilchen. *Ann. Phys.*, 17:549, 1905.

[8] M. von Smoluchowski. Zur kinetischen Theorie der Brownschen Molekularbewegung und der Suspensionen. *Ann. Phys.*, 326:756, 1906.

[9] M. P. Langevin. Sur la théorie du mouvement brownien. *C. R. Acad. Sci. Paris*, 146:530, 1908.

[10] J. Perrin. Mouvement brownien et réalité moléculaire. *Annales de Chimie et de Physique*, 18:5, 1909.

[11] J. K. G. Dhont. *An Introduction to Dynamics of Colloids*. Elsevier, 1996.

[12] M. Doi and S. F. Edwards. *The theory of polymer dynamics*. Clarendon Press, Oxford, 1988.

[13] S. A. Safran. *Statistical Thermodynamics of Surfaces, Interfaces, and Membranes*. Perseus Books, 1994.

[14] D. Nelson, T. Piran, and S. Weinberg, editors. *Statistical Mechanics of Membrames and Surfaces (2nd edition)*. World Scientific, 2004.

[15] P. L. Luisi, P. Walde, and T. Oberholzer. Lipid vesicles as possible intermediates in the origin of life. *Curr. Opin. Colloid Interface Sci.*, 4:33, 1999.

[16] The 2013 Nobel Prize in Physiology or Medicine - Advanced Information. *Nobelprize.org*. Nobel Media AB 2013. Web, 13 Mar 2014.

[17] D. Scanlan. Bacterial vesicles in the ocean. *Science*, 343:143, 2014.

[18] V. P. Torchilin. Recent advances with liposomes as pharmaceutical carriers. *Nat. Rev. Drug Discov.*, 4:145, 2005.

[19] P. Walde, K. Cosentino, H. Engel, and P. Stano. Giant vesicles: Preparations and applications. *ChemBioChem*, 11:848, 2010.

[20] P.B. Canham. The minimum energy of bending as a possible explanation of the biconcave shape of the human red blood cell. *J. Theor. Biol.*, 26:61, 1970.

[21] W. Helfrich. Elastic properties of lipid bilayers - theory and possible experiments. *Z. Naturf. C*, 28:693, 1973.

[22] E. A. Evans. Bending resistance and chemically induced moments in membrane bilayers. *Biophys. J.*, 14:923, 1974.

[23] M. P. Sheetz and S. J. Singer. Biological membranes as bilayer couples. A molecular mechanism of drug-erythrocyte interactions. *Proc. Natl. Acad. Sci. U. S. A.*, 71:4457, 1974.

[24] S. Svetina and B. Žekš. Membrane bending energy and shape determination of phospholipid vesicles and red blood cells. *Eur. Biophys. J.*, 17:101, 1989.

[25] U. Seifert. Configurations of fluid membranes and vesicles. *Adv. Phys.*, 46:13, 1997.

[26] G. Lim H. W., M. Wortis, and R. Mukhopadhyay. Stomatocyte-discocyte-echinocyte sequence of the human red blood cell: Evidence for the bilayer-couple hypothesis from membrane mechanics. *Proc. Natl. Acad. Sci. U. S. A.*, 99:16766, 2002.

[27] E. M. Purcell. Life at low Reynolds number. *Am. J. Phys.*, 45:3, 1977.

[28] J. Happel and H. Brenner. *Low Reynolds number hydrodynamics*. Martinus Nijhoff Publishers, 1983.

[29] C. Pozrikidis. *Boundary Integral and Singularity Methods for Linearized Viscous Flow*. Cambridge University Press, 1992.

[30] S. Kim and S. J. Karrila. *Microhydrodynamics*. Dover, 2005.

[31] H. Lamb. *Hydrodynamics*. Cambridge University Press, 1932.

[32] C. W. Gardiner. *Handbook of Stochastic Methods*. Springer-Verlag, Berlin, 3rd edition, 2004.

[33] H. Risken. *The Fokker-Planck Equation*. Springer-Verlag, Berlin, 2nd edition, 1989.

[34] U. Seifert. Stochastic thermodynamics, fluctuation theorems and molecular machines. *Rep. Prog. Phys.*, 75:126001, 2012.

[35] R.E. Waugh. Surface viscosity measurements from large bilayer vesicle tether formation. II. Experiments. *Biophys. J.*, 28:29, 1982.

[36] W. Rawicz, K.C. Olbrich, T. McIntosh, D. Needham, and E. Evans. Effect of chain length and unsaturation on elasticity of lipid bilayers. *Biophys. J.*, 79:328, 2000.

[37] R. Dimova, S. Aranda, N. Bezlyepkina, V. Nikolov, K. A. Riske, and R. Lipowsky. A practical guide to giant vesicles. Probing the membrane nanoregime via optical microscopy. *J. Phys.: Condens. Matter*, 18:S1151, 2006.

[38] E. P. Petrov, R. Petrosyan, and P. Schwille. Translational and rotational diffusion of micrometer-sized solid domains in lipid membranes. *Soft Matter*, 8:7552, 2012.

[39] F. G. Woodhouse and R. E. Goldstein. Shear-driven circulation patterns in lipid

membrane vesicles. *J. Fluid Mech.*, 705:165, 2012.

[40] A. R. Honerkamp-Smith, F. G. Woodhouse, V. Kantsler, and R. E. Goldstein. Membrane viscosity determined from shear-driven flow in giant vesicles. *Phys. Rev. Lett.*, 111:038103, 2013.

[41] U. Seifert. Fluid membranes in hydrodynamic flow fields: Formalism and an application to fluctuating quasispherical vesicles in shear flow. *Eur. Phys. J. B*, 8:405, 1999.

[42] T. R. Powers. Dynamics of filaments and membranes in a viscous fluid. *Rev. Mod. Phys.*, 82:1607, 2010.

[43] J. Genova, V. Vitkova, and I. Bivas. Registration and analysis of the shape fluctuations of nearly spherical lipid vesicles. *Phys. Rev. E*, 88:022707, 2013.

[44] D. Abreu, M. Levant, V. Steinberg, and U. Seifert. Fluid Vesicles in Flow. *Adv. Colloid Interface Sci.*, 208:129, 2014.

[45] S. R. Keller and R. Skalak. Motion of a tank-treading ellipsoidal particle in a shear flow. *J. Fluid Mech.*, 120:27, 1982.

[46] T. W. Secomb and R. Skalak. Surface flow of viscoelastic membranes in viscous fluids. *Q. J. Mechanics Appl. Math.*, 35:233, 1982.

[47] F. Rioual, T. Biben, and C. Misbah. Analytical analysis of a vesicle tumbling under a shear flow. *Phys. Rev. E*, 69:061914, 2004.

[48] H. Noguchi and G. Gompper. Dynamics of fluid vesicles in shear flow: Effect of membrane viscosity and thermal fluctuations. *Phys. Rev. E*, 72:011901, 2005.

[49] M.-A. Mader, H. Ez-Zahraouy, C. Misbah, and T. Podgorski. On coupling between the orientation and the shape of a vesicle under a shear flow. *Eur. Phys. J. E*, 22:275, 2007.

[50] H. Noguchi and G. Gompper. Swinging and tumbling of fluid vesicles in shear flow. *Phys. Rev. Lett.*, 98:128103, 2007.

[51] D. Abreu and U. Seifert. Effect of thermal noise on vesicles and capsules in shear flow. *Phys. Rev. E*, 86:010902, 2012.

[52] F. Youhei. Small deformation of a liposome in a linear shear flow. *Fluid Dyn. Res.*, 15:1, 1995.

[53] P. Olla. The role of tank-treading motions in the transverse migration of a spheroidal vesicle in a shear flow. *J. Phys. A: Math. Gen.*, 30:317, 1997.

[54] S. B. Rochal, V. L. Lorman, and G. Mennessier. Viscoelastic dynamics of spherical composite vesicles. *Phys. Rev. E*, 71:021905, 2005.

[55] C. Misbah. Vacillating breathing and tumbling of vesicles under shear flow. *Phys. Rev. Lett.*, 96:028104, 2006.

[56] V. V. Lebedev, K. S. Turitsyn, and S. S. Vergeles. Dynamics of nearly spherical vesicles in an external flow. *Phys. Rev. Lett.*, 99:218101, 2007.

[57] P. M. Vlahovska and R. S. Gracia. Dynamics of a viscous vesicle in linear flows. *Phys. Rev. E*, 75:016313, 2007.

[58] D. Abreu and U. Seifert. Noisy nonlinear dynamics of vesicles in flow. *Phys. Rev. Lett.*, 110:238103, 2013.

[59] G. Danker and C. Misbah. Rheology of a dilute suspension of vesicles. *Phys. Rev.*

Lett., 98:088104, 2007.

[60] A. Farutin, T. Biben, and C. Misbah. Analytical progress in the theory of vesicles under linear flow. *Phys. Rev. E*, 81:061904, 2010.

[61] G. Frenkel and M. Schwartz. Shape fluctuations of a deformable body in a randomly stirred host fluid. *Phys. Rev. E*, 68:061202, 2003.

[62] R. Finken, A. Lamura, U. Seifert, and G. Gompper. Two-dimensional fluctuating vesicles in linear shear flow. *Eur. Phys. J. E*, 25:309, 2008.

[63] K. S. Turitsyn and S. S. Vergeles. Wrinkling of vesicles during transient dynamics in elongational flow. *Phys. Rev. Lett.*, 100:028103, 2008.

[64] S. Meßlinger, B. Schmidt, H. Noguchi, and G. Gompper. Dynamical regimes and hydrodynamic lift of viscous vesicles under shear. *Phys. Rev. E*, 80:011901, 2009.

[65] H. Noguchi. Dynamical modes of deformed red blood cells and lipid vesicles in flows. *Prog. Theor. Phys. Supplement*, 184:364, 2010.

[66] X. Li, P. M. Vlahovska, and G. E. Karniadakis. Continuum- and particle-based modeling of shapes and dynamics of red blood cells in health and disease. *Soft Matter*, 9:28, 2013.

[67] M. Kraus, W. Wintz, U. Seifert, and R. Lipowsky. Fluid vesicles in shear flow. *Phys. Rev. Lett.*, 77:3685, 1996.

[68] I. Cantat and C. Misbah. Lift force and dynamical unbinding of adhering vesicles under shear flow. *Phys. Rev. Lett.*, 83:880, 1999.

[69] I. Cantat and C. Misbah. Dynamics and similarity laws for adhering vesicles in haptotaxis. *Phys. Rev. Lett.*, 83:235, 1999.

[70] S. Sukumaran and U. Seifert. Influence of shear flow on vesicles near a wall: A numerical study. *Phys. Rev. E*, 64:011916, 2001.

[71] B. Kaoui, G. H. Ristow, I. Cantat, C. Misbah, and W. Zimmermann. Lateral migration of a two-dimensional vesicle in unbounded Poiseuille flow. *Phys. Rev. E*, 77:021903, 2008.

[72] G. Coupier, B. Kaoui, T. Podgorski, and C. Misbah. Noninertial lateral migration of vesicles in bounded Poiseuille flow. *Phys. Fluids*, 20:111702, 2008.

[73] S. K. Veerapaneni, D. Gueyffier, G. Biros, and D. Zorin. A numerical method for simulating the dynamics of 3D axisymmetric vesicles suspended in viscous flows. *J. Comput. Phys.*, 228:7233, 2009.

[74] T. Biben, A. Farutin, and C. Misbah. Three-dimensional vesicles under shear flow: Numerical study of dynamics and phase diagram. *Phys. Rev. E*, 83:031921, 2011.

[75] G. Boedec, M. Leonetti, and M. Jaeger. 3D vesicle dynamics simulations with a linearly triangulated surface. *J. Comput. Phys.*, 230:1020, 2011.

[76] B. Kaoui, N. Tahiri, T. Biben, H. Ez-Zahraouy, A. Benyoussef, G. Biros, and C. Misbah. Complexity of vesicle microcirculation. *Phys. Rev. E*, 84:041906, 2011.

[77] S. V. Veerapaneni, Y.-N. Young, P. M. Vlahovska, and J. Bławzdziewicz. Dynamics of a compound vesicle in shear flow. *Phys. Rev. Lett.*, 106:158103, 2011.

[78] H. Zhao and E. S. G. Shaqfeh. The dynamics of a vesicle in simple shear flow. *J. Fluid Mech.*, 674:578, 2011.

[79] H. Zhao, A. P. Spann, and E. S. G. Shaqfeh. The dynamics of a vesicle in a

wall-bound shear flow. *Phys. Fluids*, 23:121901, 2011.

[80] A. Farutin, O. Aouane, and C. Misbah. Vesicle dynamics under weak flows: Application to large excess area. *Phys. Rev. E*, 85:061922, 2012.

[81] A. Farutin and C. Misbah. Squaring, parity breaking, and S tumbling of vesicles under shear flow. *Phys. Rev. Lett.*, 109:248106, 2012.

[82] A. Farutin and C. Misbah. Analytical and numerical study of three main migration laws for vesicles under flow. *Phys. Rev. Lett.*, 110:108104, 2013.

[83] K. Liu and S. Li. Nonlinear simulations of vesicle wrinkling. *Math. Meth. Appl. Sci.*, Early View, 2013 (DOI: 10.1002/mma.2867).

[84] H. Zhao and E. S. G. Shaqfeh. The shape stability of a lipid vesicle in a uniaxial extensional flow. *J. Fluid Mech.*, 719:345, 2013.

[85] P. Dimitrakopoulos. Interfacial dynamics in stokes flow via a three-dimensional fully-implicit interfacial spectral boundary element algorithm. *J. Comput. Phys.*, 225:408, 2007.

[86] S. Kessler, R. Finken, and U. Seifert. Swinging and tumbling of elastic capsules in shear flow. *J. Fluid Mech.*, 605:207, 2008.

[87] H. Zhao, A. H. G. Isfahani, L. N. Olson, and J. B. Freund. A spectral boundary integral method for flowing blood cells. *J. Comput. Phys.*, 229:3726, 2010.

[88] C. S. Peskin. The immersed boundary method. *Acta Num.*, 11:479, 2002.

[89] S. Takagi, T. Yamada, X. Gong, and Y. Matsumoto. The deformation of a vesicle in a linear shear flow. *J. Appl. Mech.*, 76:021207, 2009.

[90] Y. Kim and M.-C. Lai. Simulating the dynamics of inextensible vesicles by the penalty immersed boundary method. *J. Comput. Phys.*, 229:4840, 2010.

[91] Y. Kim and M.-C. Lai. Numerical study of viscosity and inertial effects on tank-treading and tumbling motions of vesicles under shear flow. *Phys. Rev. E*, 86:066321, 2012.

[92] T. Biben and C. Misbah. Tumbling of vesicles under shear flow within an advected-field approach. *Phys. Rev. E*, 67:031908, 2003.

[93] J. Beaucourt, F. Rioual, T. Séon, T. Biben, and C. Misbah. Steady to unsteady dynamics of a vesicle in a flow. *Phys. Rev. E*, 69:011906, 2004.

[94] T. Biben, K. Kassner, and C. Misbah. Phase-field approach to three-dimensional vesicle dynamics. *Phys. Rev. E*, 72:041921, 2005.

[95] A. Laadhari, P. Saramito, and C. Misbah. Vesicle tumbling inhibited by inertia. *Phys. Fluids*, 24:031901, 2012.

[96] D. Salac and M. J. Miksis. Reynolds number effects on lipid vesicles. *J. Fluid Mech.*, 711:122, 2012.

[97] V. Doyeux, Y. Guyot, V. Chabannes, C. Prud'homme, and M. Ismail. Simulation of two-fluid flows using a finite element/level set method. Application to bubbles and vesicle dynamics. *J. Comput. Appl. Math.*, 246:251, 2013.

[98] A. Yazdani and P. Bagchi. Three-dimensional numerical simulation of vesicle dynamics using a front-tracking method. *Phys. Rev. E*, 85:056308, 2012.

[99] Z. Y. Luo, S. Q. Wang, L. He, F. Xu, and B. F. Bai. Inertia-dependent dynamics of three-dimensional vesicles and red blood cells in shear flow. *Soft Matter*, 9:9651,

2013.

[100] F. L. H. Brown. Elastic modeling of biomembranes and lipid bilayers. *Annu. Rev. Phys. Chem.*, 59:685, 2008.

[101] B. Kaoui, J. Harting, and C. Misbah. Two-dimensional vesicle dynamics under shear flow: Effect of confinement. *Phys. Rev. E*, 83:066319, 2011.

[102] B. Kaoui, T. Krüger, and J. Harting. How does confinement affect the dynamics of viscous vesicles and red blood cells? *Soft Matter*, 8:9246, 2012.

[103] B. Kaoui, T. Krüger, and J. Harting. Complex dynamics of a bilamellar vesicle as a simple model for leukocytes. *Soft Matter*, 9:8057, 2013.

[104] I. Halliday, S. V. Lishchuk, T. J. Spencer, G. Pontrelli, and C. M. Care. Multiple-component lattice Boltzmann equation for fluid-filled vesicles in flow. *Phys. Rev. E*, 87:023307, 2013.

[105] E. G. Brandt. Fluctuating hydrodynamics simulations of coarse-grained lipid membranes under steady-state conditions and in shear flow. *Phys. Rev. E*, 88:012714, 2013.

[106] T. Sugii, S. Takagi, and Y. Matsumoto. A meso-scale analysis of lipid bilayers with the dissipative particle dynamics method: Thermally fluctuating interfaces. *Int. J. Numer. Meth. Fluids*, 54:831, 2007.

[107] H. Noguchi and G. Gompper. Shape transitions of fluid vesicles and red blood cells in capillary flows. *Proc. Natl. Acad. Sci. U. S. A.*, 102:14159, 2005.

[108] H. Noguchi and G. Gompper. Vesicle dynamics in shear and capillary flows. *J. Phys.: Condens. Matter*, 17:S3439, 2005.

[109] J. L. McWhirter, H. Noguchi, and G. Gompper. Flow-induced clustering and alignment of vesicles and red blood cells in microcapillaries. *Proc. Natl. Acad. Sci. U. S. A.*, 106:6039, 2009.

[110] H. Noguchi, G. Gompper, L. Schmid, A. Wixforth, and T. Franke. Dynamics of fluid vesicles in flow through structured microchannels. *EPL*, 89:28002, 2010.

[111] A. Lamura and G. Gompper. Dynamics and rheology of vesicle suspensions in wall-bounded shear flow. *EPL*, 102:28004, 2013.

[112] D. A. Fedosov, M. Peltomaki, and G. Gompper. Deformation and dynamics of red blood cells in flow through cylindrical microchannels. *Soft Matter*, 2014 (DOI: 10.1039/C4SM00248B).

[113] M. Abkarian, C. Lartigue, and A. Viallat. Tank treading and unbinding of deformable vesicles in shear flow: Determination of the lift force. *Phys. Rev. Lett.*, 88:068103, 2002.

[114] V. Kantsler and V. Steinberg. Orientation and dynamics of a vesicle in tank-treading motion in shear flow. *Phys. Rev. Lett.*, 95:258101, 2005.

[115] B. Lorz, R. Simson, J. Nardi, and E. Sackmann. Weakly adhering vesicles in shear flow: Tanktreading and anomalous lift force. *Europhys. Lett.*, 51:468, 2000.

[116] A. Sakashita, N. Urakami, P. Ziherl, and M. Imai. Three-dimensional analysis of lipid vesicle transformations. *Soft Matter*, 8:8569, 2012.

[117] J. Deschamps, V. Kantsler, and V. Steinberg. Phase diagram of single vesicle dynamical states in shear flow. *Phys. Rev. Lett.*, 102:118105, 2009.

[118] R. Hatakenaka, S. Takagi, and Y. Matsumoto. Orientation and internal flow of a vesicle in tank-treading motion in shear flow. *Phys. Rev. E*, 84:026324, 2011.

[119] A. Razpet, G. Gomišček, V. Arrigler, S. Svetina, and B. Žekš. Rotation of giant phospholipid vesicles in an uniform shear flow. *Pflügers Archiv*, 439:r141, 2000.

[120] N. Fa, C. M. Marques, E. Mendes, and A. P. Schröder. Rheology of giant vesicles: A micropipette study. *Phys. Rev. Lett.*, 92:108103, 2004.

[121] M. Abkarian and A. Viallat. Dynamics of vesicles in a wall-bounded shear flow. *Biophys. J.*, 89:1055, 2005.

[122] V. Kantsler and V. Steinberg. Transition to tumbling and two regimes of tumbling motion of a vesicle in shear flow. *Phys. Rev. Lett.*, 96:036001, 2006.

[123] M. Mader, V. Vitkova, M. Abkarian, A. Viallat, and T. Podgorski. Dynamics of viscous vesicles in shear flow. *Eur. Phys. J. E*, 19:389, 2006.

[124] C. Vezy, G. Massiera, and A. Viallat. Adhesion induced non-planar and asynchronous flow of a giant vesicle membrane in an external shear flow. *Soft Matter*, 3:844, 2007.

[125] V. Kantsler, E. Segre, and V. Steinberg. Dynamics of interacting vesicles and rheology of vesicle suspension in shear flow. *EPL*, 82:58005, 2008.

[126] A. Pommella, S. Caserta, and S. Guido. Dynamic flow behaviour of surfactant vesicles under shear flow: role of a multilamellar microstructure. *Soft Matter*, 9:7545, 2013.

[127] V. Vitkova, M. Mader, and T. Podgorski. Deformation of vesicles flowing through capillaries. *Europhys. Lett.*, 68:398, 2004.

[128] G. Coupier, A. Farutin, C. Minetti, T. Podgorski, and C. Misbah. Shape diagram of vesicles in Poiseuille flow. *Phys. Rev. Lett.*, 108:178106, 2012.

[129] S. Braunmüller, L. Schmid, and T. Franke. Dynamics of red blood cells and vesicles in microchannels of oscillating width. *J. Phys.: Condens. Matter*, 23:184116, 2011.

[130] K. H. de Haas, C. Blom, D. van den Ende, M. H. G. Duits, and J. Mellema. Deformation of giant lipid bilayer vesicles in shear flow. *Phys. Rev. E*, 56:7132, 1997.

[131] N. Shahidzadeh, D. Bonn, O. Aguerre-Chariol, and J. Meunier. Large deformations of giant floppy vesicles in shear flow. *Phys. Rev. Lett.*, 81:4268, 1998.

[132] N. Callens, C. Minetti, G. Coupier, M.-A. Mader, F. Dubois, C. Misbah, and T. Podgorski. Hydrodynamic lift of vesicles under shear flow in microgravity. *EPL*, 83:24002, 2008.

[133] V. Kantsler, E. Segre, and V. Steinberg. Vesicle dynamics in time-dependent elongation flow: Wrinkling instability. *Phys. Rev. Lett.*, 99:178102, 2007.

[134] V. Kantsler, E. Segre, and V. Steinberg. Critical dynamics of vesicle stretching transition in elongational flow. *Phys. Rev. Lett.*, 101:048101, 2008.

[135] J. S. Lee, R. Dylla-Spears, N. P. Teclemariam, and S. J. Muller. Microfluidic four-roll mill for all flow types. *Appl. Phys. Lett.*, 90:074103, 2007.

[136] J. Deschamps, V. Kantsler, E. Segre, and V. Steinberg. Dynamics of a vesicle in general flow. *Proc. Natl. Acad. Sci. U. S. A.*, 106:11444, 2009.

[137] N. J. Zabusky, E. Segre, J. Deschamps, V. Kantsler, and V. Steinberg. Dynamics of

vesicles in shear and rotational flows: Modal dynamics and phase diagram. *Phys. Fluids*, 23:041905, 2011.

[138] M. Levant, J. Deschamps, E. Afik, and V. Steinberg. Characteristic spatial scale of vesicle pair interactions in a plane linear shear flow. *Phys. Rev. E*, 85:056306, 2012.

[139] M. Levant and V. Steinberg. Amplification of thermal noise through vesicle dynamics. *Phys. Rev. Lett.*, 109:268103, 2012.

[140] H. Schmid-Schönbein and R. Wells. Fluid drop-like transition of erythrocytes under shear. *Science*, 165:288, 1969.

[141] H. L. Goldsmith and J. Marlow. Flow behaviour of erythrocytes. I. Rotation and deformation in dilute suspensions. *Proc. R. Soc. Lond. B*, 182:351, 1972.

[142] T. M. Fischer, M. Stöhr-Lissen, and H. Schmid-Schönbein. The red cell as a fluid droplet: tank tread-like motion of the human erythrocyte membrane in shear flow. *Science*, 202:894, 1978.

[143] H. Basu, A. Dharmadhikari, J. A. Dharmadhikari, S. Sharma, and D. Mathur. Tank treading of optically trapped red blood cells in shear flow. *Biophys. J.*, 101:1604, 2011.

[144] M. Abkarian, M. Faivre, and A. Viallat. Swinging of red blood cells under shear flow. *Phys. Rev. Lett.*, 98:188302, 2007.

[145] J. M. Skotheim and T. W. Secomb. Red blood cells and other nonspherical capsules in shear flow: Oscillatory dynamics and the tank-treading-to-tumbling transition. *Phys. Rev. Lett.*, 98:078301, 2007.

[146] J. Dupire, M. Socol, and A. Viallat. Full dynamics of a red blood cell in shear flow. *Proc. Natl. Acad. Sci. U. S. A.*, 109:20808, 2012.

[147] H. Noguchi and G. Gompper. Fluid vesicles with viscous membranes in shear flow. *Phys. Rev. Lett.*, 93:258102, 2004.

[148] J. T. Schwalbe, P. M. Vlahovska, and M. J. Miksis. Monolayer slip effects on the dynamics of a lipid bilayer vesicle in a viscous flow. *J. Fluid Mech.*, 647:403, 2010.

[149] P. Olla. Tank-treading as a means of propulsion in viscous shear flows. *J. Fluid Mech.*, 680:265, 2011.

[150] G. Danker, T. Biben, T. Podgorski, C. Verdier, and C. Misbah. Dynamics and rheology of a dilute suspension of vesicles: Higher-order theory. *Phys. Rev. E*, 76:041905, 2007.

[151] V. V. Lebedev, K. S. Turitsyn, and S. S. Vergeles. Nearly spherical vesicles in an external flow. *New J. Phys.*, 10:043044, 2008.

[152] M. Guedda, M. Abaidi, M. Benlahsen, and C. Misbah. Dynamic modes of quasi-spherical vesicles: Exact analytical solutions. *Phys. Rev. E*, 86:051915, 2012.

[153] B. Kaoui, A. Farutin, and C. Misbah. Vesicles under simple shear flow: Elucidating the role of relevant control parameters. *Phys. Rev. E*, 80:061905, 2009.

[154] M. Levant, D. Abreu, U. Seifert, and V. Steinberg. Wrinkling instability of vesicles in steady linear flow. *submitted*, 2014.

[155] P. Marmottant, T. Biben, and S. Hilgenfeldt. Deformation and rupture of lipid vesicles in the strong shear flow generated by ultrasound-driven microbubbles.

Proc. R. Soc. Lond. A, 464:1781, 2008.

[156] T. T. Perkins, D. E. Smith, and S. Chu. Single polymer dynamics in an elongational flow. *Science*, 276:2016, 1997.

[157] R. Bar-Ziv and E. Moses. Instability and "pearling" states produced in tubular membranes by competition of curvature and tension. *Phys. Rev. Lett.*, 73:1392, 1994.

[158] P. Nelson, T. Powers, and U. Seifert. Dynamical theory of the pearling instability in cylindrical vesicles. *Phys. Rev. Lett.*, 74:3384, 1995.

[159] S. Gerashchenko and V. Steinberg. Critical slowing down in polymer dynamics near the coil-stretch transition in elongation flow. *Phys. Rev. E*, 78:040801, 2008.

[160] S. Sowinski, C. Jolly, O. Berninghausen, M. A. Purbhoo, A. Chauveau, K. Köhler, S. Oddos, P. Eissmann, F. M. Brodsky, C. Hopkins, B. Önfelt, Q. Sattentau, and D. M. Davis. Membrane nanotubes physically connect T cells over long distances presenting a novel route for HIV-1 transmission. *Nat. Cell Biol.*, 10:211, 2008.

[161] R. Finken and U. Seifert. Wrinkling of microcapsules in shear flow. *J. Phys.: Condens. Matter*, 18:L185, 2006.

[162] P. M. Vlahovska, D. Barthes-Biesel, and C. Misbah. Flow dynamics of red blood cells and their biomimetic counterparts. *C. R. Phys.*, 14:451, 2013.

[163] U. Seifert. Hydrodynamic lift on bound vesicles. *Phys. Rev. Lett.*, 83:876, 1999.

[164] S. Chatkaew, M. Georgelin, M. Jaeger, and M. Leonetti. Dynamics of vesicle unbinding under axisymmetric flow. *Phys. Rev. Lett.*, 103:248103, 2009.

[165] P. Olla. The lift on a tank-treading ellipsoidal cell in a shear flow. *J. Phys. II France*, 7:1533, 1997.

[166] P. Olla. Simplified model for red cell dynamics in small blood vessels. *Phys. Rev. Lett.*, 82:453, 1999.

[167] T. M. Geislinger and T. Franke. Hydrodynamic lift of vesicles and red blood cells in flow – from Fåhræus and Lindqvist to microfluidic cell sorting. *Adv. Colloid Interface Sci.*, 2014 (DOI: 10.1016/j.cis.2014.03.002).

[168] P. Olla. The behavior of closed inextensible membranes in linear and quadratic shear flows. *Physica A*, 278:87, 2000.

[169] X. Grandchamp, G. Coupier, A. Srivastav, C. Minetti, and T. Podgorski. Lift and down-gradient shear-induced diffusion in red blood cell suspensions. *Phys. Rev. Lett.*, 110:108101, 2013.

[170] B. Kaoui, G. Biros, and C. Misbah. Why do red blood cells have asymmetric shapes even in a symmetric flow? *Phys. Rev. Lett.*, 103:188101, 2009.

[171] G. Danker, P. M. Vlahovska, and C. Misbah. Vesicles in Poiseuille flow. *Phys. Rev. Lett.*, 102:148102, 2009.

[172] G. Ghigliotti, A. Rahimian, G. Biros, and C. Misbah. Vesicle migration and spatial organization driven by flow line curvature. *Phys. Rev. Lett.*, 106:028101, 2011.

[173] A. Farutin and C. Misbah. Symmetry breaking of vesicle shapes in Poiseuille flow. *Phys. Rev. E*, 84:011902, 2011.

[174] J. L. McWhirter, H. Noguchi, and G. Gompper. Deformation and clustering of red blood cells in microcapillary flows. *Soft Matter*, 7:10967, 2011.

[175] R. Bruinsma. Rheology and shape transitions of vesicles under capillary flow. *Physica A*, 234:249, 1996.

[176] S.S. Vergeles. Rheological properties of a vesicle suspension. *JETP Lett.*, 87:511, 2008.

[177] A. Rahimian, S. K. Veerapaneni, and G. Biros. Dynamic simulation of locally inextensible vesicles suspended in an arbitrary two-dimensional domain, a boundary integral method. *J. Comput. Phys.*, 229:6466, 2010.

[178] G. Ghigliotti, T. Biben, and C. Misbah. Rheology of a dilute two-dimensional suspension of vesicles. *J. Fluid Mech.*, 653:489, 2010.

[179] M. Thiébaud and C. Misbah. Rheology of a vesicle suspension with finite concentration: A numerical study. *Phys. Rev. E*, 88:062707, 2013.

[180] H. Zhao and E. S. G. Shaqfeh. The dynamics of a non-dilute vesicle suspension in a simple shear flow. *J. Fluid Mech.*, 725:709, 2013.

[181] V. Vitkova, M.-A. Mader, B. Polack, C. Misbah, and T. Podgorski. Micro-macro link in rheology of erythrocyte and vesicle suspensions. *Biophys. J.*, 95:L33, 2008.

[182] A. Ramachandran and G. Leal. A scaling theory for the hydrodynamic interaction between a pair of vesicles or capsules. *Phys. Fluids*, 22:091702, 2010.

[183] D.-H. Le and K.-H. Chiam. Hydrodynamic interaction between two nonspherical capsules in shear flow. *Phys. Rev. E*, 84:056322, 2011.

[184] P. Y. Gires, G. Danker, and C. Misbah. Hydrodynamic interaction between two vesicles in a linear shear flow: Asymptotic study. *Phys. Rev. E*, 86:011408, 2012.

[185] P.-Y. Gires, A. Srivastav, C. Misbah, T. Podgorski, and G. Coupier. Pairwise hydrodynamic interactions and diffusion in a vesicle suspension. *Phys. Fluids*, 26:013304, 2014.

[186] J. B. Freund and M. M. Orescanin. Cellular flow in a small blood vessel. *J. Fluid Mech.*, 671:466, 2011.

[187] G. Ghigliotti, H. Selmi, L. El Asmi, and C. Misbah. Why and how does collective red blood cells motion occur in the blood microcirculation? *Phys. Fluids*, 24:101901, 2012.

[188] Giovanna Tomaiuolo, Luca Lanotte, Giovanni Ghigliotti, Chaouqi Misbah, and Stefano Guido. Red blood cell clustering in Poiseuille microcapillary flow. *Phys. Fluids*, 24:051903, 2012.

[189] J. L. McWhirter, H. Noguchi, and G. Gompper. Ordering and arrangement of deformed red blood cells in flow through microcapillaries. *New J. Phys.*, 14:085026, 2012.

[190] J.-J. Foo, V. Chan, and K.-K. Liu. Shape recovery of an optically trapped vesicle: effect of flow velocity and temperature. *IEEE Trans. Nanobiosci.*, 3:96, 2004.

[191] H. Zhou, B. B. Gabilondo, W. Losert, and W. van de Water. Stretching and relaxation of vesicles. *Phys. Rev. E*, 83:011905, 2011.

[192] O. Rossier, D. Cuvelier, N. Borghi, P. H. Puech, I. Derényi, A. Buguin, P. Nassoy, and F. Brochard-Wyart. Giant Vesicles under Flows: Extrusion and Retraction of Tubes. *Langmuir*, 19:575, 2003.

[193] T. Nakajima, K. Kon, N. Maeda, K. Tsunekawa, and T. Shiga. Deformation

response of red blood cells in oscillatory shear flow. *Am. J. Physiol. Heart Circ. Physiol.*, 259:H1071, 1990.

[194] N. Watanabe, H. Kataoka, T. Yasuda, and S. Takatani. Dynamic deformation and recovery response of red blood cells to a cyclically reversing shear flow: Effects of frequency of cyclically reversing shear flow and shear stress level. *Biophys. J.*, 91:1984, 2006.

[195] J. Dupire, M. Abkarian, and A. Viallat. Chaotic dynamics of red blood cells in a sinusoidal flow. *Phys. Rev. Lett.*, 104:168101, 2010.

[196] H. Noguchi. Dynamic modes of red blood cells in oscillatory shear flow. *Phys. Rev. E*, 81:061920, 2010.

[197] H. Noguchi. Dynamics of fluid vesicles in oscillatory shear flow. *J. Phys. Soc. Jpn.*, 79:024801, 2010.

[198] M. Zhao and P. Bagchi. Dynamics of microcapsules in oscillating shear flow. *Phys. Fluids*, 23:111901, 2011.

[199] A. Farutin and C. Misbah. Rheology of vesicle suspensions under combined steady and oscillating shear flows. *J. Fluid Mech.*, 700:362, 2012.

[200] S. Kessler, R. Finken, and U. Seifert. Elastic capsules in shear flow: Analytical solutions for constant and time-dependent shear rates. *Eur. Phys. J. E*, 29:399, 2009.

[201] M. Levant and V. Steinberg. Complex dynamics of compound vesicles in linear flow. *Phys. Rev. Lett.*, 112:138106, 2014.

[202] P. Sens. Dynamics of nonequilibrium membrane bud formation. *Phys. Rev. Lett.*, 93:108103, 2004.

[203] T. Franke, C. T. Leirer, A. Wixforth, N. Dan, and M. F. Schneider. Phase-transition- and dissipation-driven budding in lipid vesicles. *ChemPhysChem*, 10:2852, 2009.

[204] M. Rahimi and M. Arroyo. Shape dynamics, lipid hydrodynamics, and the complex viscoelasticity of bilayer membranes. *Phys. Rev. E*, 86:011932, 2012.

[205] P. Bagchi. Mesoscale simulation of blood flow in small vessels. *Biophys. J.*, 92:1858, 2007.

[206] D. A. Fedosov, W. Pan, B. Caswell, G. Gompper, and G. E. Karniadakis. Predicting human blood viscosity in silico. *Proc. Natl. Acad. Sci. U. S. A.*, 108:11772, 2011.

[207] M. H.-Y. Tan, D.-L. Le, and K.-H. Chiam. Hydrodynamic diffusion of a suspension of elastic capsules in bounded simple shear flow. *Soft Matter*, 8:2243, 2012.

[208] T. W. Secomb and A. R. Pries. Blood viscosity in microvessels: Experiment and theory. *C. R. Phys.*, 14:470, 2013.

[209] J. B. Freund. Leukocyte margination in a model microvessel. *Phys. Fluids*, 19:023301, 2007.

[210] D. A. Fedosov, J. Fornleitner, and G. Gompper. Margination of white blood cells in microcapillary flow. *Phys. Rev. Lett.*, 108:028104, 2012.

[211] A. Kumar and M. D. Graham. Mechanism of margination in confined flows of blood and other multicomponent suspensions. *Phys. Rev. Lett.*, 109:108102, 2012.

[212] A. Kumar and M. D. Graham. Margination and segregation in confined flows of blood and multicomponent suspensions. *Soft Matter*, 8:10536, 2012.

[213] T. M. Geislinger and T. Franke. Sorting of circulating tumor cells (MV3-melanoma) and red blood cells using non-inertial lift. *Biomicrofluidics*, 7:044120, 2013.

[214] M. Kraus, U. Seifert, and R. Lipowsky. Gravity-induced shape transformations of vesicles. *Europhys. Lett.*, 32:431, 1995.

[215] Z-H Huang, M Abkarian, and A Viallat. Sedimentation of vesicles: from pear-like shapes to microtether extrusion. *New J. Phys.*, 13:035026, 2011.

[216] G. Boedec, M. Jaeger, and M. Leonetti. Settling of a vesicle in the limit of quasi-spherical shapes. *J. Fluid Mech.*, 690:227, 2012.

[217] G. Boedec, M. Jaeger, and M. Leonett. Sedimentation-induced tether on a settling vesicle. *Phys. Rev. E*, 88:010702, 2013.

[218] I. R. Suárez, C. Leidy, G. Téllez, G. Gay, and A. Gonzalez-Mancera. Slow sedimentation and deformability of charged lipid vesicles. *PLoS ONE*, 8:e68309, 2013.

[219] M. Kummrow and W. Helfrich. Deformation of giant lipid vesicles by electric fields. *Phys. Rev. A*, 44:8356, 1991.

[220] P. Sens and H. Isambert. Undulation instability of lipid membranes under an electric field. *Phys. Rev. Lett.*, 88:128102, 2002.

[221] W. D. Ristenpart, O. Vincent, S. Lecuyer, and H. A. Stone. Dynamic angular segregation of vesicles in electrohydrodynamic flows. *Langmuir*, 26:9429, 2010.

[222] P. F. Salipante, R. L. Knorr, R. Dimova, and P. M. Vlahovska. Electrodeformation method for measuring the capacitance of bilayer membranes. *Soft Matter*, 8:3810, 2012.

[223] J. Seiwert and P. M. Vlahovska. Instability of a fluctuating membrane driven by an ac electric field. *Phys. Rev. E*, 87:022713, 2013.

[224] J. Zhang, J. D. Zahn, W. Tan, and H. Lin. A transient solution for vesicle electrodeformation and relaxation. *Phys. Fluids*, 25:071903, 2013.

[225] J. Z. Y. Chen. Pulling or compressing a vesicle by force: Solution to the bending energy model. *Phys. Rev. E*, 85:061910, 2012.

[226] J. Guven and P. Vázquez-Montejo. Force dipoles and stable local defects on fluid vesicles. *Phys. Rev. E*, 87:042710, 2013.

[227] E. Nawa, Y. Nishigaki, D. Yamamoto, and A. Shioi. Rhythmic shape change of a vesicle under a ph gradient. *Soft Matter*, 9:7832, 2013.

[228] G. Gompper and D. M. Kroll. Floppy fluid vesicles in elongational flow. *Phys. Rev. Lett.*, 71:1111, 1993.

[229] G. Gompper and D. M. Kroll. Driven transport of fluid vesicles through narrow pores. *Phys. Rev. E*, 52:4198, 1995.

[230] D. M. Kroll and G. Gompper. Polymer and vesicle conformation and scaling in elongational flow fields. *J. Chem. Phys.*, 102:9109, 1995.

[231] W. Chen, J. Chen, and L. An. Tumbling and tank-treading dynamics of individual ring polymers in shear flow. *Soft Matter*, 9:4312, 2013.

[232] J. M. Rallison. The deformation of small viscous drops and bubbles in shear flows.

Ann. Rev. Fluid Mech., 16:45, 1984.

[233] H. A. Stone. Dynamics of drop deformation and breakup in viscous fluids. *Ann. Rev. Fluid Mech.*, 26:65, 1994.

[234] C. Pozrikidis, editor. *Modelling and simulation of capsules and biological cells.* Chapman & Hall/CRC, 2003.

[235] D. Barthès-Biesel. Capsule motion in flow: Deformation and membrane buckling. *C. R. Phys.*, 10:764, 2009.

[236] R. Finken, S. Kessler, and U. Seifert. Micro-capsules in shear flow. *J. Phys.: Condens. Matter*, 23:184113, 2011.

[237] D. Barthès-Biesel. Modeling the motion of capsules in flow. *Curr. Opin. Colloid Interface Sci.*, 16:3, 2011.

[238] T. Gao, H. H. Hu, and P. Ponte Castañeda. Rheology of a suspension of elastic particles in a viscous shear flow. *J. Fluid Mech.*, 687:209, 2011.

[239] T. Gao, H. H. Hu, and P. Ponte Castañeda. Shape dynamics and rheology of soft elastic particles in a shear flow. *Phys. Rev. Lett.*, 108:058302, 2012.

[240] A. Yazdani and P. Bagchi. Influence of membrane viscosity on capsule dynamics in shear flow. *J. Fluid Mech.*, 718:569, 2013.

[241] Z. Wang, Y. Sui, P. D. M. Spelt, and W. Wang. Three-dimensional dynamics of oblate and prolate capsules in shear flow. *Phys. Rev. E*, 88:053021, 2013.

[242] M. Abkarian and A. Viallat. Vesicles and red blood cells in shear flow. *Soft Matter*, 4:653, 2008.

[243] P. M. Vlahovska, T. Podgorski, and C. Misbah. Vesicles and red blood cells in flow: From individual dynamics to rheology. *C. R. Phys.*, 10:775, 2009.

[244] C. Misbah. Vesicles, capsules and red blood cells under flow. *J. Phys.: Conf. Ser.*, 392:012005, 2012.

[245] A. M. Forsyth, J. Wan, P. D. Owrutsky, M. Abkarian, and H. A. Stone. Multiscale approach to link red blood cell dynamics, shear viscosity, and ATP release. *Proc. Natl. Acad. Sci. U. S. A.*, 108:10986, 2011.

[246] S. Braunmüller, L. Schmid, E. Sackmann, and T. Franke. Hydrodynamic deformation reveals two coupled modes/time scales of red blood cell relaxation. *Soft Matter*, 8:11240, 2012.

[247] T. M. Fischer. Shape memory of human red blood cells. *Biophys. J.*, 86:3304, 2004.

[248] L. G. Leal and E. J. Hinch. The effect of weak Brownian rotations on particles in shear flow. *J. Fluid Mech.*, 46:685, 1971.

[249] J. G. Müller. Effekte thermischen Rauschens auf die Dynamik von Vesikeln und Kapseln im Scherfluss. Master's thesis, Universität Stuttgart, 2013.

[250] H. Noguchi. Swinging and synchronized rotations of red blood cells in simple shear flow. *Phys. Rev. E*, 80:021902, 2009.

[251] Steven H. Strogatz. *Nonlinear Dynamics and Chaos.* Westview Press, 2001.

[252] O.-Y. Zhong-Can and W. Helfrich. Bending energy of vesicle membranes: General expressions for the first, second, and third variation of the shape energy and applications to spheres and cylinders. *Phys. Rev. A*, 39:5280, 1989.

[253] V. Heinrich, M. Brumen, R. Heinrich, S. Svetina, and B. Žekš. Nearly spherical vesicle shapes calculated by use of spherical harmonics : axisymmetric and nonaxisymmetric shapes and their stability. *J. Phys. II France*, 2:1081, 1992.

[254] D. C. Morse. Theory of constrained Brownian motion. *Adv. Chem. Phys.*, 128:65, 2004.

[255] R. Graham. Hydrodynamic fluctuations near the convection instability. *Phys. Rev. A*, 10:1762, 1974.

[256] K. Wiesenfeld. Noisy precursors of nonlinear instabilities. *J. Stat. Phys.*, 38:1071, 1985.

[257] Yu. A. Kravtsov and E. D. Surovyatkina. Nonlinear saturation of prebifurcation noise amplification. *Phys. Lett. A*, 319:348, 2003.

[258] E. W. Weisstein. "Spherical Harmonic." From MathWorld–A Wolfram Web Resource. http://mathworld.wolfram.com/sphericalharmonic.html.

[259] D. J. Higham. An algorithmic introduction to numerical simulation of stochastic differential equations. *SIAM Review*, 43:525, 2001.

Danksagung

Ich möchte mich bei allen bedanken, die für eine Promotion unter idealen Rahmenbedingungen gesorgt haben.

An erster Stelle gilt mein Dank Herrn Prof. Dr. Udo Seifert für das spannende Thema und die hervorragende Betreuung. Seine hohen Ansprüche und tiefen Einsichten haben meine Arbeit stets vorangebracht.

Für die Übernahme des Mitberichts danke ich Herrn Prof. Dr. Christian Holm.

Many thanks to Michael Levant and Victor Steinberg for the fruitful collaboration and the warm reception at the Weizmann Institute.

Frau Anja Steinhauser möchte ich für ihre ständige Hilfsbereitschaft und gute Laune herzlich danken.

Für die nette Atmosphäre am Institut und die manchmal blutigen Gespräche am Mensatisch möchte ich mich bei allen Mitarbeitern bedanken. Insbesondere danke ich Johannes Müller für die schöne Zusammenarbeit; Michael Bauer, David Hartich und Daniel Schmidt für das sorgfältige Korrekturlesen dieser Dissertation; und den Systemadministratoren, die immer eine originelle Ausrede parat hatten, wenn die Computers abstürzten.

Außerdem danke ich Dr. Boris Lander, Dr. Jakob Mehl, Frank Wirner, Alban Urvoy und Dr. Benedikt Sabaß für unzählige Gespräche über Gott (Evangelien nach Lukas P. und L. Matthäus) und die teilweise physikalische Welt.

Letztlich bedanke ich mich bei meinen Eltern, die mich trotz der Entfernung immer unterstützt haben, und bei Steffi.

Ehrenwörtliche Erklärung

Ich erkläre, dass ich diese Arbeit selbstständig verfasst habe und keine anderen als die angegebenen Quellen und Hilfsmittel verwendet habe.

Stuttgart, den 10. April 2014 David Abreu